



# Calibrating Interdependent Photochemistry, Nucleation, and Aerosol Microphysics in Chamber Experiments

Neil M. Donahue<sup>1</sup>, Victoria Hofbauer<sup>1</sup>, Henning Finkenzeller<sup>14, 5</sup>, Dominik Stolzenburg<sup>15, 16</sup>, Paulus S. Bauer<sup>15</sup>, Randall Chiu<sup>14</sup>, Lubna Dada<sup>5</sup>, Jonathan Duplissy<sup>5</sup>, Xu-Cheng He<sup>57</sup>, Martin Heinritzi<sup>3</sup>, Christopher R. Hoyle<sup>4</sup>, Andreas Kürten<sup>3</sup>, Aleksandr Kvashnin<sup>8</sup>, Katrianne Lehtipalo<sup>5</sup>, Naser Mahfouz<sup>1</sup>, Vladimir Makhmutov<sup>8, 9</sup>, Roy L. Mauldin III<sup>1, 14</sup>, Ugo Molteni<sup>4</sup>, Lauriane L. J. Quéléver<sup>5</sup>, Matti Rissanen<sup>5, 12</sup>, Siegfried Schobesberger<sup>6</sup>, Mario Simon<sup>3</sup>, Andrea C. Wagner<sup>3</sup>, Mingyi Wang<sup>1, 2</sup>, Chao Yan<sup>5</sup>, Penglin Ye<sup>13</sup>, Ilona Riipinen<sup>18</sup>, Hamish Gordon<sup>1</sup>, Joachim Curtius<sup>3</sup>, Armin Hansel<sup>10</sup>, Imad El Haddad<sup>4</sup>, Markku Kulmala<sup>5</sup>, Douglas R. Worsnop<sup>13, 5</sup>, Rainer Volkamer<sup>14</sup>, Paul M. Winkler<sup>15</sup>, Jasper Kirkby<sup>11, 3</sup>, and Richard Flagan<sup>17</sup>

<sup>1</sup>Center for Atmospheric Particle Studies, Carnegie Mellon University, Pittsburgh, PA, USA

<sup>2</sup>Department of the Geophysical Sciences, University of Chicago, Chicago, IL, USA

<sup>3</sup>Institute for Atmospheric and Environmental Sciences, Goethe University Frankfurt, Frankfurt am Main, Germany

<sup>4</sup>Center for Energy and Environmental Sciences, Paul Scherrer Institute, 5232 Villigen, Switzerland

<sup>5</sup>Institute for Atmospheric and Earth System Research/Physics, Faculty of Science, University of Helsinki, Helsinki, Finland

<sup>6</sup>Department of Technical Physics, University of Eastern Finland, PO Box 1627, 70211 Kuopio, Finland

<sup>7</sup>Yusuf Hamied Department of Chemistry, University of Cambridge, Cambridge, UK

<sup>8</sup>P. N. Lebedev Physical Institute of the Russian Academy of Sciences, 119991 Moscow, Russia

<sup>9</sup>Moscow Institute of Physics and Technology (National Research University), 141701 Moscow, Russian Federation

<sup>10</sup>Ion Molecule Reactions Environmental Physics Group Institute of Ion Physics and Applied Physics Leopold-Franzens University, Innsbruck Technikerstraße 25 A-6020 Innsbruck Austria

<sup>11</sup>CERN, the European Organization for Nuclear Research, Geneve 23 CH-1211, Switzerland

<sup>12</sup>Tampere University, Physics Unit, 33720 Tampere, Finland

<sup>13</sup>Aerodyne Inc, Billerica MA, USA

<sup>14</sup>University of Colorado, Boulder, Atmospheric and Oceanic Sciences, P.O. Box 311, Boulder, CO 80309 USA

<sup>15</sup>Faculty of Physics, University of Vienna, Wien, Austria

<sup>16</sup>Institute of Materials Chemistry, TU Wien, Vienna, Austria

<sup>17</sup>Division of Chemistry and Chemical Engineering, California Institute of Technology, Pasadena, CA 91125, USA

<sup>18</sup>Department of Environmental Science (ACES), Stockholm University, Stockholm, Sweden

**Correspondence:** Neil M. Donahue (nmd@andrew.cmu.edu)

**Abstract.** Laboratory experiments addressing complex phenomena such as atmospheric new-particle formation and growth typically involve numerous instruments measuring a range of key coupled variables. In addition to independent calibration, the combined dataset provides not just constraints on the parameters of interest but also on the critical instrument calibrations. Here we find good agreement between production and loss rates of sulfuric acid ( $H_2SO_4$ ) in an experiment performed at the CERN

5 CLOUD chamber involving oxidation of sulfur dioxide ( $SO_2$ ) in the presence of ammonia ( $NH_3$ ) at 58% relative humidity, driving new-particle formation and growth of particles by  $H_2SO_4 + NH_3$  nucleation initiated by  $O_3$  photolysis via several light sources. This closure requires consistency across numerous parameters, including: the particle number and size distribution; their condensation sink for  $H_2SO_4$ ; the particle growth rates; the concentration of  $H_2SO_4$ ; and the nucleation coefficients for



both neutral and ion-induced pathways. Our study shows that accurate agreement can be achieved between production and loss  
10 of condensable vapors in laboratory chambers under atmospheric conditions, with accuracy ultimately tied to particle number  
measurement (i.e. a condensation particle counter). This, in turn implies parameters such as the  $\text{H}_2\text{SO}_4$  concentration and  
particle size distributions can be determined to a comparable precision.

## 1 Introduction

The Cosmics Leaving OUtdoor Droplets (CLOUD) experiment at CERN was designed to determine particle nucleation rates  
15 under atmospheric conditions, including the effect of ionization from galactic cosmic rays (Kirkby et al., 2011; Duplissy et al., 2016). Experiments such as this are complex, involving many interconnected measurement and theoretical parameters. These parameters are often constrained separately, for example via offline instrument calibration, characterization of transfer functions, sample line-loss corrections, and so forth. All these calibrations and corrections are subject to random and systematic error.

20 Some calibrations depend on these other calibrations for their own accuracy. An example central to this paper is actinometry – specifically calibration of actinic fluxes from UV lights driving  $\text{O}_3$  photolysis, OH production,  $\text{SO}_2$  oxidation and thus  $\text{H}_2\text{SO}_4$  vapor production. Calibration of light intensities requires accurate measurement of several gas concentrations, including  $\text{H}_2\text{O}$ ,  $\text{O}_3$ ,  $\text{SO}_2$ , all species that react with OH at significant rates, and  $\text{H}_2\text{SO}_4$  itself. Here we shall consider an even larger set of interconnected measurements with associated signals or values incorporating particle nucleation and subsequent growth  
25 governed by that  $\text{H}_2\text{SO}_4$  vapor. All the values have *a priori* (independent) calibration parameters (“prm”) for signals,  $\{s_{\text{prm}}\}$ , or other values,  $\{\kappa_{\text{prm}}\}$ , etc; these include: gas-phase concentrations; particle number; particle charge; size distributions; light spectra, intensities, and amplitudes; and constants such as first-order wall loss, rate coefficients, etc.

Our objective is to scale the *a priori* parameters by a set of calibration factors,  $\{\mathcal{F}_{\text{prm}}^{\text{cal}}\}$ , to obtain overall consistency among the various measurements in the combined dataset, constrained by models of gas-phase photochemistry and aerosol  
30 microphysics. If all measurements were initially perfect and independent, we would find a solution  $\mathcal{F}_{\text{prm}}^{\text{cal}} = 1 \pm 0$  along a diagonal. Our ultimate aim is to find  $\{\mathcal{F}_{\text{prm}}^{\text{cal}}\}$  through a formal optimization and so also obtain a probability density function  $\{\mathcal{P}_{\text{prm}}^{\text{cal}}\}$ , including a full covariance among all of the factors Ozon et al. (2021a, b). Those covariances serve formally as the strong interconnections between measurements that can substantially reduce the overall uncertainty. Here we present a less formal proof-of-concept to obtain “by eye” estimates of the most likely  $\{\mathcal{F}_{\text{prm}}^{\text{cal}}\}$ . Even this less formal method can substantially  
35 tighten constraints on important parameters while building a self consistent representation of the experimental system. We shall argue that the interconnected calibrations are much more robust, and accurate, than any of the individual, *a priori*, values.

## 2 Methods

The CERN CLOUD chamber is a  $26.1 \text{ m}^3$  stainless steel reactor maintained to a high degree of cleanliness. It is fed by ultrapure cryogenic  $\text{N}_2$  and  $\text{O}_2$  and operated as a continuously stirred tank reactor (CSTR), with inductively coupled mixing fans at the

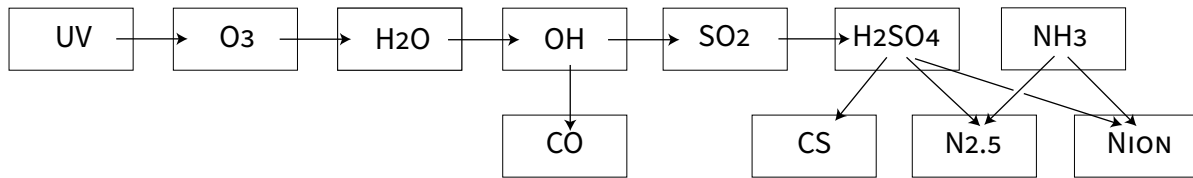


**Figure 1.** Scheme of interconnected measurements linking UV intensities to new-particle formation, and the elements required for a robust calibration. Gas phase species (and light) drive particle microphysics (nucleation and growth) depicted by the condensation sink (CS) and the total particle number ( $N_{2.5}$ ) as well as the ion distribution ( $N_{ion}$ ). The ability to measure  $N_{2.5}$  accurately (with a condensation particle counter) and  $H_2SO_4$  precisely (with an  $NO_3^-$  chemical ionization mass spectrometer) permits a robust constraint on  $H_2SO_4$  first-order loss as well as absolute calibration, particle growth rates, and the particle nucleation rate. This propagates backwards to the UV light intensities and  $O_3$  photolysis rates.

40 top and bottom maintaining well-mixed conditions (Kirkby et al., 2011; Duplissy et al., 2016). Flow in is balanced by flow out (largely to the many sampling instruments) with a dilution timescale of roughly 1.5 h and pressure maintained slightly above the ambient pressure in Geneva (965 hPa mean) to ensure that no contamination leaks into the chamber. An insulated thermal housing permits operation between 213 and 313 K. Water is added via a nafion humidifier to control the relative humidity. Under typical operating conditions with the fans at 12% of their maximum speed, the resulting turbulent loss of vapors such as 45  $H_2SO_4$  to the chamber walls proceeds with a first-order time constant of roughly 500 s (Stolzenburg et al., 2020).

The chamber was designed with careful control over ionization conditions and can operate in three modes: neutral, galactic cosmic ray (“gcr”) and beam. In the neutral mode electrodes at the top and bottom of the chamber establish a  $20\text{ kV m}^{-1}$  50 clearing field to sweep out all primary ions in roughly 1 s (Kirkby et al., 2011). In the gcr mode, the clearing field is off and ion-pair formation governed by incident cosmic rays (along with stray muons from the CERN beam target) forms ion pairs at a rate of  $2\text{--}7\text{ cm}^{-3}\text{ s}^{-1}$ . In the beam mode, a  $3.5\text{ GeV }\pi^+$  diffuse beam from the CERN proton synchrotron increases the ion-pair 55 formation rate up to  $100\text{ ion pairs cm}^{-3}\text{ s}^{-1}$ , reproducing ion-pair concentrations found in the upper troposphere.

CLOUD is illuminated by multiple different light sources to initiate photolysis of various gases. Three light sources are important here. A set of 4 Hg–Xe lamps (Hamamatsu) is coupled to the chamber via an array of carefully aligned optical fiber bundles fixed in the top cover of the chamber and oriented to provide relatively homogeneous light intensity (Kupc et al., 55 2011). These lights are known as “UVH” and can be adjusted via electro-mechanical apertures in each lamp housing. One optical fiber bundle located on the upper access cover at the top of the chamber couples a 248 nm Kr–F excimer laser into the chamber (Lehtipalo et al., 2016). This light is known as “UVX” and can be adjusted by controlling the laser pulse repetition frequency and pulse energy. Finally, a bank of UV light emitting diodes with peak intensities near 385 nm projects radially into the chamber at the middle level, along with the instrument sampling ports, with LEDs pointing axially upwards and downwards 60 in pairs (Lehtipalo et al., 2016). These diodes are housed in a quartz jacket and are cooled with chilled recirculating liquid to remove excess heat, and the 385 nm LED “light saber” is known as LS3. The various light amplitudes are measured with the combination of a UVVis spectrometer and several photodiodes, all of which are coupled to the chamber via optical fibers



located on the lower access cover, at the bottom of the chamber (Finkenzeller et al., 2022). The details of that measurement are described in a separate paper, but here the amplitude of each light appears as  $a_{lt}$ .

65 Multiple instruments are important to this paper, and we follow the sequence in Fig. 1. Relative humidity (RH) is measured with a commercial RH sensor for dew points above 260 K. Ozone ( $O_3$ ) is produced in an external generator from pure  $O_2$  irradiated with 185 nm VUV light and measured via UV absorption. There  $O_3$  generation might form some contaminant VOCs, but previous work has shown these to be negligible (Schnitzhofer et al., 2014). Carbon monoxide (CO) is always present in cryogenic  $N_2$  but was not measured at CLOUD during the campaign described here; however, measurements during 70 subsequent campaigns have shown a constant CO concentration of roughly 100 ppbv. There was no methane added to the pure synthetic air mixture, and no added  $NO_x$  during the run described here. Sulfur dioxide ( $SO_2$ ) is added to CLOUD from a compressed gas cylinder via a mass flow controller in the gas handling system and measured with a calibrated  $SO_2$  instrument. Sulfuric acid vapor ( $H_2SO_4$ ) is measured with two (semi) independently calibrated  $NO_3^-$  chemical ionization time-of-flight 75 mass spectrometers. Ammonia ( $NH_3$ ) is measured with a Picarro PI2103 analyzer, by mass spectrometry at concentrations below 1 ppbv, and also constrained via the steady-state balance between a known flow in and the chamber dilution timescale.

We regard the RH,  $O_3$  and  $SO_2$  measurements as well calibrated and relatively straightforward. The  $H_2SO_4$  and  $NH_3$  measurements are more difficult and thus uncertain. All instruments are corrected for vapor losses during sampling, but the  $H_2SO_4$  calibration itself depends on a known and controlled production and loss in a custom designed calibrator (Kürten et al., 2012) and  $NH_3$  is notoriously sticky and difficult to correct for surface equilibration and humidity effects, especially at the sub-ppb 80 levels typically used in CLOUD.

In addition to the gas measurements, several particle instruments are also important. The number concentration of particles with a mobility diameter greater than 2.5 nm is measured with a butanol condensation particle counter, known as the CPC<sub>2.5</sub>. The size distribution of particles is measured with an ensemble of instruments; here we rely on a scanning mobility particle sizer (SMPS) for particles larger than 7 nm and on a “DMA train” (Stolzenburg et al., 2017) for particles between 1.5 and 7 nm. 85 Finally, charged particles are measured with two Air Ion Spectrometers (AIS) operating in negative and positive mode, each with a succession of electrodes to measure ions with mobility diameters between 0.9 and 40 nm (the commercial instrument is known as an NAIS (Mirme and Mirme, 2013) because a corona wire can also charge neutral particles for subsequent detection, but that was not used here).

The CPC<sub>2.5</sub> is the cornerstone of this analysis; as an inversion our method works backwards in Fig. 1 toward  $P_{H_2SO_4}$  and 90 ultimately to  $j_{O(^1D)}$  and the calibrated UV light intensity. Especially when most of the particles are larger than 2.5 nm, sample line losses are minimal and the particle sampling efficiency is near 100%. The other particle measurements are less certain. The SMPS measurements depend on a known charging efficiency in the particle neutralizer and also known transmission within the differential mobility analyzer (DMA) column. We regard the size distribution amplitude measurement as precise, though particle water content and possible drying while sampling and classifying adds uncertainty to the (mobility) size determination 95 itself. The absolute magnitude of the SMPS is less accurate. The DMA train has similar systematic uncertainties. Finally, the AIS measurements are of highly mobile ions and again subject to systematic uncertainty.

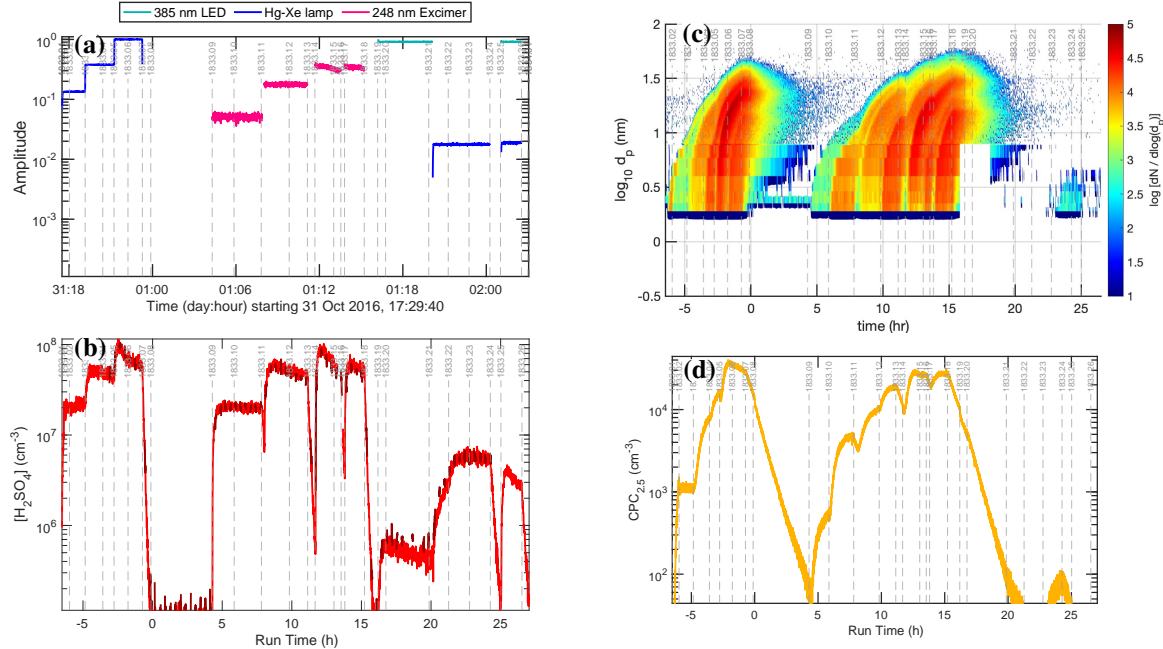


**Figure 2.** Raw photochemical observations for CLOUD11 Run 1833. (a) Light amplitudes obtained from a UVVis spectrometer vs time (UTC). The run included two intervals with systematic amplitude steps for a single light source: first the “UVH stages” (stages 01 - 08 with steps in the dark blue Hg-Xe lamp) and second the “UVX stages” (stages 09 - 18 with steps in the magenta Excimer laser). (b)  $\text{H}_2\text{SO}_4$  measured by two  $\text{NO}_3^-$  CIMS vs time relative to 0 h 01 Nov 2016. The lighter red values are from a dedicated  $\text{H}_2\text{SO}_4$  instrument whereas the darker red values are from a “ $\text{HO}_x - \text{RO}_x$ ” instrument with a modified inlet alternating between  $\text{H}_2\text{SO}_4$  mode and  $\text{HO}_x$  mode. During each sub-run the  $\text{H}_2\text{SO}_4$  signal follows the steps in light intensity, with important deviations. (c) Particle size distribution obtained by merging data from the DMA train, a nano-SMPS and an SMPS. The DMA train covers  $1.7 < d_p < 7.9$  nm with lower size resolution but greater accuracy than the SMPS. Both the UVH and UVX sub-runs display nucleation bursts associated with each stage, forming “bunches of bananas” with near monotonically increasing CPC<sub>2.5</sub> concentrations. Data from the DMA train are missing near run time 17-19 h. (d) Total particle number measured with a Condensation Particle Counter (CPC<sub>2.5</sub>).

### 3 $\text{H}_2\text{SO}_4$ production and loss

Here we shall consider a CLOUD calibration run designed to constrain OH production from  $\text{O}_3$  photolysis by measurement of  $\text{H}_2\text{SO}_4$ , during which particles nucleated via  $\text{H}_2\text{SO}_4 + \text{NH}_3$  “ternary” nucleation and grew via co-condensation of  $\text{H}_2\text{SO}_4$  and  $\text{NH}_3$  (Vehkamaki and Riipinen, 2012). Far more (and better) than a simple “actinometry” run, which would rely on accurate  $\text{H}_2\text{SO}_4$  measurements for the light calibrations, the combined photolysis, nucleation, growth and loss run establishes a robust interconnection of many of the measurements central to CLOUD nucleation rate determinations.

As depicted in Fig. 1, we will show that the combination of the CPC<sub>2.5</sub> with the particle sizing (size distribution) instruments supports a tightly constrained and accurate determination of both the particle number distribution and particle surface area



105 distribution, which in turn agree with precisely observed  $\text{H}_2\text{SO}_4$  first-order losses (to particle condensation and the chamber walls). With the evolving particle size distribution (and total number) well constrained, the particle growth rates and nucleation rates are also well constrained. As particle growth is rate-limited by  $\text{H}_2\text{SO}_4$  condensation (Stolzenburg et al., 2020), this in turn constrains the absolute  $\text{H}_2\text{SO}_4$  concentrations and thus the  $\text{NO}_3^-$  CIMS calibrations. Finally, with the gas-phase  $\text{H}_2\text{SO}_4$  known accurately, it is possible to determine, in order, the  $\text{SO}_2$  oxidation rate, the  $\text{OH}$  concentration, the  $\text{OH}$  loss and thus production 110 rate (in steady state) and, ultimately, the production rate of  $\text{O}(\text{¹D})$  from  $\text{O}_3$  photolysis and thus the volume averaged actinic flux of each light source (averaged over the overlap between the light source and the  $\text{O}_3$  action spectrum toward  $\text{O}(\text{¹D})$ ).

To interpret the observations and develop constraints,  $\mathcal{F}$ , we will employ a gas-phase photochemical model as well as a microphysical model, connecting the two with observed particle size distributions (which affect the  $\text{H}_2\text{SO}_4$  condensation lifetime) as well as observed  $\text{H}_2\text{SO}_4$  (which affects all aspects of the particle microphysics). The following processes are 115 involved, more or less in order but forming a closed loop. The terms  $c_i$ ,  $P_i$  and  $L_i$  are the concentration, production and loss rates of species  $i$ ,  $k_{\text{rxn}}$  is the rate coefficient for reaction “rxn”,  $k_i^{\text{I}}$  is the overall first-order loss coefficient for species  $i$ , and  $j_{\text{proc}}$  is a (first-order) photolysis coefficient for process “proc”.

As shown in Fig. 1, the sequence of steps that lead to  $\text{H}_2\text{SO}_4$  production start with ozone photolysis to produce  $\text{O}(\text{¹D})$  by light source “lt” with amplitude  $s_{\text{lt}}$  and an (unknown) calibration factor  $a_{\text{lt}}$ :

120 
$$j_{\text{O}(\text{¹D})} = a_{\text{lt}} s_{\text{lt}}$$

$$P_{\text{O}(\text{¹D})} = j_{\text{O}(\text{¹D})} c_{\text{O}_3}$$

$$L_{\text{O}(\text{¹D})} = (k_{\text{N}_2} c_{\text{N}_2} + k_{\text{O}_2} c_{\text{O}_2} + k_{\text{H}_2\text{O}} c_{\text{H}_2\text{O}}) c_{\text{O}(\text{¹D})}^{\text{ss}}$$

$$P_{\text{OH}} = 2 k_{\text{H}_2\text{O}} c_{\text{H}_2\text{O}} c_{\text{O}(\text{¹D})}^{\text{ss}} + \dots$$

$$L_{\text{OH}} = (k_{\text{CO}} c_{\text{CO}} + k_{\text{O}_3} c_{\text{O}_3} + k_{\text{SO}_2} c_{\text{SO}_2} + \dots) c_{\text{OH}}^{\text{ss}}$$

125 
$$P_{\text{H}_2\text{SO}_4} = k_{\text{SO}_2} c_{\text{SO}_2} c_{\text{OH}}^{\text{ss}}$$

This will be balanced by  $\text{H}_2\text{SO}_4$  loss on a timescale given by the inverse of the overall first-order loss coefficient  $k_{\text{H}_2\text{SO}_4}^{\text{I}}$ , which includes terms for wall loss, condensation loss, and ventilation, among others:

$$L_{\text{H}_2\text{SO}_4} = k_{\text{H}_2\text{SO}_4}^{\text{I}} c_{\text{H}_2\text{SO}_4}$$

$$k_{\text{H}_2\text{SO}_4}^{\text{I}} = k_{\text{wall}}^{\text{I}} + k_{\text{cond}}^{\text{I}} + \dots$$

130

The production and loss balance can be used to constrain the calibration factor  $a_{\text{lt}}$ , provided that  $k_{\text{H}_2\text{SO}_4}^{\text{I}}$  and  $c_{\text{H}_2\text{SO}_4}$  are known accurately (along with the other concentrations connecting the light intensity to  $\text{H}_2\text{SO}_4$ ). However, part of the  $\text{H}_2\text{SO}_4$  loss is to particles, which in turn form and grow because of  $\text{H}_2\text{SO}_4$  condensation. Particle production ( $J$ ), growth ( $G$ ), and loss ( $L$ ) vs diameter  $d_p$  are thus also coupled to this system. These also depend on the particle charge state, which for these tiny particles



135 is either neutral,  $\circ$ , or a single positive or negative charge,  $\pm$ :

$$J_{\text{nuc}}^{\circ, \pm} = k_{\text{nuc}}^{\circ, \pm} c_{\text{H}_2\text{SO}_4}^3 c_{\text{NH}_3} n^{\circ, \pm} \quad (n^\circ \equiv 1)$$

$$G(d_p) = k_{\text{gr}} c_{\text{H}_2\text{SO}_4}$$

$$L(d_p) = (k_{\text{wall}}^{\text{I}}(d_p) + k_{\text{vent}}^{\text{I}}) n(d_p)$$

Finally, the production of primary ions,  $n^\pm$  is given by an ion-pair formation rate  $Q_{\text{ip}}$  (by cosmic rays or the CERN pion beam) 140 while the loss of those primary ions includes wall loss, ion recombination, ion-induced nucleation, and diffusion charging and neutralization of larger particles,  $\mathcal{C}^{\circ, \pm}$ :

$$P_\pm = Q_{\text{ip}}$$

$$L_\pm = (k_{\text{ion}}^{\text{I}} n^\mp) n^\pm + J_{\text{nuc}}^\pm + \mathcal{C}^{\circ, \mp}$$

As a test case we consider an actinometry run during the CLOUD11 campaign in Autumn 2016. Run 1833 lasted from 145 roughly 1730h on 31 Oct to roughly 0400h on 2 Nov, with the chamber at 297.8 K, 58 % relative humidity, and 987 hPa. O<sub>3</sub> was near 42 ppbv, SO<sub>2</sub> near 2 ppbv, NH<sub>3</sub> at 2 ppbv, and CO was near 100 ppbv.

### 3.1 Raw measurements

We show data from Run 1833 in Figs 2 – 4. The run comprised a sequence of 26 stages, each with different nominal conditions. The stages are marked in the figures by dashed vertical gray lines numbered at the top. During intervals comprising sets of 150 stages, we systematically increased the amplitudes of different light sources (principally UVH and UVX) with pairs of neutral and charged (gcr) stages, and we followed each interval with a “cleaning” stage to remove particles from the chamber.

Fig. 2a shows the unfiltered amplitudes of the three light sources over the course of the run, obtained from the UVVis spectrometer, including some crosstalk. The light sources are labeled in the figure as “Hg–Xe lamp” (UVH), “248 nm excimer laser” (UVX), and “385 nm LED” (LS3). During the run, first the Hg–Xe lamps (stages 01 – 08; the UVH stages) and then the 155 excimer laser (stages 09 – 18; the UVX stages) were systematically stepped through 3 intensities, at roughly 10 %, 40 % and 100 % of full power. After this the 385 nm LEDs were turned on at full power (stages 19 and 20) and finally all the lights were turned on in sequence (stages 21 – 26), with the Hg–Xe and excimer lights at low power and the LEDs again at full power. With every change of light intensity, the H<sub>2</sub>SO<sub>4</sub> shown in Fig. 2b changed rapidly in response, for the most part reaching a steady state within minutes, reflecting the wall-loss timescale of H<sub>2</sub>SO<sub>4</sub>. However, while the H<sub>2</sub>SO<sub>4</sub> broadly followed the steps 160 in light amplitudes, there are obvious deviations, notably when the H<sub>2</sub>SO<sub>4</sub> concentration was high during stages 05 – 06 and again during stages 14 – 15.

The H<sub>2</sub>SO<sub>4</sub> depletion was caused by condensation to particles. Especially during the UVH and UVX stages, the H<sub>2</sub>SO<sub>4</sub> concentration was high enough to drive nucleation and substantial growth, which in turn built up a condensation sink competitive with wall loss for condensable vapors such as H<sub>2</sub>SO<sub>4</sub>. Fig. 2c shows particle size distributions vs time, measured with a scanning mobility particle sizer (SMPS), a nano-SMPS, and a DMA train. This shows a succession of overlapping nucleation and 165

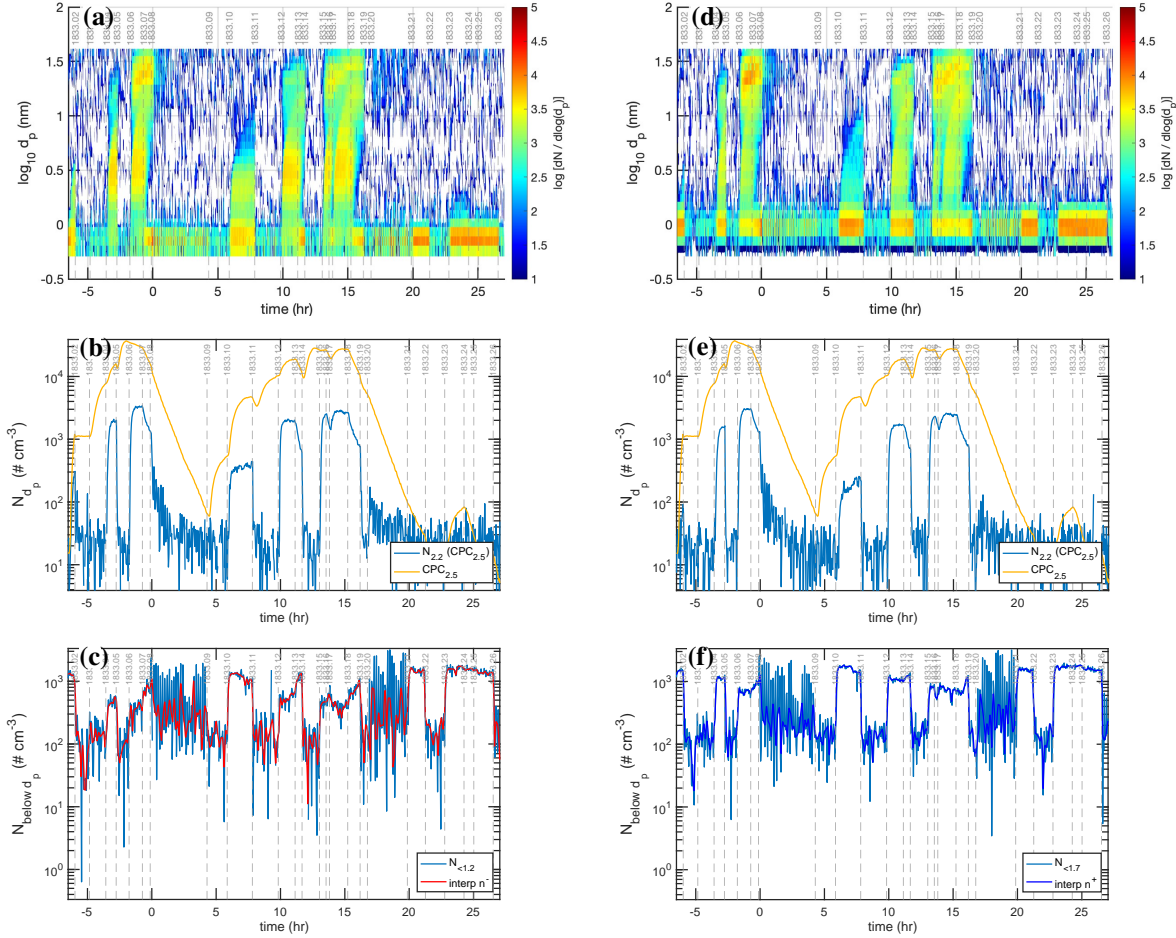


**Figure 3.** Raw negatively (left) and positively (right) charged particle observations, compared with total particle counts. (a), (d) Air Ion Spectrometer (AIS) distributions; (b), (e) total AIS number for given polarity above 2.2 nm (2.5 nm mobility diameter) compared with total CPC<sub>2.5</sub>; (c), (f) charged particle number smaller than 1.2 nm (left, negatively charged) and 1.7 nm (right, positively charged), constituting the primary ions, along with a filtered interpolant. Strong ion-induced nucleation stages (i.e. 06, 17) show nearly equal negatively and positively charged particles near  $3 \times 10^3 \text{ cm}^{-3}$  comprising, in total, roughly 20 % of the total CPC<sub>2.5</sub> concentration. During weak ion-induced nucleation (i.e. stage 10) the negatively charged particles are roughly twice as abundant as the positively charged particles (300 vs 150  $\text{cm}^{-3}$ ). The level signal of small ions in the bottom panels of  $\sim 200 \text{ cm}^{-3}$  during neutral stages (with a high-voltage clearing field turned on) are due to instrumental electronic noise; the true ion concentrations are well below  $10 \text{ cm}^{-3}$ . The oscillating signals during cleaning stages 08 and 20 are caused by alternating on/off cycles of the high-voltage clearing field.

growth bursts (a bunch of bananas) while the Hg–Xe and excimer light sources were being stepped up. Here we use physical particle diameter ( $d_p$ ) to represent (and model) the size distribution but retain the standard practice of describing classifiers by their classification size (here mobility diameter,  $d_{\text{mob}}$ ); we relate the two with  $d_{\text{mob}} = d_p + 0.3 \text{ nm}$  (Larriba et al., 2011). Fig. 2d shows the total particle number above 2.5 nm (mobility diameter) measured with a condensation particle counter (CPC<sub>2.5</sub>).



170 Fig. 3 shows charged particle size distributions from the two air-ion spectrometers (AIS), one in negative mode (a-c, left panels) and one in positive mode (d-f, right panels). The top panels (a and d) are the measured size distributions, the middle panels (b and e) are the integrated cuts above  $d_p = 2.2$  nm (compared with the total CPC<sub>2.5</sub> measurement of all particles), and the bottom panels (c and f) are integrated counts below a cut size of 1.2 nm for the negative particles and 1.7 nm for the positive particles, along with a median filtered interpolant of these values. These small particles are the primary ions responsible for  
175 ion-induced nucleation.

180 For the UVH and UVX stages, each light power setting included a neutral stage (field on) and a stage charged by galactic cosmic rays (gcr, field off). In most cases the neutral stage preceded the charged stage so that the weaker neutral nucleation could be easily distinguished from stronger ion-induced nucleation. An exception is the first pair of stages, 01 and 02, where the chamber was initially charged in stage 01 and then switched to neutral in stage 02. This was because the neutral nucleation under these low H<sub>2</sub>SO<sub>4</sub> conditions was very weak, and the initial burst of ion-induced nucleation during stage 01 appears as a clear mode growing toward 20 nm over time in Fig. 2c. For all the other pairs at a fixed light setting during both the UVH and UVX stages, the neutral stage preceded the charged stage.

185 The run included two cleaning stages (08 and 20), during which the clearing field alternated between on and off with the pion beam also on. During these stages the AIS data oscillate between the highest and very low values, which is clearly evident in the raw particle number counts (Fig. 3c and 3f). These cleaning stages are designed to generate primary ions with the clearing field off, which then charge a fraction of the larger particles via diffusion charging. When the clearing field turns on, these charged particles are then swept out of the chamber. Because the steady state charged fraction of these small particles is very low (as is clearly evident in the middle panels of these figures), this alternating method first removes any charge particles and then builds the charge distribution back towards the steady state value, thus progressively removing the larger particles (which  
190 would otherwise be removed on the slow ventilation timescale of the chamber).

195 Because the condensation sink occasionally grew to be competitive with wall loss, we must account for this to quantitatively constrain H<sub>2</sub>SO<sub>4</sub> production and loss. However, the evident exponential drop in H<sub>2</sub>SO<sub>4</sub> in, e.g., stages 05 – 06 shows that the enhanced H<sub>2</sub>SO<sub>4</sub> loss is also a *measurement* of the (first-order) condensation sink, requiring only precise H<sub>2</sub>SO<sub>4</sub> measurements, not accurate knowledge of the H<sub>2</sub>SO<sub>4</sub> absolute calibration. Further, the growth (rate) of the particles was governed by H<sub>2</sub>SO<sub>4</sub> condensation; consequently, with the condensation sink well constrained, the growth rate in turn constrains the absolute H<sub>2</sub>SO<sub>4</sub> concentration, provided we can account for the role of co-condensing NH<sub>3</sub> and H<sub>2</sub>O. Finally, the nucleation rates (neutral and charged) also depend strongly on the H<sub>2</sub>SO<sub>4</sub> concentration (in addition to NH<sub>3</sub> and ion concentrations) and so with all these other parameters fixed by multiple constraints, the concentrations driving observed nucleation rates are known accurately.

200 We show two other important gas-phase measurements in Fig. 4a: O<sub>3</sub> and b SO<sub>2</sub>. Ozone photolysis leading to OH drives the whole system, H<sub>2</sub>SO<sub>4</sub> is produced via SO<sub>2</sub> + OH, and so the production rate is proportional to both of these. Both O<sub>3</sub> and SO<sub>2</sub> include notable variations, which we will discuss below. In addition to those, the absolute H<sub>2</sub>O was known because T and RH were controlled, whereas the gas-phase NH<sub>3</sub> measurement was unreliable and CO (present in synthetic air) was unmeasured. Both were likely constant during Run 1833 but affect some of the absolute calibrations.

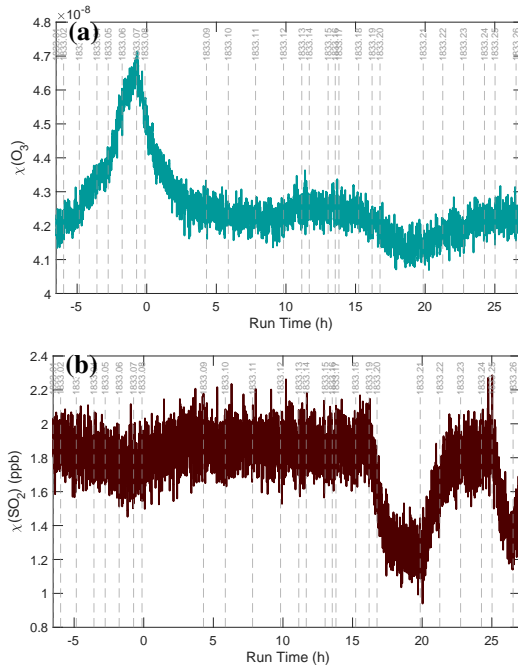


**Figure 4.** Raw chemical drivers for  $\text{H}_2\text{SO}_4$  formation. (a)  $\text{O}_3$  mixing ratio. (b)  $\text{SO}_2$  mixing ratio. Increased  $\text{O}_3$  during stages 1–6 is caused by  $\text{O}_2$  photolysis by the  $\text{Xe}–\text{Hg}$  arc lamps. Nearly stoichiometric (1:1) depletion of  $\text{SO}_2$  and  $\text{O}_3$  during stages 19 and 20 (with intense irradiation by 385 nm light) is consistent with photo-enhanced wall uptake of  $\text{SO}_2$ , presumably leaving  $\text{SO}_4$  on the chamber walls.

All the data in Figs 2 and 4 require some amount of refinement. In addition to possible calibration factors,  $\mathcal{F}$ , most benefit  
205 from smoothing. We favor median filters as they exclude outliers and maintain sharp edges. In many cases we combine median filtering with interpolation to develop interpolants so that we can use the observed data to drive constrained models of gas-phase chemistry and particle microphysics.

The CPC<sub>2.5</sub> particle number concentration is the most robust and accurate measurement in this dataset. Much of the time, most of the particles were between 10 and 30 nm. Particles in this size range have relatively low mobility (compared to  
210 molecules). Fig. 3 shows they were for the most part neutral. Consequently, line losses between the chamber and the CPC were low. Also, during this run it took many minutes for nucleated particles to grow to this size, so the CPC<sub>2.5</sub> concentration was almost certainly homogeneous in the chamber. Finally, the CPC itself is a robust instrument, relying only on activation by a controlled supersaturation of 1-butanol; while there is some particle composition dependence to this activation, that is important only for particles near the cutoff activation diameter (2.5 nm); the particles in these experiments were usually much  
215 larger than that cutoff size and so this has a minimal effect. Here we assume detection by the CPC<sub>2.5</sub> is a step-function cut in the size distribution at a physical diameter  $d_p \geq 2.2$  nm. Overall, we estimate that we constrain  $N_{2.2}$  with an accuracy of well below 10 % under these conditions.



## 4 Calibration elements

To constrain calibration factors,  $\mathcal{F}^{\text{cal}}$ , our strategy is to start with observational constraints based on instrument precision and 220 then to add in constraints based on accuracy, starting with the CPC<sub>2.5</sub>. We shall start with the H<sub>2</sub>SO<sub>4</sub> first-order loss terms (wall and condensation), which depend on precise H<sub>2</sub>SO<sub>4</sub> signals but not accurate calibration; then we will address particle formation and growth, which both depend on accurate (calibrated) H<sub>2</sub>SO<sub>4</sub> measurements; and finally, we will turn to photochemical and microphysical to model H<sub>2</sub>SO<sub>4</sub> production, evolution of the particle size distribution, and particle charging. The models will also permit a detailed examination of key process rates.

225 The absolute H<sub>2</sub>SO<sub>4</sub> concentration includes a calibration scaling factor:

$$c_{\text{H}_2\text{SO}_4} = \mathcal{F}_{\text{H}_2\text{SO}_4}^{\text{cal}} s_{\text{H}_2\text{SO}_4}$$

This is the nominal H<sub>2</sub>SO<sub>4</sub> concentration (signal) as measured via NO<sub>3</sub><sup>-</sup> CIMS,  $s_{\text{H}_2\text{SO}_4}$ , multiplied by a calibration factor 230  $\mathcal{F}_{\text{H}_2\text{SO}_4}^{\text{cal}}$  based on additional constraints from this unified calibration. In some circumstances there may be “hidden” sulfuric acid contributing to nucleation or growth (Rondo et al., 2016), but this has been shown to be negligible for the (NH<sub>3</sub>)<sub>2</sub>·SO<sub>4</sub> system (Stolzenburg et al., 2020), and our observations support this finding.

Accurate measurement of H<sub>2</sub>SO<sub>4</sub> is so central to nucleation and growth experiments that establishing the best possible  $\mathcal{F}_{\text{H}_2\text{SO}_4}^{\text{cal}}$  is in many ways our ultimate objective. This extends even beyond particle formation involving H<sub>2</sub>SO<sub>4</sub>, because often the calibration of other constituents (i.e. Highly Oxygenated Organic Molecules, HOMs) is also tied to the H<sub>2</sub>SO<sub>4</sub> calibration in a chemical ionization mass spectrometer (Ehn et al., 2014).

235 The central feature of these actinometry runs is the balance of production and loss for H<sub>2</sub>SO<sub>4</sub>:

$$\frac{d}{dt} c_{\text{H}_2\text{SO}_4} = P_{\text{H}_2\text{SO}_4} - k_{\text{H}_2\text{SO}_4}^{\text{I}} c_{\text{H}_2\text{SO}_4}$$

This has a steady-state solution

$$c_{\text{H}_2\text{SO}_4}^{\text{ss}} = \frac{P_{\text{H}_2\text{SO}_4}}{k_{\text{H}_2\text{SO}_4}^{\text{I}}} = P_{\text{H}_2\text{SO}_4} \tau_{\text{H}_2\text{SO}_4}$$

If the H<sub>2</sub>SO<sub>4</sub> concentration in Fig. 2 is accurately calibrated, then this becomes a constraint on the H<sub>2</sub>SO<sub>4</sub> production rate

$$240 P_{\text{H}_2\text{SO}_4} = c_{\text{H}_2\text{SO}_4}^{\text{ss}} k_{\text{H}_2\text{SO}_4}^{\text{I}} = \mathcal{F}_{\text{H}_2\text{SO}_4}^{\text{cal}} s_{\text{H}_2\text{SO}_4}^{\text{ss}} k_{\text{H}_2\text{SO}_4}^{\text{I}}$$

Regardless, the light calibration unavoidably involves accurate knowledge of the H<sub>2</sub>SO<sub>4</sub> concentration and lifetime; consequently, it is the production rate of H<sub>2</sub>SO<sub>4</sub> that is most directly calibrated.

### 4.1 Loss constraints

When  $P_{\text{H}_2\text{SO}_4} \ll k_{\text{H}_2\text{SO}_4}^{\text{I}} c_{\text{H}_2\text{SO}_4}$  (as in stages 07–08, 13, and 18), the H<sub>2</sub>SO<sub>4</sub> follows pseudo first-order loss

$$245 \frac{d}{dt} \ln(s_{\text{H}_2\text{SO}_4}) \simeq -k_{\text{H}_2\text{SO}_4}^{\text{I}}$$



That first-order sulfuric acid loss (inverse lifetime) comprises several elements

$$\begin{aligned} k_{\text{H}_2\text{SO}_4}^{\text{I}} &= k_{\text{H}_2\text{SO}_4}^{\text{wall}} + k_{\text{H}_2\text{SO}_4}^{\text{cond}} + (k_{\text{H}_2\text{SO}_4}^{\text{dil}} + k_{\text{H}_2\text{SO}_4}^{\text{nuc}} + \dots) \\ &= \mathcal{F}_{\text{H}_2\text{SO}_4}^{\text{wall}} \kappa_{\text{H}_2\text{SO}_4}^{\text{wall}} + \mathcal{F}_{\text{H}_2\text{SO}_4}^{\text{cond}} \kappa_{\text{H}_2\text{SO}_4}^{\text{cond}} + \dots \end{aligned}$$

We expect loss to be dominated by wall loss and condensation, but it also includes dilution by flow into and out of the chamber  
250 and, potentially, nucleation (or formation of “hidden sulfuric acid” clusters that are not well measured by the  $\text{NO}_3^-$  CIMS (Rondo et al., 2016)).

It is crucial for the calibration experiments to include stages that are almost completely governed by wall loss as well as others where condensation loss is competitive with or even greater than wall loss. This variability and dynamic range robustly disentangles these two crucial parameters and permits accurate determination of both via precise  $\text{H}_2\text{SO}_4$  measurements.

## 255 4.2 Production constraints

The  $\text{H}_2\text{SO}_4$  production rate is nominally proportional to the UV light amplitudes,  $s_{\text{lt}}$ :

$$\begin{aligned} p_{\text{H}_2\text{SO}_4} &= y_{\text{H}_2\text{SO}_4} (c_{\text{SO}_2}, c_{\text{CO}}, c_{\text{H}_2\text{O}}, c_{\text{O}_3}) \mathcal{L}_{\text{lt}}^{\text{cal}} s_{\text{lt}} \\ P_{\text{H}_2\text{SO}_4} &= \mathcal{F}_{\text{H}_2\text{SO}_4}^{\text{cal}} \mathcal{F}_{\text{lt}}^{\text{cal}} p_{\text{H}_2\text{SO}_4} \end{aligned}$$

We break the production into a nominal production rate,  $p_{\text{H}_2\text{SO}_4}$ , and the fully calibrated value  $P_{\text{H}_2\text{SO}_4}$ , which is scaled by the  
260 same  $\text{H}_2\text{SO}_4$  calibration factor,  $\mathcal{F}_{\text{H}_2\text{SO}_4}^{\text{cal}}$  and possibly a slight adjustment for each light calibration,  $\mathcal{F}_{\text{lt}}^{\text{cal}}$ , reflecting any non-linearities propagating through the system with changes to the absolute  $\text{H}_2\text{SO}_4$  levels. However, at this point in the process, the main feature is that we expect  $\text{H}_2\text{SO}_4$  production to be proportional to the light amplitudes, scaled by an action term for each light,  $\mathcal{L}_{\text{lt}}^{\text{cal}}$  (giving the photolysis rate of  $\text{O}_3 \longrightarrow \text{O}_2 + \text{O}(\text{I}\text{D})$  at unit light amplitude) and a yield of  $\text{H}_2\text{SO}_4$  per  $\text{O}(\text{I}\text{D})$  formed,  $y_{\text{H}_2\text{SO}_4}$ , which is a function of several concentrations as well. In practice that function is a photochemical model. The  
265 steady-state balance gives

$$\begin{aligned} P_{\text{H}_2\text{SO}_4} &= L_{\text{H}_2\text{SO}_4} \\ \mathcal{F}_{\text{lt}}^{\text{cal}} p_{\text{H}_2\text{SO}_4} y_{\text{H}_2\text{SO}_4} \mathcal{L}_{\text{lt}}^{\text{cal}} s_{\text{lt}} &= k_{\text{H}_2\text{SO}_4}^{\text{I}} s_{\text{H}_2\text{SO}_4}^{\text{ss}} \end{aligned}$$

## 5 Disaggregating loss terms

The first-order  $\text{H}_2\text{SO}_4$  loss consists almost entirely of wall loss and condensation to particles, which we must disaggregate, and  
270 which can be extended to all gases and particles for neutral conditions and all neutral gases and particles for charged conditions.



## 5.1 Wall loss

Neutral wall loss is driven by turbulence, and for electrically neutral  $\text{H}_2\text{SO}_4$  in a chamber with conductive walls, it is given by:

$$k_i^{\text{wall}} = \frac{2}{\pi} (\text{S:V}) \sqrt{(k_e D_i)} \quad (1)$$

275 where  $D_i$  is the diffusion coefficient of different vapors and particles, S:V is the surface area to volume ratio of the chamber, and  $k_e$  is the nominal eddy mixing inverse timescale for the chamber (McMurry and Grosjean, 1985; Kürten et al., 2014). Here,  $k_{\text{H}_2\text{SO}_4}^{\text{wall}}$  is constrained empirically, and the other terms are known, leaving

$$k_e = \frac{\pi^2}{4} (\text{V:S})^2 \frac{(k_{\text{H}_2\text{SO}_4}^{\text{wall}})^2}{D_{\text{H}_2\text{SO}_4}} \quad (2)$$

This then constrains wall losses for particles given  $D_{d_p}$  Kürten et al. (2015), in practice with the proportionality

$$280 \quad k_i^{\text{wall}} = k_{\text{H}_2\text{SO}_4}^{\text{wall}} \sqrt{\frac{D_i}{D_{\text{H}_2\text{SO}_4}}} \quad (3)$$

This is only valid for electrically neutral conditions – either for neutral species and particles or for charged particles in the absence of electric fields and induction effects (Mahfouz and Donahue, 2020). CLOUD has precisely controlled fields, conductive stainless steel walls and no electrically isolated surfaces where static charge might accumulate; consequently, this condition is met under almost all circumstances. During charged stages there are no electric fields in the chamber, and so wall losses 285 remain governed by this neutral physics, and in practice during neutral stages there are no charged species because they are swept from the chamber essentially as soon as they form. During the cleaning stage there is a significant charge buildup on particles as well as a clearing field, and so the particle losses are in part governed by electrical mobility. This also occurs as a transient when the clearing field turns on for the transition between a charged stage and a neutral stage. When the clearing field is turned on, any charged particles in the chamber are removed quickly, based on their electrical mobility; this transient serves 290 as an important secondary diagnostic constraint indicating the fraction of charged particles in the overall population at the end of that charged stage.

## 5.2 Condensation

The condensation sink frequency measurement relies on accurate measurement (signal) of the number size distribution,  $s_{\text{dist}}$ , and so presents another interconnected calibration factor

$$295 \quad k_{\text{H}_2\text{SO}_4}^{\text{cond}} = \mathcal{F}_{\text{cond}}^{\text{cal}}(d_p) s_{\text{dist}}$$

Here we explicitly show the calibration factor as a function of particle size ( $d_p$ ) because the distribution itself is an amalgamation of measurements from multiple instruments. Condensation is a (first-order) sink for  $\text{H}_2\text{SO}_4$  vapor, but it also drives growth of the particles, and here we shall assume that the particle growth rate,  $s_p^{\text{gr}}$  is rate-limited by the condensation of  $\text{H}_2\text{SO}_4$



vapors. Thus the size distribution (and more importantly the surface-area distribution converted to a condensation-sink distribution) is also governed by the condensation rate of  $\text{H}_2\text{SO}_4$  vapors (along with the nucleation rate, also governed by that vapor concentration).

### 5.2.1 net condensation flux

The net condensation flux of a species with excess vapor concentration,  $c_i^{\text{xs}}$ , and an effective spherical diameter  $d_i$ , to a suspension of identical particles,  $p$ , with number concentration,  $N_p^s$ , and diameter,  $d_p$ , is (Donahue et al., 2019):

$$\begin{aligned}
 305 \quad \Phi_{i,p}^{v,s} &= N_p^s \underbrace{\left( \frac{\pi}{4} (d_p + d_i)^2 \alpha_{i,p} E_{i,p}^\mu \right)}_{\text{cross section: } \sigma_{i,p}} \underbrace{\bar{s}_{i,p} B_{i,p}}_{\text{speed: } s'_{i,p}} c_i^{\text{xs}} \\
 &= N_p^s \pi d_p^2 \underbrace{(\alpha_{i,p} E_{i,p}^\mu \epsilon_{i,p} e_{i,p} B_{i,p})}_{\text{area: } A_p^s} \underbrace{\left( \frac{\bar{s}_i}{4} \right)}_{\text{collision speed: } s_{i,p}^\perp} c_i^{\text{xs}} \\
 &\quad \underbrace{\phi_{i,p}^{v,s} = s_{i,p}^\perp c_i^{\text{xs}}}_{\text{flux per unit surface area: } \phi_{i,p}^{v,s} = s_{i,p}^\perp c_i^{\text{xs}}}
 \end{aligned}$$

$$k_{i,p}^{\text{cond}} = N_p^s \pi d_p^2 s_{i,p}^\perp$$

$$k_i^{\text{cond}} = \int_{-\infty}^{\infty} \underbrace{\left( \frac{d N_p^s}{d \log d_p} \pi d_p^2 s_{i,p}^\perp \right)}_{d\text{CS}/d \log d_p} d \log d_p$$

The terms  $\epsilon_{i,p}$  and  $e_{i,p}$  reflect the finite size of the condensing molecule and the smaller reduced mass of the line-of-centers collision compared to the particle mass (Donahue et al., 2019). The term  $E_{i,p}^\mu$  reflects Van der Waals enhancements above the hard-spheres collision rate to be discussed below (Stolzenburg et al., 2020). The term  $B_{i,p}$  reflects transition-regime gas-phase diffusion limitations and has almost no role for the sub-30 nm particles here. If the vapor is highly supersaturated ( $\text{H}_2\text{SO}_4$  here), then the excess vapor concentration is simply the vapor concentration,  $c_i^{\text{xs}} = c_i^v$ .

### 5.2.2 microphysics of extremely small particles

315 Microphysics accelerates the growth of very small particles above the nominal  $\text{H}_2\text{SO}_4$  condensation speed ( $\bar{s}_i/4$ ). The terms  $(E_{i,p}^\mu \epsilon_{i,p} e_{i,p})$  are enhancements to this nominal speed due to Van der Waals effects (Stolzenburg et al., 2020) as well as the reduced mass and finite size of the condensing molecule. These are all notably important for  $d_p \lesssim 10$  nm, while  $B_{i,p}$  only becomes important as the Knudsen number decreases toward the transition regime ( $Kn \lesssim 1$  or  $d_p \gtrsim 30$  nm). Finally, a non-unit mass accommodation factor,  $\alpha_{i,p} < 1$ , would simply slow growth; as we shall see below there is no evidence for this, so 320 we shall assume  $\alpha_{i,p} = 1$ .

Fig. 5a shows the overall collision adjustment to the nominal  $\text{H}_2\text{SO}_4$  condensation speed,  $\alpha_{i,p} E_{i,p}^\mu \epsilon_{i,p} e_{i,p} B_{i,p} \bar{s}_i/4$ , and Fig. 5b shows the Van der Waals enhancement alone,  $E_{i,p}^\mu$ , using a Hamaker constant (Chan and Mozurkewich, 2001) for  $\text{H}_2\text{SO}_4$  of  $A_{\text{H}_2\text{SO}_4} = 6 \times 10^{-20}$  J. This is consistent with published values (Chan and Mozurkewich, 2001; Stolzenburg et al.,

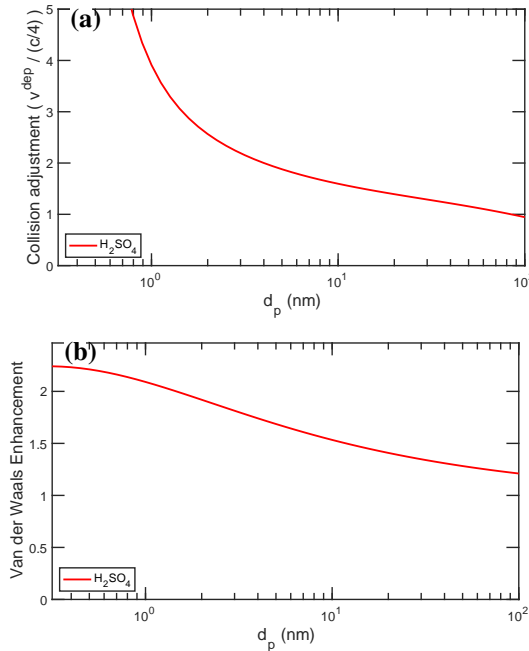


**Figure 5.** Enhancement over simple kinetic condensation vs size for  $\text{H}_2\text{SO}_4$ . (a) All effects adjusting simple vapor condensation speed,  $\bar{s}_{\text{H}_2\text{SO}_4}/4$ . (b) Van der Waals enhancement alone for  $A_{\text{H}_2\text{SO}_4} = 6 \times 10^{-20}$  Joules to give  $E_{\text{H}_2\text{SO}_4}^{\mu} \simeq 1.6$  at  $d_p = 10$  nm.

2020). For visualization purposes, the plotted particle size range extends down to 0.3 nm, which is effectively the small-molecule limit. We also apply the same Van der Waals enhancement to coagulation of  $(\text{NH}_4)_2\text{SO}_4$  particles; coagulation remains smaller than wall loss and ventilation in our microphysical model and so, while the Van der Waals correction is very important for condensation to small particles, it has minimal effect on the particle size distribution for the conditions relevant to this work.

### 5.2.3 calibrating the condensation sink

Fig. 6 shows the observed particle size distributions from combined DMA-train, nano-SMPS, and SMPS data as “bunches of bananas” of both the number distribution and the condensation sink distribution, as well as the resulting integrated number distribution and condensation sink for Run 1833. We apply median filters and interpolants to the scalar values in the lower panels to improve the precision. To match the CPC<sub>2.5</sub> total number, we scale data from the SMPS (for  $d_p \gtrsim 7.2$  nm) by  $\mathcal{F}_{\text{SMPS}}^{\text{cal}} = 1.33$ , consistent with a small undercounting for the SMPS (the peak hues in the distribution are a modestly darker red than in Fig. 2). With this, the integrated distributions match the CPC<sub>2.5</sub> regardless of whether most of the particles are principally small ( $d_p < 10$  nm) or large ( $d_p > 10$  nm). Only when the particles are very small is there some hint of a discrepancy between the CPC<sub>2.5</sub> and the integrated distribution (mostly the DMA train under these conditions). Here some consideration of the CPC<sub>2.5</sub> transmission curve might be warranted, but for the vast majority of the time, with larger particles, the agreement between the

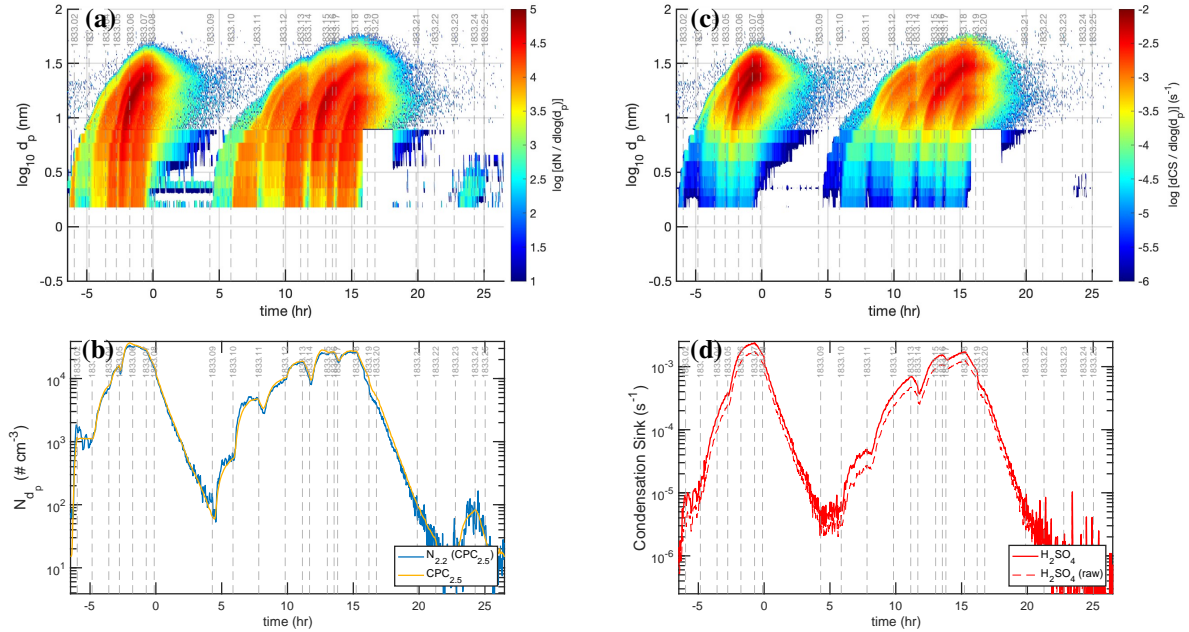


**Figure 6.** Particle measurements after calibration to CPC<sub>2.5</sub> values. (a) Particle size distribution ( $dN/d\log d_p$ ) after calibration. (b) The total particle number for  $d_{\text{mob}} \geq 2.5 \text{ nm}$  ( $d_p \geq 2.2 \text{ nm}$ ) measured with a TSI CPC<sub>2.5</sub> as well as the integrated number distribution after calibration. SMPS data for  $d_p \geq 7.1 \text{ nm}$  are scaled by 1.33 to match the CPC<sub>2.5</sub> data; the constraints are especially strong for loss stages 07-08 and 18-20, where almost all of the particles were  $d_p > 10 \text{ nm}$  (though in portions of stages 18-20 the DMA-train data are missing). (c) condensation sink distribution ( $dCS/d\log d_p$ ) after calibration. (d) The integrated condensation sink after SMPS calibration. The solid red curve shows the condensation sink for  $\text{H}_2\text{SO}_4$  including a Hamaker (Van der Waals) constant of  $6 \times 10^{-20} \text{ J}$  whereas the dashed red curve omits this, revealing a roughly 30 % Van der Waals enhancement.

CPC<sub>2.5</sub> and the integrated size distribution (after correcting for the SMPS undercount) is well better than 10 %, giving high  
340 confidence in the size distribution over time and thus both the total number and the integrated surface area.

Various modes of nucleation and growth are clearly evident during both the UVH and UVX stages. Stage 02, which is neutral with low  $\text{H}_2\text{SO}_4$ , shows little nucleation, and stage 06, which is charged, shows less nucleation than the preceding neutral stage 05. Each of the visible nucleation bursts forms individual nucleation modes, whose growth rates must be proportional to the *absolute* amount of condensation, which in turn depends on the absolute  $\text{H}_2\text{SO}_4$  concentration. During both events, these  
345 bunches of bananas reach a maximum size of  $d_p \simeq 30 \text{ nm}$ .

The Van der Waals term maximizes for objects of the same size (Chan and Mozurkewich, 2001), but the enhancement is substantial throughout the 5-15 nm size range most relevant here, increasing the collision rate by roughly 60 % at 10 nm. Overall the sharp deceleration in collision speed with size shown in Fig. 5a is essential to reproduce the sharp modal shape of the “bunches of bananas” we observe. Without this condensational narrowing the nucleation modes would remain much more  
350 spread out towards lower size. The condensation sink for  $\text{H}_2\text{SO}_4$  obtained from these calibrated size distributions, including



the Van der Waals effect, agrees very closely with the observed gas-phase  $\text{H}_2\text{SO}_4$  signals. Complementary model runs, without the condensational narrowing induced by the Van der Waals term, fail to reproduce these well-defined modes.

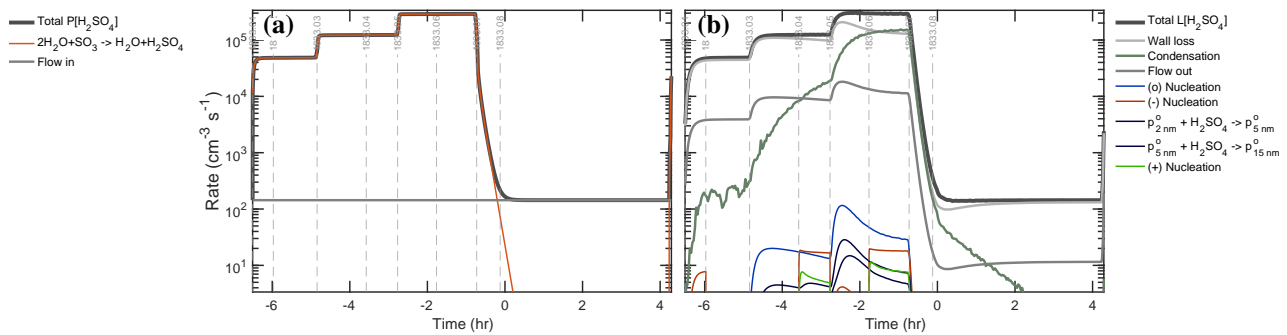
Fig. 6d shows the measured condensation sink vs time for  $\text{H}_2\text{SO}_4$  with (solid) and without (dashed) the Van der Waals correction. The corrected condensation sink, with integrated particle number matching the CPC<sub>2.5</sub> and treatment of the Van der 355 Waals enhancement, provides our best *a-priori* estimate of the condensation contribution to the first-order  $\text{H}_2\text{SO}_4$  loss term.

Fig. 6 and especially Figs 6b and 6d comprise a two-moment objective function to assess the agreement between different measurements and between measurements and simulations incorporating various calibration terms,  $\mathcal{F}_i^{\text{cal}}$ . For an optimal calibration, we would quantify this performance (including some weighting of the variance between the different moments of the simulated and observed distributions) and obtain optimal  $\mathcal{F}_i^{\text{cal}}$  along with a full variance-covariance matrix. Here however we 360 shall restrict ourselves to a “by eye” comparison of these four panels to assess different simulations.

## 6 $\text{H}_2\text{SO}_4$ loss calibration

With the first-order condensation sink calibrated we could assess the production and loss balance of  $\text{H}_2\text{SO}_4$ , assuming that  $P_{\text{H}_2\text{SO}_4} \propto s_{\text{lt}}$  for a given light source,  $\text{lt}$ . Here we show results from a full photochemical model, described in detail below, but at this step in the calibration sequence our focus is on accurate constraint of the first-order loss (largely wall loss and 365 condensation) and precise constraint of  $P_{\text{H}_2\text{SO}_4}$  and thus  $c_{\text{H}_2\text{SO}_4}$ . The actual scale of  $c_{\text{H}_2\text{SO}_4}$  (i.e.  $\mathcal{F}_{\text{H}_2\text{SO}_4}^{\text{cal}}$ ) remains to be determined, presuming (as is the case) that the shape of the concentration vs time remains largely unchanged with modest scaling of the absolute concentration.

Fig. 7 shows the production and loss rate balance for  $\text{H}_2\text{SO}_4$  during the UVH stages of run 1844, including 3 different light intensities over 6 stages followed by two dark stages. This is the first of many process rate analyses from our suite of



**Figure 7.** Production and loss rates of  $\text{H}_2\text{SO}_4$  during the UVH stages. (a) Production rises in 3 steps with UVH intensity in stages 01 – 06 and then drops to near zero with the lights are turned off for stages 07 and 08. A small source of unknown origin is modeled as a constant flow more than 3 orders of magnitude lower than the maximum photochemical production. (b) Losses are dominated by wall deposition (light gray) and condensation (gray-green), with a small contribution from dilution (flow out, dark gray), giving the overall rate balance evident by comparing the two panels. Losses from nucleation itself are evident but extremely small.

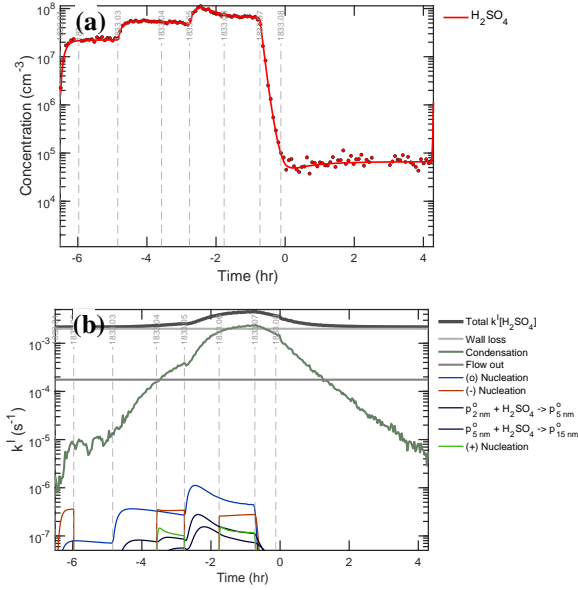


**Figure 8.** (a) H<sub>2</sub>SO<sub>4</sub> concentration measurements (points) and model (curve) during the UVH stages. (b) H<sub>2</sub>SO<sub>4</sub> first-order loss frequency (inverse lifetime). Wall loss defines the minimum loss frequency, with condensation contributing equally during the middle of the sequence. The H<sub>2</sub>SO<sub>4</sub> steady state concentration falls during stages 05 and 06, with the model and measurements agreeing at all times.

370 models; we show production and loss side-by-side with identical *y*-axes so the degree of balance can be assessed directly. Here the production and loss rates balance following a short adjustment after each step in UVH intensity (the loss rates adjust with a timescale given by  $1/k_{H_2SO_4}^1$ ). The production rates are almost entirely photochemical (appearing as hydrolysis, SO<sub>3</sub> + 2H<sub>2</sub>O → H<sub>2</sub>SO<sub>4</sub> + H<sub>2</sub>O in Fig. 7a). The loss rates are predominantly wall loss, with steadily rising condensation and a small (few percent) contribution from dilution. Condensation exceeds wall loss in stage 06. During the “wall loss” stage 07 375 the condensation and wall loss rates remain nearly equal, and so the separation between wall loss and condensation is achieved primarily during stages 01-04, when condensation is at most 10 % of the wall loss rate, making these (precise) level steps important in the separation. The shape of these production and especially loss curves constrains the absolute magnitude of the major loss processes.

380 There is a small unknown source of H<sub>2</sub>SO<sub>4</sub>, modeled here as a constant input flow. It is orders of magnitude weaker than photochemistry when the lights are on and so has no practical effect on the calibration. It could be an instrument background but it is shared by two instruments as seen in Fig. 2b, and because of this and its shape we conclude that it is real, of unknown origin, but negligible.

385 During the most intense nucleation events, nucleation remains less than 1 % of the overall H<sub>2</sub>SO<sub>4</sub> loss. The “nanoparticle” and “cluster” growth terms are part of overall condensation as it is treated in a modal scheme within the photochemical model; this would be double counting the condensation sink but they represent single collisions of H<sub>2</sub>SO<sub>4</sub> with particles comprising



those modes, and growth from one mode to the next requires hundreds to thousands of such collisions. These growth terms are many orders of magnitude smaller than the total condensation sink and so we can run the photochemical model with an externally constrained condensation sink – the measured values shown Fig. 7b – without introducing double counting error.

Fig. 8 compares the modeled and measured  $\text{H}_2\text{SO}_4$  as well as the individual terms comprising the  $\text{H}_2\text{SO}_4$  first-order loss. 390 The condensation frequency shown in Fig. 8b corresponds to the condensation loss rate shown in Fig. 7b. Accurate separation of wall and condensation loss requires that the condensation loss grows to at least equal the wall loss, such as during stages 05-07. This is important for two reasons. First, stage 07 is a so-called “wall loss” stage with no  $\text{H}_2\text{SO}_4$  production, but the condensation sink remains competitive, meaning that  $k^{\text{wall}} + k^{\text{cond}}$  are constrained jointly during this stage. The wall loss itself is more tightly constrained by the steady-state  $\text{H}_2\text{SO}_4$  levels during e.g. stages 02-03, when the condensation sink is 395 negligible. Second, the progressive drop in the steady-state  $\text{H}_2\text{SO}_4$  during stages 05-06 requires this competition between wall and condensation losses and is not consistent with a lower condensation sink (without the Van der Waals enhancement). The particle number (or individual particle surface area) could be increased by 30 % to achieve the same effect, but the condensation sink itself is tightly constrained. Because we regard the CPC<sub>2.5</sub> as accurate and because the Van der Waals effect produces 400 modes with the right shape (discussed below), we conclude that the current constraints are correct (to within roughly 10 %), meaning  $\mathcal{F}_{\text{cond}}^{\text{cal}} \simeq 1.0 \pm 0.1$ . Overall the modeled  $\text{H}_2\text{SO}_4$  matches measurements for all light intensities after the wall loss is constrained (to its nominal value), with  $\tau_{\text{H}_2\text{SO}_4}^{\text{wall}} = 500\text{ s}$  and  $\mathcal{F}_{\text{wall}}^{\text{cal}} \simeq 1.0 \pm 0.1$ .

Fig. 8a shows that the  $\text{H}_2\text{SO}_4$  signals precisely match the expected (modeled) signals, and the lower panel shows the individual contributions to the  $\text{H}_2\text{SO}_4$  loss frequency. The constant (horizontal) wall and dilution frequencies stand in contrast to the evolving condensation loss term. The overall rate balance in Fig. 7 and the precise fit of  $\text{H}_2\text{SO}_4$  in Fig. 8a combine to 405 give a strong and accurate constraint on the two timescales (wall and condensation loss) in Fig. 8b. Even the small depression in the  $\text{H}_2\text{SO}_4$  signal at the start of cleaning stage 08 is consistent with the model – the  $\text{H}_2\text{SO}_4$  steady state increases as the constant (unknown) source is balanced by an increasing lifetime as the condensation sink diminishes, which shows that the 410 small unknown  $\text{H}_2\text{SO}_4$  source is a real signal. The condensation frequency shown here is derived from the measured particle size distribution; however, the overall  $\text{H}_2\text{SO}_4$  first-order loss, and thus the condensation frequency during the middle period of the UVH stages where the total loss rises well above the wall loss timescale, is accurately constrained regardless of any particle measurements.

## 7 Nucleation and growth

The  $\text{H}_2\text{SO}_4$  loss is accurately constrained, in part by the equally well constrained total particle number and size distribution forming the condensation sink. The next step is to determine the absolute  $\text{H}_2\text{SO}_4$  calibration factor required to nucleate and 415 grow those particles to sufficient number and size to form that sink. The condensation sink is determined by the number of particles with surface area – the total suspended surface area – and so it depends on both the nucleation and growth of particles (as well as their sinks). Nucleation and growth are connected of course – without particle formation there is nothing to grow.



To constrain nucleation and growth, we employ two tools. One is a sectional microphysical model described in detail elsewhere (Donahue et al., 2019). The other is a comprehensive gas-phase photochemical model described below that contains 420 a simple modal scheme to represent particles, including ions and charge. The sectional microphysical model does not (yet) represent the charge state of particles. The major connection between gas-phase processes and aerosol microphysics in this experiment is the  $\text{H}_2\text{SO}_4$  vapor concentration and the aerosol condensation sink of that  $\text{H}_2\text{SO}_4$ , and so the different modules can be driven either by modeled or observational data. For example, the microphysical model can be driven by measured  $\text{H}_2\text{SO}_4$  (with a potential calibration factor), and the gas-phase photochemical model can incorporate the observed condensation sink 425 (as shown in Fig. 8b). The two models provide complementary constraints and together enable a comprehensive analysis of the processes connecting the fully coupled system.

Particle sections in the microphysical model have spherical equivalent diameter,  $d_p$ , and track number concentration ( $n_p$ ) and 430 composition via density ( $\rho_p$ ) and constituent specific volume ( $v_{i,p}$ ) and thus constituent mass concentration ( $m_{i,p} = \rho_p v_{i,p}$ ). Density can be specified for each species if the particles have more than one phase, but in this case we assume a single 435 condensed phase in each bin. The model treats condensational growth with a moving sectional algorithm and user-selectable size limits,  $d_{\min} \leq d_p \leq d_{\max}$  and resolution,  $\delta \log_{10} d_p$ . At the end of each growth step the algorithm redistributes particles to the specified sizes, conserving number and mass by distributing particles between the fixed bins below and above each new particle size. The model treats coagulation, again conserving number and mass when the produced particles inevitably fall 440 between the fixed size bins. Finally, the model treats size dependent wall loss and size independent ventilation loss.

435 Because the current microphysical model does not treat particle charge, it cannot treat coagulation or wall loss enhancements due to charge. The most obvious manifestation of enhanced loss is the sudden removal of charged particles when the clearing field is turned on after a stage with charge (e.g. the start of stage 02 and especially stage 05). As already discussed, most of the particles are neutral even during charged stages with substantial ion induced nucleation because the growing particles are neutralized via diffusion (dis)charging. However, at the start of these neutral stages some 10-20 % of the particles are charged 440 (as seen in Fig. 3). We address this empirically by removing a fraction of the particles, independent of size, at the start of these stages. This is crude, but because the fraction removed is small, errors caused by this crude treatment are negligible.

## 7.1 Nucleation

The models treat nucleation with either fixed nucleation rates ( $J$ ) or externally specified vapor concentrations ( $\text{H}_2\text{SO}_4$ ,  $\text{NH}_3$ , 445  $\text{H}_2\text{O}$  and ions). Those may be from observations or, in the case of the microphysical model, from the photochemical model. It is not the purpose of this study to constrain nucleation rates per se, but rather to constrain all other parameters leading up to an accurate determination of the nucleation rates. Here we shall simply adjust a nucleation coefficient in order to reproduce the observed particle number (increase) during each stage. We represent nucleation as formation of either neutral or singly charged clusters  $c^{\circ, -, +}$  via interactions of  $\text{H}_2\text{SO}_4$ ,  $\text{NH}_3$ , and ions ( $n^{\pm}$ ). The nucleation rate is nearly third-order in  $\text{H}_2\text{SO}_4$  and nearly first-order in  $\text{NH}_3$  (Dunne et al., 2016; Gordon et al., 2017); here we treat nucleation as exactly third and first order but then



450 adjust the nucleation coefficients for each stage,  $k_n, k_{\pm}$ .

$$J_{1.7}^{\circ} = k_n c_{\text{H}_2\text{SO}_4}^3 c_{\text{NH}_3}$$

$$J_{1.7}^{\text{ion}} = k_{\pm} c_{\text{H}_2\text{SO}_4}^3 c_{\text{NH}_3} n^{\pm}$$

We assume that the ion-induced channel is linear in the concentration of ions ( $n^{\pm}$ ) and predominantly negative, but we treat a fraction of positive ion nucleation based on the observed depletion of the positive primary ions. The ions themselves are 455 produced via an ion-pair production rate,  $J^{\text{ip}} = 7 \text{ cm}^{-3} \text{ s}^{-1}$ , which as we shall see later is sufficient to sustain a steady state  $c_{\text{n}^-} \simeq c_{\text{n}^+} = 1500 \text{ cm}^{-3}$ , as seen in Fig. 3c. In the microphysical model, nucleated particles are introduced at an initial particle size,  $d_p = 0.8 \text{ nm}$ .

The photochemical model treats ions and thus calculates nucleation directly. The microphysical model does not explicitly treat ions, and so we have two choices. The first choice is to fix the ion concentrations at the observed  $n^- = 1500 \text{ cm}^{-3}$  but to 460 ensure that the derived ion induced nucleation rate does not exceed the ion pair limit by imposing a saturation constraint:

$$J^{\text{iin}} = \frac{1}{\frac{1}{J^{\text{ion}}} + \frac{1}{J^{\text{ip}}}} \quad (4)$$

This has the same effect as the expected depletion of ion concentrations as nucleation becomes a major ion sink, but it omits other possible interactions. The second choice is to use an interpolant of constrained ion concentrations (either from measurements or the photochemical model), with a limit to ensure  $J^{\text{iin}} \leq J^{\text{ip}}$ . As we shall see, nucleation rates from the two models 465 agree well when we apply the saturation constraint, and so that is our default choice.

## 7.2 Condensational growth

The condensation sink contributes to first-order loss of  $\text{H}_2\text{SO}_4$ , but in turn it drives particle growth. While the growth rate is governed by  $\text{H}_2\text{SO}_4$  condensation, co-condensation of other vapors ( $\text{NH}_3$  and perhaps  $\text{H}_2\text{O}$ ) must also be addressed to constrain the growth of the size distribution. We also assume that the measured size distribution shown in Fig. 6 accurately reflects their 470 true size in CLOUD.

The condensation sink is generated both by nucleation (to produce particle number) and growth (to produce particle surface area), which we can constrain with the dual constraints of total particle number (the CPC<sub>2.5</sub>) and condensation sink. For this step we shall restrict ourselves to this UVH stages (01 - 08), as this is sufficient for the constraint, takes less time to simulate, and the figures are easier to read with this narrower time range. Stages 01, 04, and 06 are charged while 02, 03 and 05 are 475 neutral. Stage 08 is a cleaning stage with the beam on 50 % but the clearing field alternating between off and on in order to build up charge on larger particles and then sweep them from the chamber.

### 7.2.1 condensation of volatile species

The condensation flux per unit surface area from the vapor ( $v$ ) to a suspended phase ( $s$ ), of a species ( $i$ ) to a particle population ( $p$ ), is  $\phi_{i,p}^{v,s}$ . This depends on an excess concentration,  $c_{i,p}^{\text{xs}}$ . For effectively non-volatile species, such as sulfuric acid in this case,



480 this is just the vapor concentration:  $c_{i,p}^{\text{xs}} = c_i^v$ . That is further ensured when reactive uptake with unit uptake coefficient ( $\gamma_i^{\text{rxn}} = 1$ ) converts the condensing vapor to a non-volatile salt (in this case ammonium salts,  $\text{H}_2\text{SO}_4 + n\text{NH}_3 \longrightarrow (\text{H}_{2-n}\text{SO}_4) \cdot (\text{NH}_4)_n$ ).

When species are not effectively non-volatile, that in turn depends on the volatility of the vapor species (saturation concentration  $c_i^{\circ}$ ) as well as its activity in the suspended particle ( $a_{i,p}^s$ ).

$$c_{i,p}^{\text{xs}} = c_i^v \left( 1 - \frac{c_i^{\circ}}{c_i^v} a_{i,p}^s \right)$$

485  $a_{i,p}^s = K_{i,p} \gamma_{i,p} x_{i,p}$

Here that applies to both ammonia (via reactive uptake) and water. The Kelvin term accounts for increased vapor pressure over highly curved small particles. This can be expressed in terms of a “decadal Kelvin diameter”,  $d_{K10}$ , which is the diameter at which the vapor pressure is a factor of 10 higher than over a flat surface.

$$\log_{10} K_{i,p} = \left( \frac{d_{K10}}{d_p} \right) + O\left( \frac{d_{K10}}{d_p} \right)^2 + \dots$$

490  $d_{K10} = 0.434 d_K; \quad d_K = \left( \frac{4\sigma_p m_i}{k_B T \rho_p} \right) = \left( \frac{4\sigma_p V_i}{RT} \right)$

For water, with  $M_i \simeq 18$  amu,  $\sigma_p \simeq 80 \text{ mN m}^{-1}$  and  $\rho_p \simeq 1000 \text{ kg m}^{-3}$ ,  $d_{K10} = 1 \text{ nm}$ .

### 7.2.2 growth rate

The model is driven by the condensation flux, but it is useful to consider the growth rate. This speed ( $s_{i,p}^{\text{gr}}$  assuming a particle with spherical equivalent  $d_p$ ) due to the flux,  $\phi_{i,p}^{v,s}$ , of a constituent with molar mass  $M_i$  into a phase with density  $\rho_p$ , and thus 495 with molar volume  $v_i = M_i / \rho_p$ , is:

$$s_{i,p}^{\text{gr}} = 2 \frac{M_i}{\rho_p} \phi_{i,p}^{v,s} = 2 v_i \phi_{i,p}^{v,s}; \quad s_p^{\text{gr}} = \sum_i s_{i,p}^{\text{gr}}$$

The factor of 2 is because growth extends the diameter by extending the radius symmetrically.

### 7.2.3 co-condensation of abundant vapors

For ternary  $\text{H}_2\text{SO}_4$ ,  $\text{NH}_3$  and  $\text{H}_2\text{O}$  nucleation and growth, condensational growth is rate limited by  $\text{H}_2\text{SO}_4$  condensation but 500 is accompanied by  $\text{NH}_3$  and  $\text{H}_2\text{O}$ . This can have two subtly different manifestations: vapors can co-condense with a fixed stoichiometric ratio to  $\text{H}_2\text{SO}_4$  via reactive uptake (i.e. 2:1 for  $\text{H}_2\text{SO}_4 + 2\text{NH}_3 \longrightarrow (\text{NH}_4)_2 \cdot \text{SO}_4$ ); or vapors can continuously approach equilibrium with the condensed-phase solution to maintain equal activities in both vapor and condensed phases (i.e.  $a_{\text{H}_2\text{O}} \rightarrow \text{RH}/100$ ). In either event, the other vapors will contribute to the particle volume in proportion to their molar volume, so scaled by their molar mass,  $M_i / M_{\text{H}_2\text{SO}_4}$ .

505 Here we assume the ammonia co-condenses with a 2:1 stoichiometry but is in sufficient excess to maintain its equilibrium composition (activity) in the growing particles, regardless of whether they are wet or dry and regardless of size: Specifically, if



NH<sub>3</sub> condenses with a stoichiometry of  $s_{\text{NH}_3}$  with respect to H<sub>2</sub>SO<sub>4</sub>:

$$\begin{aligned}s_p^{\text{gr}} &= 2 \left( \frac{M_{\text{H}_2\text{SO}_4}}{\rho_p} \phi_{\text{H}_2\text{SO}_4,p}^{v,s} + \frac{M_{\text{NH}_3}}{\rho_p} \phi_{\text{NH}_3,p}^{v,s} \right) \\ &= 2 \left( \frac{M_{\text{H}_2\text{SO}_4} + s_{\text{NH}_3} M_{\text{NH}_3}}{\rho_p} \right) \phi_{\text{H}_2\text{SO}_4,p}^{v,s}\end{aligned}$$

510 However, the very smallest particles, visible in an Atmospheric Pressure Interface Time of Flight Mass Spectrometer (APITOF), have been shown to grow with a 1:1 stoichiometry (i.e. as ammonium bisulfate) (Kirkby et al., 2011); this is presumably due to a Kelvin effect for extremely small particles (Ahlm et al., 2016). It is not yet known over what size range  $s_{\text{NH}_3}$  changes from 1 to 2, but here we assume it is below the size range where our analysis is most sensitive to our constraints on growth rate. None 515 the less the smallest particles are likely to be ammonium bisulfate, which may well matter to the overall behavior at any given relative humidity.

Condensation of H<sub>2</sub>O represents a binary uncertainty in these calculations. At thermodynamic equilibrium and 58 % RH, the particles would grow as dry (NH<sub>3</sub>)<sub>2</sub> · SO<sub>4</sub>, as this is well below the 80 % deliquescence relative humidity (DRH), which persists down to  $d_p \simeq 6$  nm (Lei et al., 2020). If the particles are dry, they contain essentially no water and have a hygroscopic growth factor very near 1.0 and  $s_{\text{H}_2\text{O}} \simeq 0$  (Bezantakos et al., 2016). This would also imply that any sample drying during sampling 520 (i.e. due to dry sheath flow) would have minimal effect on the already dry particles.

However, the particles initially grow as ammonium bisulfate, and particles with stoichiometry between 1:1 and 1.5:1 have a DRH as low as 37 % down to  $d_p = 15$  nm, (Mifflin et al., 2009). The nucleated particles may well grow as aqueous (deliquesced) particles and so remain wet during growth even once the stoichiometry increases to 2:1, because 58 % RH is well above the efflorescence relative humidity of ammonium sulfate. Further, the growth rate of particles observed under similar 525 conditions in CLOUD is independent of HN<sub>3</sub> for  $1 \lesssim \chi_{\text{NH}_3} < 1000$  ppt (Stolzenburg et al., 2020), thus encompassing pure sulfuric acid droplets. Because H<sub>2</sub>O almost certainly condenses to H<sub>2</sub>SO<sub>4</sub> droplets at very low NH<sub>3</sub>, we conclude that the particles in Run 1833 were also wet. If they did grow along the meta-stable deliquescence branch as a deliquesced aqueous solution, their diameter growth factor was roughly 1.2 (depending on size) (Lei et al., 2020; Vlasenko et al., 2017), and they sustained a water activity of  $a_{\text{H}_2\text{O}}^s = 0.58$ . This will also have implications for the accuracy of the measured particle size distribution, as 530 the SMPS measurement may involve some drying in the DMA column (Stolzenburg et al., 2020). However, the condensation sink remains precisely constrained by the directly observed contribution to first-order H<sub>2</sub>SO<sub>4</sub> vapor loss.

Our treatment of water condensation in the growth will be to sustain the water activity via simplified thermodynamics, but consideration of hygroscopic growth is useful to check this treatment. The growth factor can be split into two contributing elements. One is the density difference between the aqueous and dry particles; the other is the contribution of condensing 535 water to the overall molar volume. Both affect volume and so the volume growth factor  $f_{\text{gr}}^3$ .

$$\begin{aligned}f_{\text{gr}}^3 &= \left( \frac{\rho_{\text{dry}}}{\rho_{\text{wet}}} \right) \times \\ &\left( \frac{M_{\text{H}_2\text{SO}_4} + s_{\text{NH}_3} M_{\text{NH}_3} + s_{\text{H}_2\text{O}} M_{\text{H}_2\text{O}} + \sum_i s_i M_i}{M_{\text{H}_2\text{SO}_4} + s_{\text{NH}_3} M_{\text{NH}_3}} \right)\end{aligned}$$



$$= \left( \frac{\rho_{\text{dry}}}{\rho_{\text{wet}}} \right) \left( 1 + \frac{s_{\text{H}_2\text{O}} \sum_i s_i M_i}{M_{\text{H}_2\text{SO}_4} + s_{\text{NH}_3} M_{\text{NH}_3}} \right)$$

The term  $\sum_i s_i M_i$  accounts for other constituents, such as  $\text{H}^+$  and  $\text{HSO}_4^-$ , which we lump into  $\text{H}_2\text{O}$  and  $\text{H}_2\text{SO}_4$  and otherwise neglect in this simple treatment. This is reasonable for neutral  $(\text{NH}_4)_2\cdot\text{SO}_4$ . Thus, for a known growth factor, the molar ratio of  $\text{H}_2\text{O}$  to  $\text{H}_2\text{SO}_4$  is

$$s_{\text{H}_2\text{O}} = \left( f_{\text{gr}}^3 \left( \frac{\rho_{\text{wet}}}{\rho_{\text{dry}}} \right) - 1 \right) \left( \frac{M_{\text{H}_2\text{SO}_4} + s_{\text{NH}_3} M_{\text{NH}_3}}{M_{\text{H}_2\text{O}}} \right)$$

For example, at 58 % RH and  $s_{\text{NH}_3} = 2$ , the growth factor at  $d_p = 100$  nm is  $f^{\text{gr}} = 1.27$  (Lei et al., 2020). With  $\rho_{\text{dry}} = 1770 \text{ kg m}^{-3}$  and  $\rho_{\text{wet}} = 1350 \text{ kg m}^{-3}$ , this gives  $s_{\text{H}_2\text{O}} = 4.12$ , close to the EAIM value of  $s_{\text{H}_2\text{O}} = 4.36$  (Friese and Ebel, 2010). Tandem-DMA measurements of  $(\text{NH}_4)_2\cdot\text{SO}_4$  hygroscopic growth show growth factors consistent with established thermodynamics and a size dependence affected by a Kelvin term (Lei et al., 2020). For this reason we shall assume that the particles rapidly equilibrate with water vapor to maintain a particle activity equal to the ambient RH (58 % in this case).

To find the equilibrium water activity, we equilibrate each particle section after it grows due to condensation of  $\text{H}_2\text{SO}_4$  and so find the molar ratio of  $\text{H}_2\text{O}$  to  $\text{H}_2\text{SO}_4$ ,  $s_{\text{H}_2\text{O}}$ . The mole fraction of water is

$$550 \quad x_{\text{H}_2\text{O}} = \frac{s_{\text{H}_2\text{O}}}{1 + s_{\text{NH}_3} + s_{\text{H}_2\text{O}}}$$
$$\frac{1}{x_{\text{H}_2\text{O}}} = \left( 1 + \frac{1 + s_{\text{NH}_3}}{s_{\text{H}_2\text{O}}} \right)$$

so the molar ratio of water to  $\text{H}_2\text{SO}_4$  is

$$s_{\text{H}_2\text{O}} = \frac{1 + s_{\text{NH}_3}}{\frac{1}{x_{\text{H}_2\text{O}}} - 1}$$
$$= x_{\text{H}_2\text{O}} \frac{1 + s_{\text{NH}_3}}{1 - x_{\text{H}_2\text{O}}}$$

555 This is then governed by the water activity, including the Kelvin term and any activity coefficient,  $\gamma_{\text{H}_2\text{O},p}$ .

$$x_{\text{H}_2\text{O},p} = \frac{a_{\text{H}_2\text{O}}}{\gamma_{\text{H}_2\text{O},p} K_{\text{H}_2\text{O},p}}$$

A full and accurate model requires (iterative) treatment of the thermodynamics (for example in the model MABNAG (Yli-Juuti et al., 2013; Ahlm et al., 2016)), but we find that simplified treatment with just  $\text{H}_2\text{SO}_4$ ,  $\text{NH}_3$  and  $\text{H}_2\text{O}$ , assuming  $\gamma_{\text{H}_2\text{O},p} \simeq 1$  reasonably reproduces the observed size-dependent growth factors for ammonium sulfate (Lei et al., 2020). For our default analysis, we shall thus assume that  $\text{NH}_3$  condenses with a constant ratio to  $\text{H}_2\text{SO}_4$  of 2:1 and water vapor equilibrates with particles to maintain  $a_{\text{H}_2\text{O}} = RH$ , with the wet particle density fixed at  $\rho_{\text{wet}} = 1350 \text{ kg m}^{-3}$  and a surface tension  $\sigma_p = 79 \text{ mN m}^{-1}$  (Hyvärinen et al., 2005).

### 7.3 Coupled nucleation and growth simulations

We simulate the evolving particle size distribution with nucleation and condensation driven by  $\text{H}_2\text{SO}_4$ , finding the nucleation 565 coefficients for each stage and scaling the sulfuric acid concentration by  $\mathcal{F}_{\text{H}_2\text{SO}_4}^{\text{cal}}$ . Nucleation governs total particle number

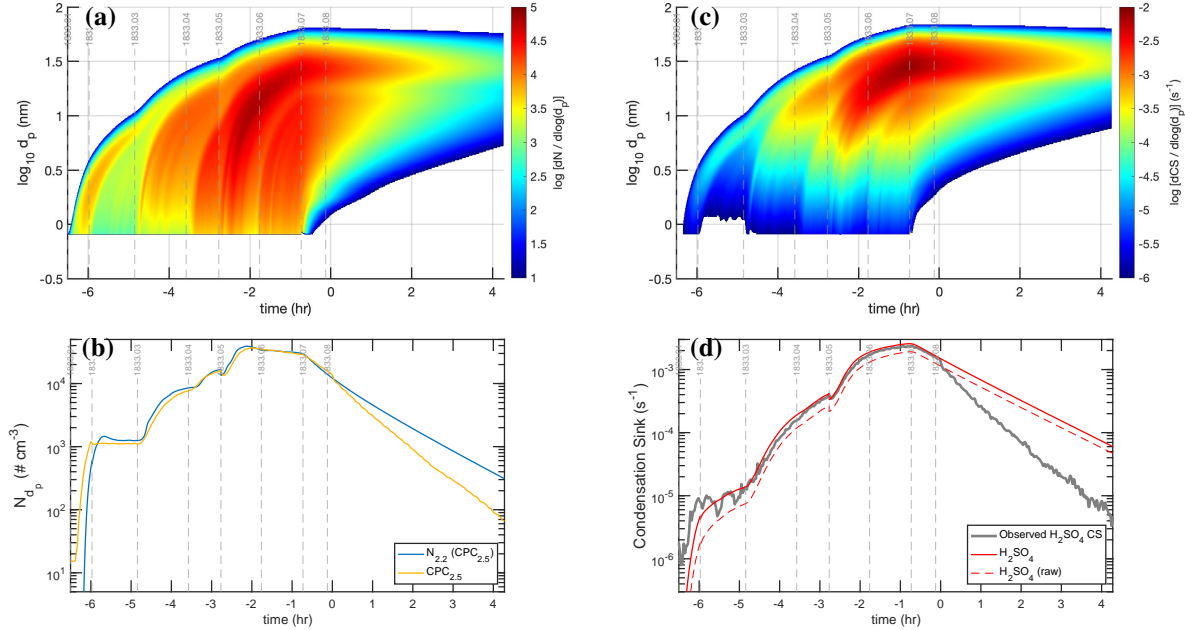


**Figure 9.** Optimal modeled particle size and corresponding condensation sink distributions with wet  $(\text{NH}_4)_2 \cdot \text{SO}_4 \cdot (\text{H}_2\text{O})_n$  growth, and their agreement with measurements. (a) Simulated particle size distribution ( $dN/d\log d_p$ ) for optimal parameters, with empirical nucleation coefficients and an  $\text{H}_2\text{SO}_4$  calibration factor of 1.2. (b) Simulated (blue) and observed (gold) total particle number measurable by a CPC<sub>2.5</sub>. The simulation for the most part agrees within 10 % of the observations, although it falls short during the low  $\text{H}_2\text{SO}_4$  neutral stage 02. The simulation also does not include enhanced losses of charged particles and so misses the dip at the start of stage 05 as well as the accelerated loss during the cleaning stage 08. (c) Simulated condensation-sink distribution ( $d\text{CS}/d\log d_p$ ). (d) Simulated (red) and observed (gray) condensation sink. Simulated values are shown both with (solid) and without (dashed) a Van der Waals correction; the observed values include the correction; the condensation sink is reproduced with good fidelity aside from the enhanced loss during the cleaning stage, which was not simulated. Other than the low-intensity stages (01 and 02), charged and neutral nucleation are competitive because charged nucleation is limited by ion-pair production. That saturation value serves as an additional constraint on the nucleation parameters.

(balanced by deposition and some coagulation), while growth rate-limited by  $\text{H}_2\text{SO}_4$  condensation determines the condensation sink associated with that total number. Because the growth and nucleation are coupled in this way, we determine a nucleation coefficient for each stage to optimally match the particle number production during that stage (including wall and condensation loss of course) and then to constrain  $F_{\text{H}_2\text{SO}_4}^{\text{cal}}$  based on growth of the observed particle number to reproduce the observed condensation sink.

### 7.3.1 calibrated model with wet $(\text{NH}_4)_2 \cdot \text{SO}_4 \cdot (\text{H}_2\text{O})_n$ growth

If we assume that  $\text{H}_2\text{SO}_4$  condensation governs particle growth as wet  $(\text{NH}_4)_2 \cdot \text{SO}_4 \cdot (\text{H}_2\text{O})_n$ , the nominal (independently calibrated)  $\text{H}_2\text{SO}_4$  nearly matches the observed growth rate. Specifically, our best estimate is  $F_{\text{H}_2\text{SO}_4}^{\text{cal}} = 1.2 \pm 0.1$ , summarized in Fig. 9. Fig. 9a shows the observed particle size distribution and Fig. 9b shows the integrated particle number for  $d_p \geq 2.2 \text{ nm}$

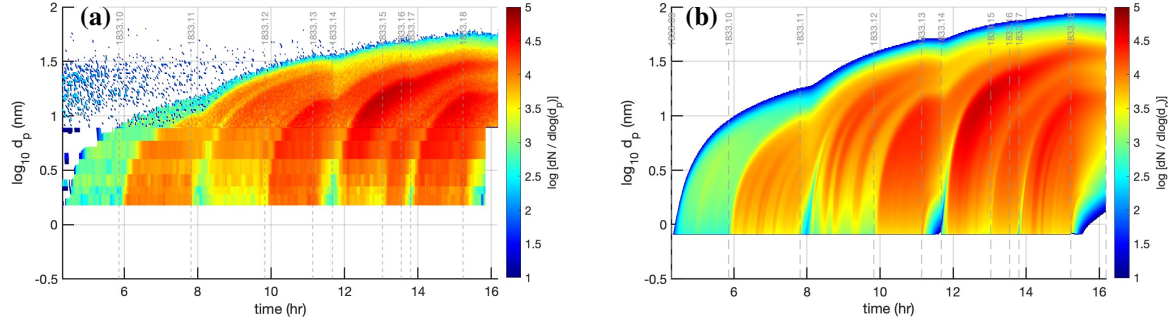


**Figure 10.** Observed (a) and modeled (b) particle size distribution during the UVX stages of Run 1833 with optimized parameters. These include a factor of 1.2 scaling of  $\text{H}_2\text{SO}_4$  and empirical nucleation rates, as well as hygroscopic growth of wet  $(\text{NH}_4)_2 \cdot \text{SO}_4 \cdot (\text{H}_2\text{O})_n$ . Essentially all the features of the observations are reproduced by the simulation with good fidelity, including the timing, intensity, growth rate, and final size of the nucleation bursts during each stage.

575 along with the observed CPC<sub>2.5</sub> number. For this simulation we worked through the stages, adjusting the nominal nucleation  
 coefficients (third order in  $c_{\text{H}_2\text{SO}_4}$ ) to match the CPC<sub>2.5</sub> observations (Fig. 9b) and then adjusting  $\mathcal{F}_{\text{H}_2\text{SO}_4}^{\text{cal}}$  to match the observed  
 condensation sink (Fig. 9d). Fig. 9c shows the corresponding condensation sink distribution and Fig. 9d shows the modeled and  
 observed condensation sink, with the calibrated Hamaker Constant  $A_{\text{H}_2\text{SO}_4} = 6 \times 10^{-20}$  J, growth as wet  $(\text{NH}_4)_2 \cdot \text{SO}_4 \cdot (\text{H}_2\text{O})_2$   
 rate-limited by H<sub>2</sub>SO<sub>4</sub> condensation, and nucleation described below. The overall agreement for particle number, growth rate,  
 580 and condensation sink remains within 10 % throughout, with the exception of losses during the cleaning stage (08), which this  
 neutral microphysical model cannot reproduce. The very initial particle burst during stage 01 is also delayed, possibly because  
 we treat the CPC<sub>2.5</sub> cutoff as a step function but the instrument has some sensitivity to smaller particles.

In Fig. 10a we show the observed size distribution for the UVX stages and in Fig. 10b we reproduce the modeled size distribution, again with  $\mathcal{F}_{\text{H}_2\text{SO}_4}^{\text{cal}} = 1.2$ . This confirms the excellent model-measurement agreement for a different light source  
 585 but shows minor differences. The empirical nucleation coefficients are for the most part similar to those for the UVH stages, and in all but one case (the medium intensity neutral stage 11), we found an optimal match with observed particle number with a small increase compared to the UVH stages. This is not surprising. The UVX light source is less uniform than the UVH source (Kupc et al., 2011), meaning  $P_{\text{H}_2\text{SO}_4}$  will also be less homogeneous. This in turn will contribute to (small) inhomogeneities in  $c_{\text{H}_2\text{SO}_4}$ . Particle growth is slow and so uniform throughout the chamber. Because the  $\text{H}_2\text{SO}_4$  calibration factors are identical for  
 590 each case, we conclude that the measurements accurately reflect the average concentration. However, nucleation is (roughly) third order in  $\text{H}_2\text{SO}_4$  and thus much more sensitive to inhomogeneity; this will tend to enhance the overall average nucleation rate as well.

Overall, we find excellent agreement with the observations after only modest (20 %) adjustment in the  $\text{H}_2\text{SO}_4$  calibration assuming the growing particles are wet and the size distribution measurement is accurate. A larger Hamaker constant would 595 enhance growth, but it would also lower the  $\text{H}_2\text{SO}_4$  lifetime, which we have already constrained (though a full optimization would certainly show co-variance here). However, significant Van der Waals attraction is essential for the overall appearance of



the size distribution – the sharply dropping growth rates vs size shown in Fig. 5a are crucial for the emergence of sharp modes even with constant nucleation and growth, as a constant flux vs size will form modes via condensational narrowing.

### 7.3.2 nucleation coefficients

600 We find good agreement for the overall particle number distribution with nucleation rate coefficients that remain nearly constant as the  $\text{H}_2\text{SO}_4$  and ion concentrations vary, confirming that the particle formation is roughly third-order in  $\text{H}_2\text{SO}_4$  and first-order in ions as expected. For  $c_{\text{H}_2\text{SO}_4} \simeq 6 \times 10^7 \text{ cm}^{-3}$ , we find  $k_{\text{neut}} \simeq 1.6 \times 10^{-33} \text{ cm}^{12} \text{ s}^{-3}$  and  $k_{\text{ion}} \simeq 8.5 \times 10^{-36} \text{ cm}^{15} \text{ s}^{-3}$ .

Fig. 3 shows that, while the AIS data during ion-induced nucleation show large depletion of negatively charged primary ions, they also show some depletion of positively charged primary ions. Indeed, at high  $\text{NH}_3$  concentrations, ion-induced nucleation 605 of  $\text{H}_2\text{SO}_4 - \text{NH}_3$  is known to proceed with both positive and negative ions (Kirkby et al., 2011). A model incorporating primary ion losses is required to explore this further, which we incorporate into our gas-phase kinetic simulation. Based on that model (discussed below) we conclude that negative nucleation is 90 % of the ion-induced pathway and positive nucleation comprises the remaining 10 %. With these coefficients, both the growth (constraining  $\text{H}_2\text{SO}_4$ ) and the total particle number (constraining nucleation) are simulated with good fidelity as shown in Fig. 10.

610 Fig. 11 shows observed and modeled size distributions at roughly -1.47 h during stage 06 (the high light intensity charged stage). The data show clear signs of three modes, with minima at  $d_p \simeq 9 \text{ nm}$  and  $d_p \simeq 20 \text{ nm}$ . There is a hint of a maximum at 5 nm (this is the burst from stage 06 itself), a major maximum at 17 nm (this is the intense burst from the neutral stage 05) and a final maximum at 23 nm (from stage 04, with the stage 03 burst along its leading edge). The simulations also shows 615 these features, with a much clearer maximum near 5 nm, the main 17 nm mode and a shoulder near 23 nm. In the simulation the larger two modes have merged due to numerical diffusion, but the corresponding features over time in Fig. 10 are clearly evident.

620 A final feature in Fig. 11 is the steady increase in the size distribution for  $1 \text{ nm} < d_p < 5 \text{ nm}$ . This is caused by condensational narrowing at a steady nucleation rate and growth flux,  $J_{d_p}$  over this size range. This would not emerge without the decreasing condensation speed with size shown in Fig. 5. Largely because of the (diminishing) Van der Waals enhancement, the condensation speed decreases with size and so the number distribution must increase to compensate and keep the overall growth flux constant (in the absence of losses). This is condensational narrowing. Without these effects, simulations predict a much flatter distribution during constant nucleation rate simulations. Only coagulation would erode the smaller particles, and coagulation is a secondary contributor under these conditions.

### 7.4 Implications of microphysical calibration

625 Our findings based on the particle microphysics are quantitatively consistent with those of Stolzenburg et al. (2020). Specifically, we find that we can reproduce CLOUD observations of particle growth governed by  $\text{H}_2\text{SO}_4$  condensation using a Van der Waals enhancement for that  $\text{H}_2\text{SO}_4$  condensation of  $6 \times 10^{-20} \text{ J}$ , which is slightly higher than the  $4 \times 10^{-20} \text{ J}$  used in that work. We do find best agreement with an  $\text{H}_2\text{SO}_4$  calibration factor of 1.2, but this is within error of the Stolzenburg et al. (2020) analysis as well as the very difficult  $\text{H}_2\text{SO}_4$  calibration itself (Kürten et al., 2012). However, this is contingent on the

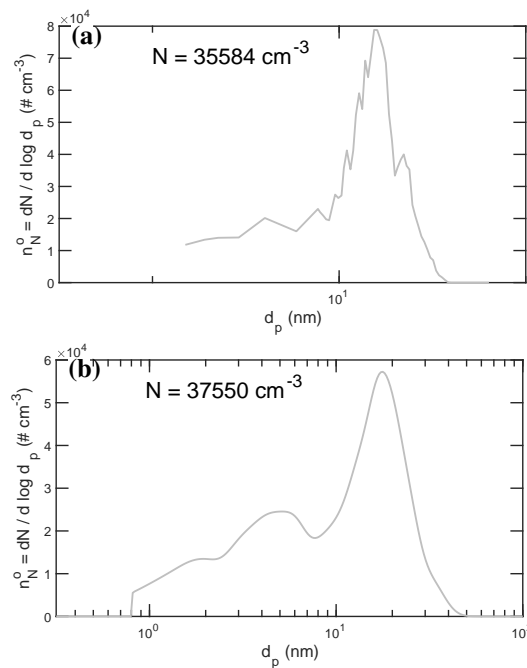


**Figure 11.** Comparison of measured and simulated size distributions near -1.47 h during stage 06. (a) Measured size distribution, combining DMA train and scaled SMPS values, with suspended surface area  $S_p = 2.3 \times 10^{-5} \text{ m}^2 \text{ m}^{-3}$ . (b) Simulated size distribution with the optimized parameters described here, with suspended surface area  $S_p = 2.5 \times 10^{-5} \text{ m}^2 \text{ m}^{-3}$ . Features of 3 distinct modes are evident in the observations and simulation, at the appropriate particle diameters. The steady increase in particles with increasing size for  $1 \text{ nm} < d_p < 5 \text{ nm}$  reflects nearly steady nucleation and growth flux ( $J_{d_p}$ ) because of the condensational narrowing associated with the declining collision speed associated with the Van der Walls effect on the collision cross section.

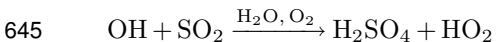
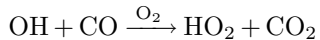
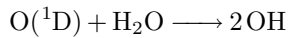
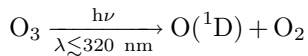
630 growing particles containing considerable water, with a volume growth factor of 1.6, consistent with the deliquescence branch of ammonium sulfate, even though RH never exceeded the deliquescence relative humidity of ammonium sulfate. This is also consistent with the findings of Stolzenburg et al. (2020), who reported no dependence of growth rates on  $\text{NH}_3$  under identical conditions.

## 8 Gas-phase photochemistry

635 We now turn to gas-phase behavior of  $\text{H}_2\text{SO}_4$  – this is almost the only connecting point between the particle (microphysical) constraints and the gas-phase photochemical constraints, including the desired photolysis actinometry. Once the absolute  $\text{H}_2\text{SO}_4$  calibration is constrained, then it is possible to peel back the layers to calibrate the photolysis rates and light amplitudes. The original purpose of Run 1833 was light calibration – to use accurately measured  $\text{H}_2\text{SO}_4$  along with precisely measured amplitudes from several light sources to determine the calibration factors for the volume averaged actinic flux of each light in  
640 CLOUD.



Photolysis drives a nominal set of reactions that produce  $\text{H}_2\text{SO}_4$



The production,  $P_{\text{H}_2\text{SO}_4}$ , is really a complicated function of the light amplitude comprising a photochemical box model, with production by design largely from  $\text{OH} + \text{SO}_2$  and  $\text{OH}$  in turn largely produced by  $\text{O}_3$  photolysis. The absolute light calibration factors also scale almost linearly with the (estimated)  $\text{CO}$ , which is the major  $\text{OH}$  sink. We have already tightly constrained the first-order  $\text{H}_2\text{SO}_4$  loss terms, and here the calibrated condensation sink discussed above is used in the photochemical model 650 via an interpolant.

In CLOUD, both  $\text{O}_3$  and  $\text{SO}_2$  are maintained by adding a steady flow into the continuously stirred reactor, and the resulting mixing ratios are shown in Fig. 4. While these are fairly stable, there is obvious variability that is also evidently associated with light intensity. The ozone mixing ratio rises by more than 10 % during stages 01 – 06 as the  $\text{Hg-Xe}$  lamps approach full intensity, before relaxing back during the dark wall-loss and cleaning stages (07 and 08). It also declines modestly during 655 stage 20 when the 385 nm LEDs are on at full power. The  $\text{SO}_2$  mixing ratio drops by roughly 10 % during stages 01 – 06 but declines by more than 30 % during stage 20, reaching a steady state in a timescale similar to the wall-loss timescale for  $\text{H}_2\text{SO}_4$ . At a minimum it is important to interpolate these observed mixing ratios, but reproducing them in the photochemical model is a more satisfying goal.

The full photochemistry used for  $\text{HO}_x$  calibration to constrain  $j_{\text{O}(\text{^1D})}$  is listed in Appendix A1. The key reactions first 660 establish a steady state of  $\text{O}(\text{^1D})$ , with  $c_M = c_{\text{N}_2} + c_{\text{O}_2}$  and quenching rate coefficient  $k_q$  (actually slightly different for  $\text{N}_2$  and  $\text{O}_2$ ):

$$c_{\text{O}(\text{^1D})}^{\text{ss}} = \underbrace{j_{\text{O}(\text{^1D})} c_{\text{O}_3}}_{P_{\text{O}(\text{^1D})}} \underbrace{(k_q c_M + k_{\text{H}_2\text{O}} c_{\text{H}_2\text{O}})}_{\tau_{\text{O}(\text{^1D})}}^{-1}$$

Because the  $\text{H}_2\text{O}$  reaction rate coefficient is gas kinetic but the quenching coefficients are roughly one in ten collisions, when the water vapor mixing ratio is about 0.01 (typical of room temperature and 50 % RH), about 10 % of the  $\text{O}(\text{^1D})$  is converted 665 to  $\text{OH}$ . This in turn establishes an  $\text{OH}$  steady state within roughly 1 s:

$$c_{\text{OH}}^{\text{ss}} = (2 k_{\text{O}(\text{^1D})} c_{\text{H}_2\text{O}} c_{\text{O}(\text{^1D})}) \tau_{\text{OH}}$$

$$\tau_{\text{OH}} = (k_{\text{CO}} c_{\text{CO}} + k_{\text{O}_3} c_{\text{O}_3} + k_{\text{SO}_2} c_{\text{SO}_2} + \dots)^{-1}$$

The predominant  $\text{OH}$  sink is  $\text{CO}$ , with a few percent reacting with  $\text{SO}_2$ . Finally, this produces  $\text{H}_2\text{SO}_4$ , with a steady state established in at most the wall timescale (of order 10 minutes):

670  $c_{\text{H}_2\text{SO}_4}^{\text{ss}} = (k_{\text{SO}_2} c_{\text{SO}_2} c_{\text{OH}}) \tau_{\text{H}_2\text{SO}_4}$

$$\tau_{\text{H}_2\text{SO}_4} = (k_{\text{H}_2\text{SO}_4}^{\text{wall}} + k_{\text{H}_2\text{SO}_4}^{\text{cond}} + \dots)^{-1}$$

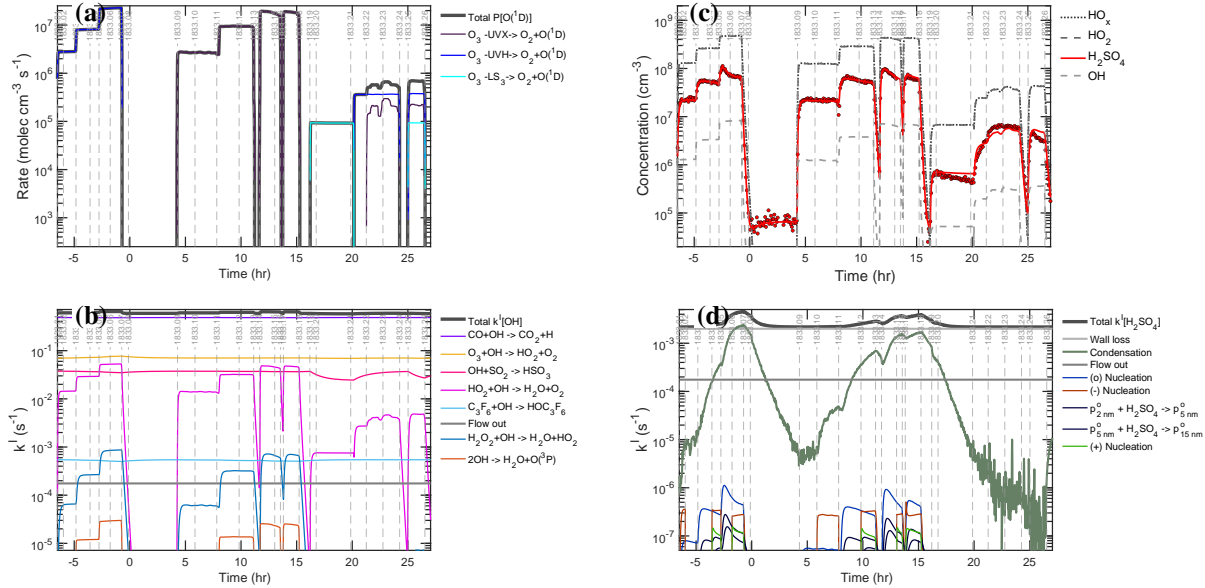


**Figure 12.** Actinometry calibration, with production and loss terms associated with H<sub>2</sub>SO<sub>4</sub> based on corrected H<sub>2</sub>SO<sub>4</sub> ( $\mathcal{F}_{\text{H}_2\text{SO}_4}^{\text{cal}} = 1.1$ ). (a) Primary, calibrated photolysis rates producing O(1D) from 3 different light sources. (b) Contributions to the OH first-order loss (lifetime). (c) Measured and modeled H<sub>2</sub>SO<sub>4</sub> (with modeled HO<sub>2</sub> and OH); (d) Contributions to the H<sub>2</sub>SO<sub>4</sub> first-order loss (lifetime). Photolysis rates are calibrated based on the smoothed light amplitudes shown here, with calibration coefficients adjusted to give optimal agreement with H<sub>2</sub>SO<sub>4</sub>. The H<sub>2</sub>SO<sub>4</sub> behavior is reproduced with excellent fidelity, including timing and amplitude of depletion associated with the increased condensation sink, which is clearly evident in the H<sub>2</sub>SO<sub>4</sub> lifetime as well. This in turn means the average OH concentration is known, and from OH loss the balanced production constrains O(1D) photolysis.

Overall, the fraction of O<sub>3</sub> photolysis toward O(1D) that forms H<sub>2</sub>SO<sub>4</sub> is only a few per mil.

Fig. 12 shows the major contributing to gas-phase closure throughout Run 1833. This includes O(1D) production tied to measured light amplitudes, the OH lifetime, the H<sub>2</sub>SO<sub>4</sub> simulated and measured concentrations (along with simulated HO<sub>2</sub> and OH) and finally the H<sub>2</sub>SO<sub>4</sub> lifetime. With the first-order loss of H<sub>2</sub>SO<sub>4</sub> well constrained, the absolute H<sub>2</sub>SO<sub>4</sub> concentration in Fig. 12 is scaled by  $\mathcal{F}_{\text{H}_2\text{SO}_4}^{\text{cal}} = 1.1$ . Almost all features of the H<sub>2</sub>SO<sub>4</sub> time trace are reproduced with good fidelity, including the downturn in stage 05 (both the timing and amplitude) and the undershoot from the (unknown) dark H<sub>2</sub>SO<sub>4</sub> source in stage 08 (which we simulate as a constant flow). That undershoot is caused by extra loss – a residual condensation sink from suspended particles. For the full span of stages 01 – 19, the model-measurement agreement is well within 10 %, giving us high confidence in the overall constraints (including the precision of the measured light amplitudes, O<sub>3</sub>, and SO<sub>2</sub>). This leaves only a single scaling factor common to all light sources to accurately constrain  $j_{\text{O}(1\text{D})}$ .

The less precise agreement after stage 19 (but still for the most part within 20 %) is at lower H<sub>2</sub>SO<sub>4</sub> with more complicated stages; stage 20 is a cleaning stage with the 385 nm LEDs (LS1) illuminated and concurrent wall loss of SO<sub>2</sub> and O<sub>3</sub> as well as non-trivial condensation, stages 21-23 include very low excimer intensity with noisy amplitudes despite the median

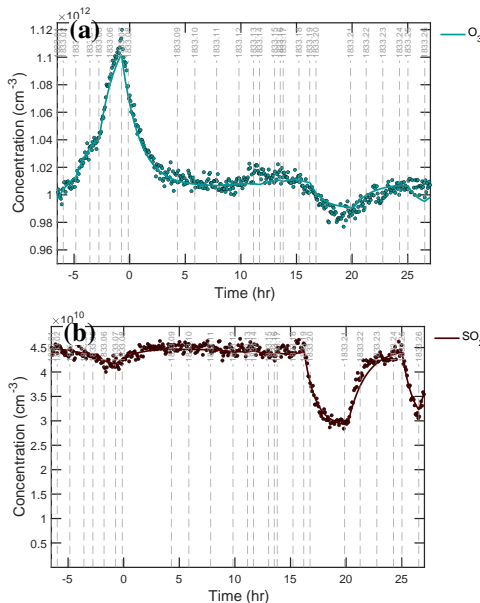


**Figure 13.** Simulated (curve) and observed (points) gas-phase precursors with smoothed and interpolated measurements. (a)  $\text{O}_3$ . (b)  $\text{SO}_2$ . Note the different, linear  $y$ -axis scales. Observed values have been smoothed with a median filter and interpolated to model time points as needed. Production of  $\text{O}_3$  via  $\text{O}_2$  photolysis during the Hg–Xe (UVH) stages is evident, as is a stoichiometric (1:1) decrease in both  $\text{O}_3$  and  $\text{SO}_2$  especially with 380 nm LED (LS1) illumination but also with UVH illumination.

685 smoothing, and stage 25 again has declining  $\text{SO}_2$  and significant excimer contributions. As there is little model-measurement bias, the 20 % deviations are attributable to noise. Because the  $\text{H}_2\text{SO}_4$  is the only significant connection between the gas-phase photochemistry and the particle microphysics, the very high fidelity of this model-measurement agreement (after  $\text{H}_2\text{SO}_4$  calibration) effectively decouples the microphysical and photochemical models, though the photochemistry (because of the  $\text{H}_2\text{SO}_4$  condensation loss) remains dependent on accurate constraints from the microphysics.

690 There is no evidence for “hidden sulfuric acid”; there is nowhere to hide. The precise agreement between simulated and observed  $\text{H}_2\text{SO}_4$  over at least a factor of 10 as light intensities change confirms this. A primary indicator for unobserved  $\text{H}_2\text{SO}_4$  contained in small clusters of  $(\text{NH}_4 \cdot \text{HSO}_4)$  would be nonlinear observed  $\text{H}_2\text{SO}_4$  with increasing absolute  $\text{H}_2\text{SO}_4$ , as the clusters concentrations are at least quadratic in  $\text{H}_2\text{SO}_4$  (Rondo et al., 2016). The relatively low nucleation rate coefficients, far below the kinetic limit, also confirm that small clusters are an inconsequential reservoir of  $\text{H}_2\text{SO}_4$ . Small clusters sequester 695 a substantial pool of  $\text{H}_2\text{SO}_4$  when nucleation is near the kinetic limit, such as with the  $\text{H}_2\text{SO}_4 + (\text{CH}_3)_2\text{NH}$  system (Lehtipalo et al., 2016), but not here.

In addition to the principal photolysis of  $\text{O}_3 \xrightarrow{\text{h}\nu} \text{O}(\text{1D}) + \text{O}_2$ , the effects of two other photolysis processes are evident in Fig. 13. The Hg–Xe lights produce sufficient fluence for  $\lambda < 250$  nm to drive weak photolysis of molecular oxygen,  $\text{O}_2 \xrightarrow{\text{h}\nu} 2\text{O}(\text{3P})$ , but also there is clear evidence that especially the 385 nm LED (on at full intensity in stages 19–20 and again in stage 700 25) drives what appears to be stoichiometric (1:1) loss of  $\text{SO}_2$  and  $\text{O}_3$ . The  $\text{SO}_2$  reaches a new, steady state level roughly 1/3 lower than its initial value, which under dark conditions is governed by the flow in and the chamber ventilation timescale



(1.7 h). We conclude that this loss is a photon mediated reactive wall uptake of  $\text{SO}_2 + \text{O}_3$ , with at least the sulfur containing reaction products (presumably  $\text{SO}_4$ ) remaining on the wall. It is possible that the  $\text{H}_2\text{SO}_4$  observed during stage 20 indicates small evaporation of  $\text{H}_2\text{SO}_4$  from this (copious) wall source, but it is also possible that there is sufficient overlap between the 705 high-frequency tail of the light source and  $\text{O}_3$  absorption to produce some  $\text{OH}$ ; separating these possibilities would require direct  $\text{HO}_x$  measurement. However, this source is a factor of 10-100 weaker than the targeted UV sources (UVH and UVX) even with the high 385 nm LED intensity. Consequently, we conclude that it is insignificant to the overall calibration.

Comparing Figs 12 and 13 with Figs 2 and 4, the importance of smoothing via median filtering (and excluding UVX crosstalk from the UVH amplitudes) is also clear. Many of the finer features in the model values are impossible to see in the unfiltered 710 raw data. Even with the increased precision of the smoothing, a model for dry growth is equally precise, with twice the  $\text{H}_2\text{SO}_4$ ; this agreement does not differentiate between the dry growth and wet growth scenarios (changing the  $\text{H}_2\text{SO}_4$  calibration simply shifts the  $y$ -axis scale). This is because the  $\text{HO}_x$  chemistry (production and loss) is nearly linear over the conditions of this run, with the  $\text{OH} + \text{HO}_2$  reaction reaching at most 10 % of the overall  $\text{OH}$  loss in Fig. 12b.

## 9 Charge and ion production and loss

715 Close examination of the CPC<sub>2.5</sub> data in Fig. 6 shows the effect of voltage transitions in the clearing field removing charged particles – for example the particle number drops by roughly 20 % at the start of stage 05 (a neutral nucleation state at full UVH power) and by less than 10 % at the start of stage 02 (also a neutral nucleation stage, at 20 % UVH power). This indicates that only a small fraction of the particles in stage 01 were charged by the end of the stage, even though this is an ion induced 720 nucleation (charged) stage with evidently much more particle formation than the subsequent neutral stage. The same applies at the end of the gcr stage 04 less than 20 % of the particles were charged (though notably more than after stage 01). That is confirmed by Fig. 3. The sectional particle microphysics model presented so far neglects charge, and thus we have so far left out of our model-measurement constraints are the primary ions and charged particles. These, especially the primary ions, are much closer in size and collision dynamics to the gas-phase than the particle microphysics, and so we incorporate them into 725 our gas-phase photochemical model, with primary ion production as well as loss via wall deposition (including the clearing field), ion recombination, and diffusion charging (and neutralization) of larger particles.

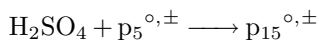
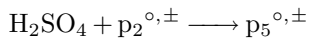
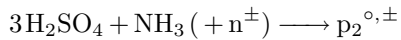
### 9.1 Modal scheme

To simulate the loss of primary ions we need some treatment of the number and charge state of larger particles (the overall condensation sink), so we simulate nucleation and growth in the gas-phase model with a succession of pseudo-reactions in a simplified modal representation of particles with nominal diameters  $d_p = 2 \text{ nm}, 5 \text{ nm},$  and  $15 \text{ nm}$ , and charge  $q = -1, 0, +1$ , 730 labeled  $p_{d_p}^q$ . Along with the primary ions, we refer to the 2 nm mode as clusters, the 5 nm mode as the nucleation mode, and the 15 nm mode as the Aitken mode. Nucleation is formation of the 2 nm cluster mode (in any charge state) and we assume that growth to the 5 nm mode is required for detection in the CPC<sub>2.5</sub>. The scheme is designed to be accurate for ions and the nucleation rates, and “reasonable” for the larger particles. This is not a formal modal scheme with mode widths or any

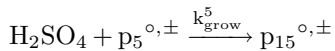
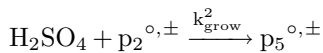


representation of composition, just charge. Our objective here is to use this portion of the model to identify the major processes  
735 controlling the charged microphysics and charge balance in the experiment.

As always the scheme starts with nucleation to form 2 nm clusters, followed by condensational growth from mode to mode.



740 The nucleation coefficients are identical to those in the microphysical model, but the ions are treated explicitly. We model growth as first-order and rate-limited by  $\text{H}_2\text{SO}_4$  with a rate coefficient to drive growth from one mode to the next.

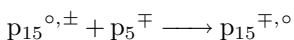
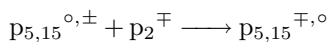
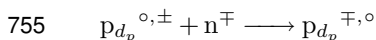


However, it takes several hundred  $\text{H}_2\text{SO}_4$  collisions to grow from 2 nm to 5 nm to 15 nm. That number for each case is  
745  $g_{\text{H}_2\text{SO}_4}^{d_p} \gtrsim 100$ , and so the effective modal growth coefficient is

$$k_{\text{grow}}^{d_p} = k^{d_p} / g_{\text{H}_2\text{SO}_4}^{d_p} < 10^{-12} \text{ cm}^{-3} \text{ s}^{-1}$$

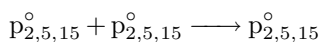
where  $k^{d_p}$  is the collision kernel for single collisions of  $\text{H}_2\text{SO}_4$  with particles of size  $d_p$ . The rate coefficient includes the growth  
enhancements by co-condensation of  $\text{NH}_3$  and hygroscopic growth if appropriate. The apparent loss of  $\text{H}_2\text{SO}_4$  from this modal  
750 growth is trivial compared with the (observationally constrained) condensation sink term of  $\text{H}_2\text{SO}_4$  itself; that is a significant  
advantage as it effectively decouples the  $\text{H}_2\text{SO}_4$  loss from the particle formation and growth in the mechanism, allowing us to  
continue to constrain  $\text{H}_2\text{SO}_4$  loss by the observed condensation sink while simultaneously modeling the nucleation and growth  
via this modal mechanism.

Importantly, we also represent diffusion charging. At these particle sizes, essentially no particles are doubly charged, but  
charging and neutralization are important.



The charging occurs via collisions of the primary ions themselves ( $\text{n}^\pm$ ) but also via collisions involving any charged particles  
smaller than a given target particle (i.e. all collisions involving charge of 15 nm particles with any primary ions, 2 nm, or 5 nm  
760 particles). In this simplified modal mechanism, particle charging does not cause growth, and so it removes the smaller charge  
carrying particle (this is an important coagulation mechanism (Mahfouz and Donahue, 2021)).

Coagulation also occurs via neutral collisions between particles of all sizes, which again does not cause growth in our  
(overly) simple scheme:



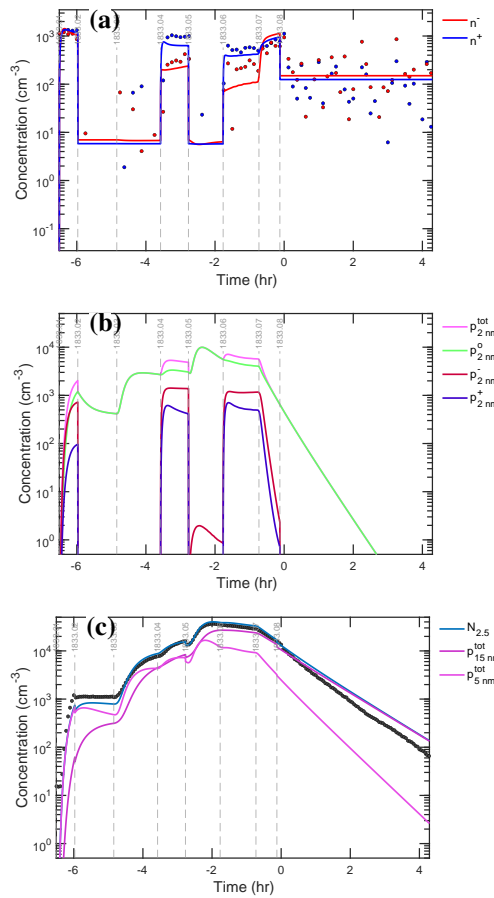


**Figure 14.** Simulation of particle evolution (including charge state) during the UVH stages using a modal scheme with primary ions and modes centered at 2 nm, 5 nm, and 15 nm along with relevant observations. (a) Simulated and observed primary ions. (b) Simulated concentration of the 2 nm mode, representing clusters of each charge state. (c) Simulated and observed  $N_5$  (the sum of 5 nm and 15 nm particles). The primary ion simulation reproduces the observed depletion of primary ions, strongly biased toward negatively charged ions. The 2 nm clusters are principally neutral even during stages that are dominated by ion induced nucleation, such as stage 01, because the charged clusters are steadily neutralized by ion-ion recombination on a timescale of around 10 min. Finally, the simulated  $N_5$  trace reasonably reproduces the CPC<sub>2.5</sub> observations (shown in gray), with similar fidelity to the microphysical model. Notably, the simulation reproduces the dips in particle numbers at the beginning of neutral stages immediately following charged stages, such as stage 05, when the charged particles are rapidly swept from the chamber as well as the loss rate of the largest particles during the cleaning stage (08) where charging and electrostatic removal enhances that loss.

765 Analysis of growth rates in the microphysical model below shows that, for the conditions of this experiment, condensational growth far exceeds coagulational growth and so these assumptions are warranted.

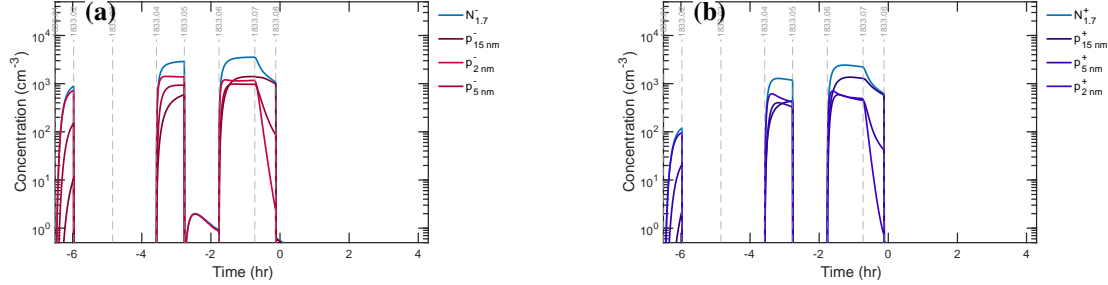


**Figure 15.** Simulated charged particles vs time, with concentrations of each mode (centered at 2 nm, 5 nm, and 15 nm) as well as the sum,  $N_{1.7}^{\pm}$ . (a) Negatively charged particles. (b) Positively charged particles. As with observations, during strong ion-induced nucleation stages (i.e. 06) there are  $2-3 \times 10^3 \text{ cm}^{-3}$  of both negatively and positively charged particles. Strong ion-induced nucleation yields slightly fewer positively charged than negatively charged particles, whereas weak ion-induced nucleation (i.e. stage 01) favors negatively charged particles by nearly an order of magnitude.

## 9.2 Model results

The gas-phase modal scheme as part of the photochemical model is substantially faster than the full sectional microphysical model (and would be vastly faster than a full sectional microphysical model treating charge). We show the results in Figs 14 and 15. Fig. 14 shows the modeled and measured primary ions, the 2 nm cluster mode for each charge state along with the total, and the total particles in the 5 nm nucleation and 15 nm Aitken modes along with the sum of these two modes (nominally  $N_5$ ) and the observed CPC<sub>2,5</sub> count. Fig. 15 shows the concentration in each mode for negatively and positively charged particles along with the total of all the modes (nominally  $N_2^{\pm}$ ). As with the microphysical model, and despite its simplifications, this modal simulation reproduces the observations with good fidelity.

For the primary ions in Fig. 14a we subtracted an empirical background value of  $200 \text{ cm}^{-3}$  from each polarity since these represent the AIS instrument background signal for our operating conditions. With the AIS offset correction, the simulated ion concentrations match the observations reasonably well. The particle-free steady state near  $1500 \text{ cm}^{-3}$  confirms an ion-pair production rate of  $7 \text{ cm}^{-3} \text{ s}^{-1}$  (combining galactic cosmic rays with stray muons from the CERN Proton Synchrotron and external targets). The primary ions rarely reach  $1500 \text{ cm}^{-3}$  – only the weakest charged nucleation stages, such as stage 01, are free of ion depletion for either polarity. The ion depletion and the charge asymmetry are captured during strong ion-induced nucleation stages (04, 06). A simulation without a 10 % contribution from the positive ion channel does not reproduce the cation depletion.

Fig. 14b shows that the neutral 2 nm particles comprise more than half of the total 2 nm mode at all times; the green neutral concentration is always either coincident with the magenta total or 10-20 % below it. During stage 01 the nucleation is more than 90 % ion induced, and even during that stage, the 2 nm clusters are mostly neutral, with a strong asymmetry between the negatively and positively charged particles. However, without the 10 % positively charged nucleation channel, the positively charged particle concentration during stage 01 would be far too low compared to Fig. 3; the observed asymmetry during that



stage is a telling indicator of the relative intensity of the two polarities. Evidently, neutralization of the 2 nm negatively charged particles by positively charged primary ions, or positively charged clusters, is substantial.

790 Fig. 14c shows the totals of the 5 nm nucleation and 15 nm Aitken modes and their sum (nominally  $N_5$ ), along with the observed CPC<sub>2.5</sub> signal. Because this simulation has modes at 2 and 5 nm, comparison with the CPC<sub>2.5</sub> signal ( $d_p = 2.2$  nm) is imprecise. However, except for weak nucleation periods with substantial 2 nm particle concentrations, the sum of the two larger (nucleation and Aitken) modes from the simulation agrees with the observations to within 10 %. Notably, the simulation quantitatively reproduces the concentration dips when stages switch from charged to neutral (i.e. the clearing field is turned on, 795 at the start of stage 05) and any charged particles are removed quickly.

Fig. 15 shows that the concentrations of the three modes are almost always in rank order for the negatively charged particles during gcr stages. These are all represented with a crimson hue, with brighter colors corresponding to smaller modes. The smaller negatively charged particles are always more abundant, and the larger modes react to the onset of ion induced nucleation much more slowly than the smallest particles (e.g. stage 10). This is opposite to the thermodynamics of charging but consistent 800 with nucleation and growth, with some losses. Below 10-15 nm, the principal reason the negatively charged particles exist is because they grew up from smaller negatively charged particles. During the wall loss stage, 07, the reverse is true; the source is removed and the smaller particles are lost before the less diffusive larger particles.

805 The positively charged particles present a more nuanced picture. At times, such as during stage 06, the larger positively charged particles are more abundant than the smaller modes, suggesting that diffusion charging and not nucleation and growth is the major source. This diffusion charging also depletes the smaller positively charged particles and so deprives the positively charged nucleation channel of its source. Overall, there is a direct relationship between the relative abundance of small charged particles below 10 nm diameter, compared to the neutral abundance, and the importance of ion induced nucleation of that polarity.

810 Treating the nucleation and growth with this modal simulation, along with the charge production and loss, ultimately yields a good simulation of the total primary ion behavior, including the asymmetry between positively and negatively charged ions, clusters and particles. Finally, the particle loss rates during the cleaning stage are adequately reproduced. Overall this thus yields the final element of closure when combined with the (sectional but uncharged) microphysical model and the gas-phase photochemistry.

## 10 Process rates

815 A crucial element of both the microphysical and photochemical models is that they disaggregate and diagnose process rates. This is vital to understanding the results but also to experimental design – experiments are often designed to constrain or test a specific process, and the results of a given test are only meaningful if that process is actually prominent, making the observations sensitive to the process. Nonlinear interconnected systems such as this can be subtle – stiff systems almost by definition are sensitive to seemingly minor terms – but careful rate analysis is if anything more important in that case.

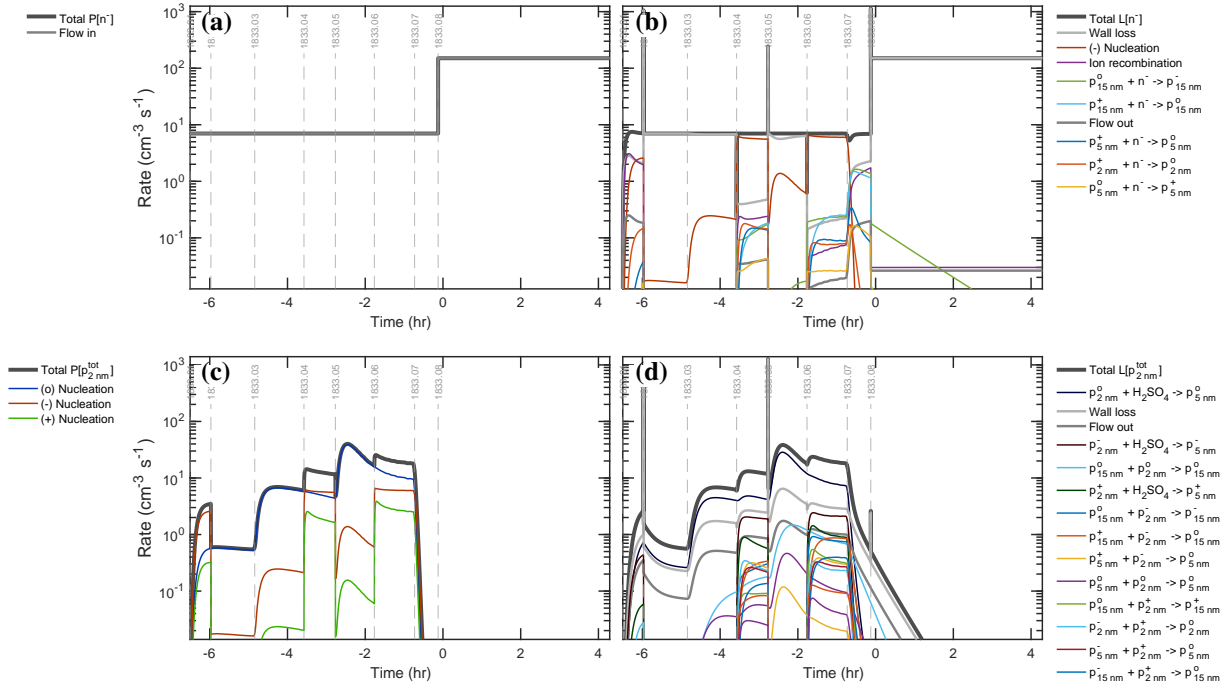


**Figure 16.** Production ( $P[x]$ ) vs loss ( $L[x]$ ) for primary negative ions and the total 2 nm cluster mode from the gas-phase model. Both show production rates on the left and loss rates on the right, with identical scales to permit assessment of the rate balance. Transitions from charged to neutral stages (e.g. the beginning of stages 02 and 05) cause a short, sharp increase in loss as the clearing field rapidly removes charged particles and the rate balance is re-established in seconds. (a) Production and (b) Loss of negatively charged primary ions. Production is steady at  $7 \text{ cm}^{-3} \text{ s}^{-1}$  gcr ion-pair formation aside from enhanced formation of  $150 \text{ cm}^{-3} \text{ s}^{-1}$  via the CERN beam during the cleaning stage 08; this is modeled as a homogeneous flow and is labeled “Flow in”. Loss has many competing elements, including wall loss, ion induced nucleation, recombination with positively charged ions (and larger particles), and diffusion charging of larger neutral particles. Loss by nucleation saturates during gcr nucleation stages 04 and 06, where the red nucleation rate dominates the loss term. (c) Production and (d) Loss of total clusters (all charge states comprising the 2 nm particle mode). Production is nucleation, separating neutral (o), negatively (–) and positively (+) charged clusters. Loss includes wall deposition but is predominantly growth to the larger (5 nm) mode. Numerous processes involving ions and charged particles of opposite polarity contribute during gcr stages (04 and 06).

820 For the current system, both the microphysical and photochemical rates are important diagnostics. We have already presented several rate analyses in the process of showing the key model results.

### 10.1 Photochemical rates

In order to assess the  $\text{H}_2\text{SO}_4$  loss we have already presented its production and loss rates during the UVH stages in Fig. 7, side by side with identical  $y$ -axis ranges. The plots include individual rate terms as well as totals. This format facilitates a quick



825 assessment of the overall rate balance. The overall production increases sharply for the three UVH settings, while the loss rate catches up to the production rate asymptotically on a timescale that is evidently a small fraction of an hour. The same applies during the wall loss and cleaning stages (07 and 08), when the photochemical production drops quickly past the (unknown) chamber source, which is modeled as a steady flux of  $280 \text{ cm}^{-3} \text{ s}^{-1}$ . After the induction period in each stage, production and loss clearly balance to give a steady state; however, the growing condensation sink clearly plays a role as it grows to compete  
830 with the wall loss term, even driving the small “undershoot” in the  $\text{H}_2\text{SO}_4$  during the early part of the cleaning stage (08). It is also clear that photochemical production balances wall and condensation losses, with all other terms playing a minor role (though ventilation is important at the 10 % level).

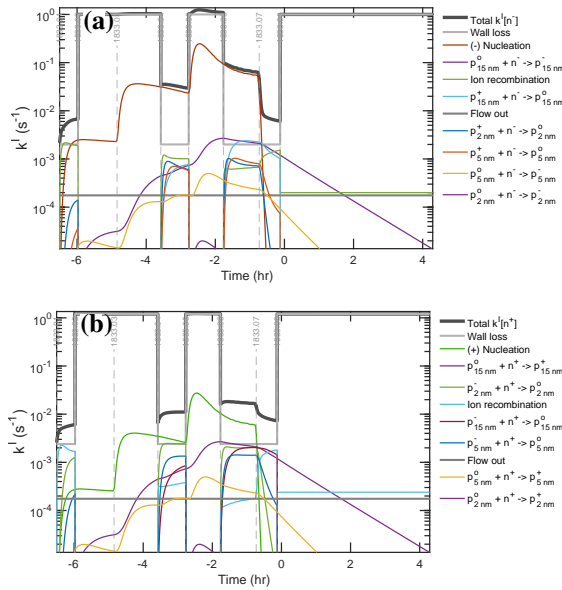
Fig. 8 shows the complementary assessment of the  $\text{H}_2\text{SO}_4$  first-order loss during the UVH stages. This is a separate and equally important diagnostic. Here the emerging importance of condensation between stage 04 and the start of stage 08 is  
835 made clear, but also the quantitative lifetime of 500 s or less confirms the rapid but discernible approach to steady state of both  $c_{\text{H}_2\text{SO}_4}$  and  $L_{\text{H}_2\text{SO}_4}$ .

Fig. 12 also shows the contributions to the OH first-order loss, which in total is slightly slower than  $1 \text{ s}^{-1}$ . The largest sink is  $\text{CO}$ , followed by  $\text{O}_3$ , with  $\text{SO}_2$  contributing at less than 10 %. All of these are fairly constant, though the dips in especially  
840  $\text{SO}_2$  are evident. Nonlinear processes such as  $\text{HO}_2 + \text{OH}$  play a very modest role of at most a few percent. The limited role of  $\text{SO}_2$  and especially the limited non-linear  $\text{HO}_x$  loss reactions are the main reason why the gas-phase photochemistry is almost insensitive to the absolute  $\text{H}_2\text{SO}_4$  calibration beyond simply shifting the (log)  $y$ -axes. Doubling the  $\text{H}_2\text{SO}_4$  requires doubling the OH which requires doubling the light intensity; beyond that, the shapes of the concentration profiles are nearly identical.

## 10.2 Charged modal microphysics

Interpretation of the  $\text{H}_2\text{SO}_4$  rate and lifetime plots is relatively straightforward. Other important processes are more nuanced.  
845 Fig. 16a shows the production and Fig. 16b the loss rates for negative primary ions ( $n^-$ ). The ions are almost always in steady state, and so the total production and loss balance; however, the very brief transients are evident at the start of neutral stages when the clearing field turns on suddenly and the loss rates show a brief spike. For stages 04 and 06, ion-induced nucleation is the predominant loss for the primary negatively charged ions and so the crimson “(-) nucleation” curve nearly reaches the total loss; this represents the saturated ion formation limit, but also means that the primary ions have all grown and are thus  
850 depleted. This in turn affects the particle charging dynamics and so particle losses. Even during stage 01, nucleation becomes competitive with ion recombination (“cluster neutralization”) and wall losses, which in turn are all nearly equal during the stage; this is the most complicated condition, where the three major loss mechanisms – recombination, wall loss (deposition) and nucleation – are all competitive and nearly equal.

An analysis of the primary ion first-order loss rates is also revealing, as shown in Fig. 17. The ion lifetimes are under 100 s,  
855 revealing why they are in steady state. The most notable feature is the modulation of the wall loss as the clearing field turns on and off, with the primary ion lifetimes dropping to 1 s when the clearing field is on. In contrast, nucleation depends only on (the third power of)  $c_{\text{H}_2\text{SO}_4}$  and so becomes prominent during the medium and high intensity UVH stages. For the negative ions, these are the only notable sinks. For the weaker positive channel, nucleation never overwhelms other processes, and during



**Figure 17.** Simulated first-order loss during the UVH stages for (a) negatively charged and (b) positively charged primary ions. At the beginning of stage 01, without substantial nucleation or diffusion charging, ion recombination is (by chance) equal to wall loss. High-voltage clearing stages (02, 03, 05, 08) increase the wall-loss to  $1 \text{ s}^{-1}$ . Both nucleation and a large condensation sink causing diffusion charging and neutralization increase the loss. Saturation of ion-induced nucleation (e.g. negatively charged ions during stage 04 and 06) is indicated by nucleation dominating the loss. At steady state (e.g. nearly in stage 04) diffusion charging and neutralization nearly balance, as required.

stage 06 a host of neutralization channels are important secondary sinks. This plays a key role in the overall mechanism, as  
860 neutralization of the more intense negative ion induced nucleation pathway causes neutral particles to dominate the overall distribution, as we observe. However, the results suggest that for somewhat higher  $\text{H}_2\text{SO}_4$ , the positive nucleation would also saturate; this would have a secondary effect of reducing the neutralization rate by completely depleting the primary ions of both polarities.

Nucleation produces the 2 nm cluster mode, and Fig. 16c shows production and Fig. 16d loss of the total 2 nm cluster mode  
865 mode in all charge states (neutral, negatively charged, and positively charged;  $n_2 = n_2^+ + n_2^- + n_2^0$ ). The total rates are more rounded compared to the square-wave shape of the primary ion rates, but there are more contributions to both production and loss. The sources of this family comprise each of the three nucleation rates (neutral, negatively charged and positively charged). The sinks include wall loss and dilution (“flow out”), growth by condensation of all three charge states (“cluster growth”), and also various forms of coagulation.

870 For the nucleation source, during stage 01 this is almost entirely (negatively charged) ion-induced nucleation, but, for higher  $\text{CH}_2\text{SO}_4$ , the charge saturates at the ion-pair formation rate of  $7 \text{ cm}^{-3} \text{ s}^{-1}$  and adds only incrementally to the total. During stage 06,  $\text{H}_2\text{SO}_4$  is high enough that even the weaker positive nucleation reaches half of the positive ion production rate, but it does not quite saturate. This shows one important element of constraining both polarities of ion induced nucleation – even though

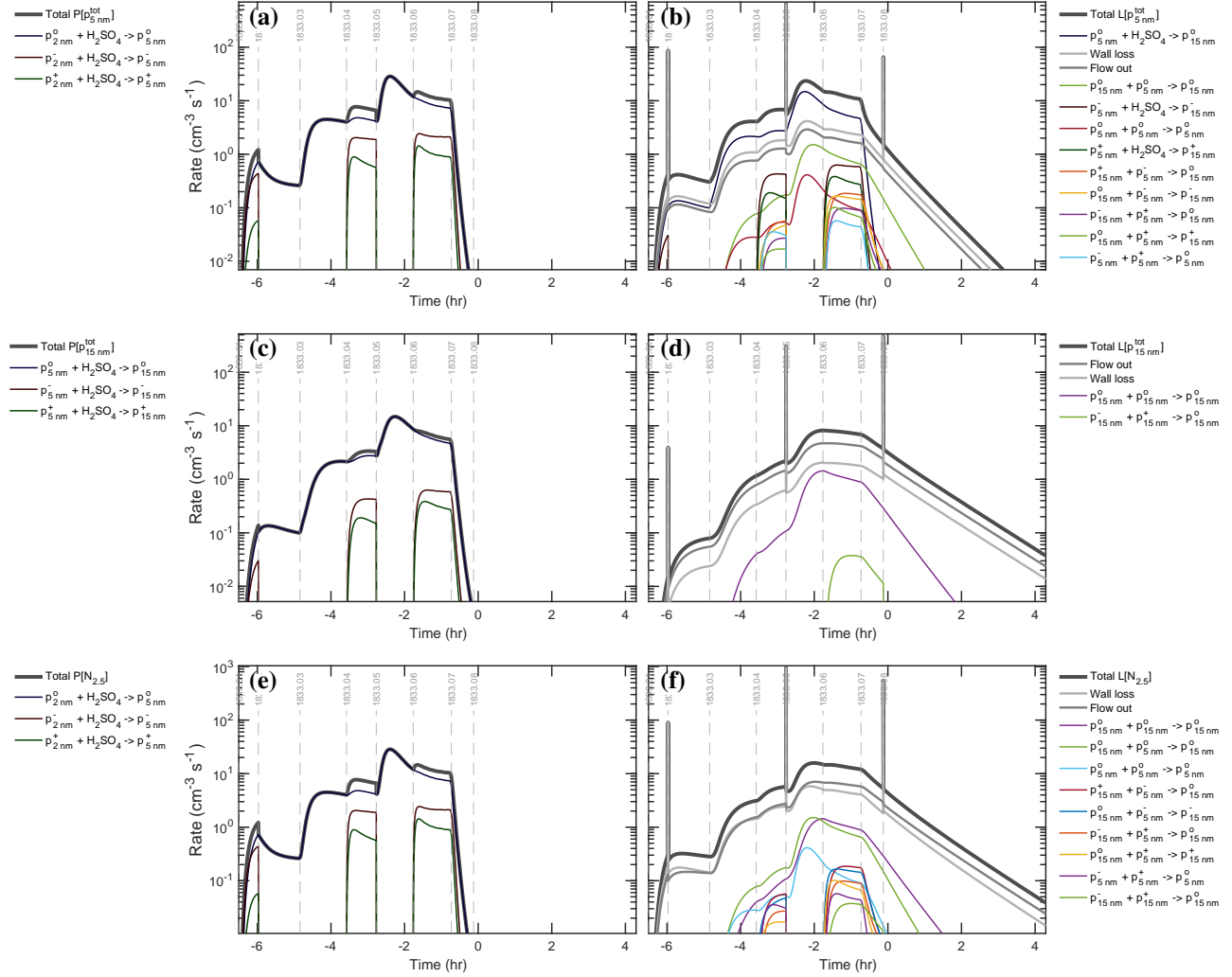


**Figure 18.** Production and loss of particle modes in the gas-phase model. (a) Production and (b) Loss of total 5 nm particles. Production is largely via neutral condensational growth from the 2 nm mode. Loss includes growth to 15 nm but also wall loss and ventilation loss, as well as coagulation between 5 and 15 nm modes during high-concentration stages 05 and 06. (c) Production and (d) Loss of total 15 nm particles. Production is almost exclusively neutral growth from the 5 nm mode. Loss includes ventilation and wall deposition with a 10 % contribution by coagulation during high concentration stages. (e) Production and (f) Loss of combined 5 and 15 nm particles (“ $\mathcal{N}_5$ ”). Production is identical to the 5 nm production. Loss is split equally between wall deposition and ventilation, with three coagulation pathways between the two modes contributing during the high-concentration stages.

the positive channel is roughly 10 % as efficient as the negative channel, it remains important near the ion pair saturation limit



875 and this has knock on effects on particle charging and neutralization, as we shall see. Once the ion induced channels saturate, the neutral pathway (blue) predominates even during the gcr stages, such as stage 06.

The loss terms are marginally more involved. Neutral condensational growth to 5 nm (dark blue) is almost always the leading sink of the 2 nm particles (meaning the particle survival probability is high), though wall loss is more important at lower  $H_2SO_4$  when growth is slower. The spikes in wall loss at the start of stages 02 and 04 drive the small dips in the overall 880 number discussed above. During the gcr stages, growth of negatively charged particles (dark crimson) plays a secondary role, and ventilation is consistently about 10 % of the total loss. A host of other processes are minor sinks, especially during the gcr stages when the small clusters can diffusion charge larger (neutral) particles but also be lost via coagulation to larger positively charged particles.

Fig. 18 shows the production and loss terms for total particles (the sum of all charge states) for the larger particle modes at 5 885 nm (“nano”) and 15 nm (“Aitken”) as well as the total of those larger particles, which is identified by the family name “ $N_{2.5}$ ”. The only source for these total mode families, within the scheme defined in the quasi-modal mechanism, is condensational growth.

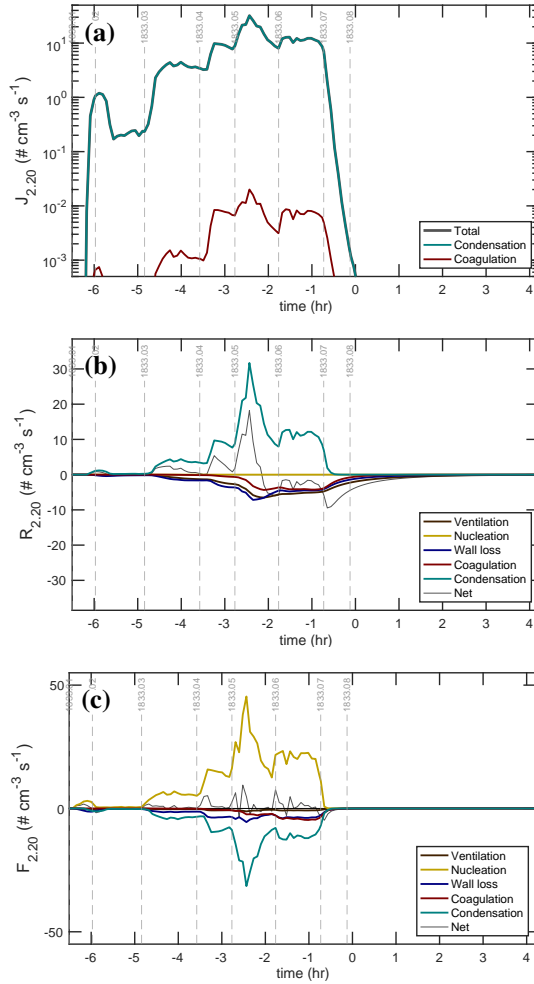
Consequently, in Fig. 18a the production of nucleation-mode nano particles ( $p_5$ ) is growth from the cluster mode ( $p_2$ ), in 890 each of the three charge states. Even at this size, neutral growth is always predominant even during gcr stages. Fig. 18c shows that growth from  $p_5$  to  $p_{15}$  is qualitatively the same but the neutral pathway is almost completely dominant. As is typical, losses are more nuanced. In Fig. 18b for the 5 nm mode, growth to 15 nm, wall loss, and dilution (flow out) are all competitive, with growth becoming progressively more significant at high  $H_2SO_4$  as expected. However, for the highest intensity UVH with high 895  $H_2SO_4$  (stages 05 and 06), neutral coagulation loss of 5 nm nanoparticles to 15 nm Aitken mode particles comprises roughly 10 % of the overall nanoparticle loss rate. In Fig. 18d for the 15 nm mode, our simple scheme does not treat further growth, and flow out of the chamber takes over as the largest sink. However, neutral coagulation between 15 nm particles is also a 10 % sink.

Fig. 18e shows production and Fig. 18f shows loss for the combination of the two modes ( $N_{2.5}$ ). The production rates are 900 identical to production for  $p_5$  in Fig. 18a. However, nanoparticle growth from  $p_5$  to  $p_{15}$  is no longer a sink and coagulation between the two modes and coagulation among the 15 nm particles are roughly equivalent sinks, accounting for roughly 20 % of the total particle loss. Wall and ventilation losses are also roughly equal at 40 % each.

### 10.3 Microphysical process rates

The model with sectional microphysics permits more detailed simulation (and analysis) of the size-dependent microphysical processes, but it is not (yet) coupled to the gas-model and does not (yet) include charge. Consequently, it is driven by either 905 observed or modeled vapor concentrations that drive nucleation and growth. As a reminder, this model uses (spherical equivalent) diameter,  $d_p$ , whereas instruments generally report mobility diameter,  $d_{mob} \simeq d_p + 0.3$  nm (Larriba et al., 2011), so for example a 2.5 nm CPC has a physical cutoff diameter of  $d_p = 2.2$  nm.

Fig. 19 shows the particle-phase rates at  $d_p = 2.2$  nm. Fig. 19a shows  $J_{2.2}$ , which is the flux of particles across the 2.2 nm size cut in the sectional model. This includes both condensational growth as well as coagulation, but condensation constitutes



**Figure 19.** Rates in the sectional microphysical model at  $d_p = 2.2 \text{ nm}$  ( $d_{\text{mob}} \simeq 2.5 \text{ nm}$ ). (a) Formation rate,  $J_{2,2}$ , defined as the flux of particles from  $d_p \leq 2.2 \text{ nm}$  to  $d_p > 2.2 \text{ nm}$ . This is almost entirely due to condensation, but some coagulation contributes. (b) Integrated rates for all processes for  $d_p \geq 2.2 \text{ nm}$ . Condensation is the source (matching panel a) as particles nucleate at  $d_p = 0.8 \text{ nm}$  and grow into the  $N_{2,2}$  range, whereas losses are distributed more or less evenly among wall loss, ventilation (dilution), and coagulation. These are the critical loss terms needed to calculate  $J_{2,2}$  from a counter with a 2.2 nm size threshold (e.g. CPC<sub>2,5</sub>) during steady state conditions (e.g. much of stage 06). The system is often not in steady state (the dashed net rate is not always zero). (c) Integrated rates for all processes for  $d_p < 2.2 \text{ nm}$ ; coagulation, wall loss and ventilation constitute corrections to  $J_{2,2}$  for losses below that size; the gold nucleation source has a larger amplitude than the condensation growth out of (and thus a sink from) this size range.

the overwhelming majority of the flux; for growth involving “hidden” sulfuric acid clusters, the coagulation term would be  
910 much larger, as that is technically coagulation. An interesting feature is the drop in  $J_{2,2}$  well after the end of stage 01, when



the system switched from gcr to neutral conditions; this reflects the time delay due to growth between formation near 1 nm and appearance at 2.2 nm. This is similar to the slow drop of  $p_5$  production in Fig. 18a.

Fig. 19b shows the integrated rates above the cutoff size of  $d_p = 2.2$  nm (processes that would affect a CPC<sub>2.5</sub>) and Fig. 19c shows the integrated rates *below* that cutoff size (processes that would affect the difference between the nucleation rate itself, 915  $J$ , and the flux into the CPC<sub>2.5</sub> measurement range,  $J_{2.2}$ ). The  $y$ -axis is linear and symmetrical about 0. These are the rates into or out of the total population larger than 2.2 nm (i.e.  $N_{2.2}$ ) in Fig. 19b and the rates for all processes before reaching that cutoff size in Fig. 19c. For that reason, condensation (teal) is the only major source of  $N_{2.2}$  as smaller particles grow past the 920 cutoff diameter, but the three losses of coagulation (red), wall loss (blue) and ventilation (brown) are all similar in magnitude. Note that growth via aggregation of “hidden” sulfuric acid clusters would formally appear as a coagulation source in Fig. 19a and a coagulation sink in Fig. 19c, as it would remove (two) extremely small particles but produce (one) larger particle above the CPC<sub>2.5</sub> cutoff. The net rate in Fig. 19b is rarely near 0 for the fluxes above 2.2 nm, other than during stage 06, and so even for the small 2.2 nm particles the system almost never reached a steady state. This is because for much of the run there were abundant particles between 10 and 30 nm, and the loss timescales (and thus the timescale to establish a steady state) were almost as long as the dilution timescale of over an hour.

925 Fig. 19b also illustrates the method used at CLOUD to measure nucleation rates. Specifically, the figure illustrates the process used to determine  $J_{2.2}$ ; it is not to measure  $dN_{2.2}/dt$  (equivalent to the net rate) and then apply small corrections, but rather to constrain the steady state balance of loss via wall deposition, dilution flow out, and coagulation and then to apply a small correction for any observed  $dN_{2.2}/dt$  when the system is not fully at steady state (Dada et al., 2020). As seen here, the three loss terms are often similar, though coagulation is often the smallest of the three.

930 In contrast, Fig. 19c shows process rates below 2.2 nm. Here, nucleation (gold) is the only source and this is for the most part balanced by condensational growth out of the smaller range. The nucleation source drops immediately at the end of stage 01 here, without delay. The condensation term is exactly the opposite of the condensation flux into the  $N_{2.2}$  population from the middle panel. In this case the other sinks – coagulation and wall loss – are secondary but by no means negligible, and the system reaches a steady state quickly because the lifetime for particles smaller than 2.2 nm remains short at all times. The (gold) 935 nucleation rate is directly comparable to the  $p_2$  production rate in Fig. 19. These agree well, though the nucleation rates in the microphysical model and Fig. 19 are driven by interpolated H<sub>2</sub>SO<sub>4</sub> observations whereas the photochemical nucleation rates are driven by (smoother) modeled H<sub>2</sub>SO<sub>4</sub>, and the third-order dependence amplifies the modest noise in the interpolated data. However, the good agreement also confirms that the ion production saturation limit in the microphysical model is sufficiently accurate.

## 940 11 Uncertainties

Uncertainties in this analysis rest on the accuracy of CPC<sub>2.5</sub> data and the precision of the H<sub>2</sub>SO<sub>4</sub> measurements, and how all instrument measurements reflect the actual state of the CLOUD chamber (i.e. line loss corrections and chamber mixing). As the analysis shows, most of the particles measured by the CPC are neutral and larger than 10 nm during the periods when the



constraints are strong. The CPC and SMPS agree to within 33 % during these periods and we elect to base our analysis on the  
945 more robust CPC measurement. The precise  $\text{H}_2\text{SO}_4$  behavior, including timescales and level-signal changes when condensation competes with wall losses is also strong and agrees with *a priori* determination of the condensation sink. We therefore also regard the condensation sink constraint as robust and accurate.

While the number and condensation sink of the particles is accurately constrained, their composition is not certain – notably the water content. At 58 % RH, deliquesced  $(\text{NH}_4)_2\text{SO}_4$  particles with an  $\text{H}_2\text{O}$  activity of 0.58 have a (size dependent) diameter  
950 growth factor compared to dry (effloresced)  $(\text{NH}_4)_2\text{SO}_4$  of roughly 1.2 (Lei et al., 2020) and very nearly double the growth rate versus dry particles. If the thermodynamics for fully neutralized ammonium sulfate did prevail under these conditions, it would be unlikely for the growing particles to be aqueous; however, we cannot exclude deliquescence of ammonium bisulfate during the process of nucleation that would then never effloresce. In fact, the preponderance of the evidence supports the particles remaining deliquesced and wet.

955 A related uncertainty is the concordance of our particle size measurements with the actual size in the CLOUD chamber. In our analysis we assume that the SMPS measurements reflect the actual particle size, and the SMPS sheath air is filtered air that remains near the chamber RH. Thus, if the the actual particles in CLOUD were wet and larger, given the strong constraints on the actual condensation sink, the “free” parameter would be the Hamaker constant, which would decrease to compensate. A somewhat lower  $A_{\text{H}_2\text{SO}_4}$  and modestly less condensational narrowing is certainly not ruled out by the size distribution data.

960 If the growth of the particles in this run includes water condensation, the overall sulfuric acid calibration factor is  $\mathcal{F}_{\text{H}_2\text{SO}_4}^{\text{cal}} = 1.2$ . This is well within the stated factor of 2 error in the independent  $\text{NO}_3^-$  CIMS calibration (Kürten et al., 2012), and overall this comprehensive analysis would significantly improve the accuracy and confidence in that calibration, provided that the growth demonstrably includes water uptake. In terms of precision of model-measurement agreement in this analysis, that calibration factor is constrained to within approximately 0.1. However, we cannot (yet) claim such an improvement in the  
965 overall accuracy for two reasons. First, if the particles were in fact dry, then the calibration factor would be  $\mathcal{F}_{\text{H}_2\text{SO}_4}^{\text{cal}} = 2$ , at the outer limit of the independent instrument calibration. Second, if the particles were wet, the true size distribution in the chamber is somewhat uncertain, though still the  $\text{H}_2\text{SO}_4$  condensation sink remains tightly constrained.

970 Uniformity in the chamber is another uncertainty. We estimate the mixing timescale of CLOUD to be of order 60-100 s, but there are known inhomogeneities. Different light sources illuminate the chamber to different extents, and there are always some boundary layer effects near the walls. Consequently, the measured  $\text{H}_2\text{SO}_4$  is not necessarily the chamber average  $\text{H}_2\text{SO}_4$ , but it is that chamber average  $\text{H}_2\text{SO}_4$  that almost certainly governs the particle growth, especially for the larger particles that dominate the condensation sink, which have lifetimes approaching the dilution lifetime. This is important for nucleation, which is non-linear. If we represent the difference between the measured and average concentration as

$$\begin{aligned} \overline{c_{\text{H}_2\text{SO}_4}^3} &= \overline{(\overline{c}_{\text{H}_2\text{SO}_4} + c'_{\text{H}_2\text{SO}_4})^3} \\ 975 &= \overline{c_{\text{H}_2\text{SO}_4}}^3 + 3\overline{c_{\text{H}_2\text{SO}_4}}(\overline{c'_{\text{H}_2\text{SO}_4}})^2 \\ &= \overline{c_{\text{H}_2\text{SO}_4}}^3(1 + 3(\overline{f'_{\text{H}_2\text{SO}_4}})^2) \end{aligned}$$



where  $f'_{\text{H}_2\text{SO}_4}$  is the fractional covariance of  $\text{H}_2\text{SO}_4$ . If that is 0.2, then the average cube is 12 % higher than the cube of the averages. As an example, the UVX excimer laser source is less homogeneous than the UVH Xe–Hg source, and so we expect the OH field and thus  $P_{\text{H}_2\text{SO}_4}$  to also be less homogeneous. Thus, despite being relatively well mixed, the model-measurement agreement for the UVH stages in Fig. 9 is different from (and slightly better than) the model-measurement agreement for the UVX stages in Fig. 10. The difference is manifest in the empirical nucleation coefficients, which are non-linear in  $\text{H}_2\text{SO}_4$ , but not in the growth rates, which are linear in  $\text{H}_2\text{SO}_4$  and thus not subject to covariance. However, because the agreement is well within a factor of 1.5 for all stages for both light sources, our overall conclusion is that the CLOUD chamber is reasonably well mixed and our CSTR calculations are robust.

The light intensity calibrations depend on accurate measurement of  $\text{SO}_2$ , as the direct constraint is on  $P_{\text{H}_2\text{SO}_4}$ ; more importantly, the OH lifetime is governed by CO, which was not measured during CLOUD11. Here we have assumed  $\text{CO} = 100 \text{ ppbv}$ , a value that we measured for the CLOUD synthetic air in a later campaign and which appears to be reproducible with time. The model is nearly linear in CO, with only a slight nonlinearity caused by  $\text{HO}_x$  self reactions that is well within the constraint uncertainty of the intensity steps and corresponding fractional  $\text{H}_2\text{SO}_4$  level changes. The *precision* (i.e. relative constraint) on the chamber-average light amplitudes is high. In addition to direct measurement of CO, other constraints on or measurements of  $\text{HO}_x$  would tighten the overall constraints on absolute light intensity; routine  $\text{HO}_x$  measurements in the CLOUD chamber began after CLOUD11.

Overall, the constraints on nucleation and growth of  $\text{H}_2\text{SO}_4$  are robust, with only the binary uncertainty of the phase state of the growing particles remaining. The methodology presented here, however, builds a web of mutual constraints on the various measurements that are far stronger than the individual, independent calibrations. The precision is very high; light amplitudes span an order of magnitude and nucleation rates span well over 2, and the model is able to reproduce essentially all of the observations to within the measurement precision. A formal optimal error estimation will require a rigorous Bayesian treatment with a microphysical model that fully couples both the gas-phase chemistry and the evolving particle charge distribution. That is beyond the scope of this work.

## 1000 12 Conclusion

The mutual interaction of multiple instruments and processes provide strong constraints on overall calibrations for nucleation experiments such as the example run shown here. A key element is to ensure sufficient nucleation and growth for  $\text{H}_2\text{SO}_4$  loss via condensation to compete with wall loss; this establishes a tight constraint on the  $\text{H}_2\text{SO}_4$  lifetime as well as the condensation sink (total particle surface area). Ultimately the very accurate measurement of total particle numbers via a condensation particle counter (CPC<sub>2.5</sub>) becomes the transferable standard for all other measurements. To firmly constrain accurate  $\text{H}_2\text{SO}_4$ , the exact composition of the growing particle must be known; sufficient base ( $\text{NH}_3$ ) to ensure irreversible condensation of  $\text{H}_2\text{SO}_4$  is important, but the amount of water in the growing particles must also be known for full accuracy. Ideally, experiments below the efflorescence relative humidity of ammonium sulfate (and below the deliquescence relative humidity of ammonium bisulfate)



would ensure dry growth, and companion experiments in the hysteresis region and possibly also above the deliquescence  
1010 relative humidity would constrain the intriguing potential for nucleation and growth to remain wet over this RH range.

In the future, the methodology presented here can and should be extended to a more formal Bayesian approach once some technical steps have been cleared (Ozon et al., 2021a). First is to fully integrate particle charging into the microphysical model. Second is to develop an appropriate quantitative objective function to compare the modeled size distributions with the “bunches of bananas” where individual nucleation and growth modes are not fully resolved. This may well involve methods from image  
1015 processing. Once complete, the method will provide an important anchor point for these nucleation and growth experiments.

## Support

This work was supported by the following grants: AGS1447056; AGS1439551; AGS1801574; AGS1801897; AGS2132089; AGS2215489; and AGS2431817 to CMU from the US NSF. 80NSSC19K0949 to CMU from NASA. AGS1649147; AGS1801280; AGS2215522; AGS2027252 to CU Bounder from the US NSF. NNX16AP36H; and 80NSSC17K0369 to CU Boulder from  
1020 NASA. ACCC Flagship funded by the Academy of Finland grants: 337549; and 357902. Academy professorship funded by the Academy of Finland (grant no. 302958). Academy of Finland projects: 325656; 311932; 334792; 316114; 325647; 325681; 333397; 328616; 357902; 345510; 347782; “Quantifying carbon sink, CarbonSink+ and their interaction with air quality” INAR project funded by Jane and Aatos Erkko Foundation, “Gigacity” project funded by: Wihuri foundation; European Research Council (ERC) project ATM-GTP Contract No. 742206; and European Union via Non-CO2 Forcers and their Climate,  
1025 Weather, Air Quality and Health Impacts (FOCI); and EMME-CARE (856612).



## References

- Ahlm, L., Yli-Juuti, T., Schobesberger, S., Praplan, A. P., Kim, J., Tikkanen, O.-P., Lawler, M. J., Smith, J. N., Tröstl, J., Navarro, J. C. A., Baltensperger, U., Bianchi, F., Donahue, N. M., Duplissy, J., Franchin, A., Jokinen, T., Keskinen, H., Kirkby, J., Kürten, A., Laaksonen, A., Lehtipalo, K., Petäjä, T., Riccobono, F., Rissanen, M. P., Rondo, L., Schallhart, S., Simon, M., Winkler, P. M., Worsnop, D. R., Virtanen, A., and Riipinen, I.: Modeling the thermodynamics and kinetics of sulfuric acid-dimethylamine-water nanoparticle growth in the CLOUD chamber, *Aerosol Science and Technology*, 50, 1017–1032, <https://doi.org/10.1080/02786826.2016.1223268>, 2016.
- Bezantakos, S., Huang, L., Barmpounis, K., Martin, S., and Biskos, G.: Relative humidity non-uniformities in Hygroscopic Tandem Differential Mobility Analyzer measurements, *Journal of Aerosol Science*, 101, 1–9, <https://doi.org/10.1016/j.jaerosci.2016.07.004>, 2016.
- Chan, T. W. and Mozurkewich, M.: Measurement of the coagulation rate constant for sulfuric acid particles as a function of particle size using tandem differential mobility analysis, *Journal of Aerosol Science*, 32, 321–339, [https://doi.org/https://doi.org/10.1016/S0021-8502\(00\)00081-1](https://doi.org/10.1016/S0021-8502(00)00081-1), 2001.
- Dada, L., Lehtipalo, K., Kontkanen, J., Nieminen, T., Baalbaki, R., Ahonen, L., Duplissy, J., Yan, C., Chu, B., Petäjä, T., Lehtinen, K., Kerminen, V.-M., Kulmala, M., and Kangasluoma, J.: Formation and growth of sub-3-nm aerosol particles in experimental chambers, *Nature Protocols*, 15, 1013–1040, <https://doi.org/10.1038/s41596-019-0274-z>, 2020.
- Donahue, N. M., Chuang, W. K., and Schervish, M.: Advances in Chemistry of the Contemporary Atmosphere, vol. 2, chap. Gas-Phase Organic Oxidation Chemistry and Atmospheric Particles, pp. 199–317, World Scientific, [https://doi.org/10.1142/9789813271838\\_0004](https://doi.org/10.1142/9789813271838_0004), 2019.
- Dunne, E. M., Gordon, H., Kürten, A., Almeida, J., Duplissy, J., Williamson, C., Ortega, I. K., Pringle, K. J., Adamov, A., Baltensperger, U., Barmet, P., Benduhn, F., Bianchi, F., Breitenlechner, M., Clarke, A., Curtius, J., Dommen, J., Donahue, N. M., Ehrhart, S., Flagan, R. C., Franchin, A., Guida, R., Hakala, J., Hansel, A., Heinritzi, M., Jokinen, T., Kangasluoma, J., Kirkby, J., Kulmala, M., Kupc, A., Lawler, M. J., Lehtipalo, K., Makhmutov, V., Mann, G., Mathot, S., Merikanto, J., Miettinen, P., Nenes, A., Onnela, A., Rap, A., Reddington, C. L. S., Riccobono, F., Richards, N. A. D., Rissanen, M. P., Rondo, L., Sarnela, N., Schobesberger, S., Sengupta, K., Simon, M., Sipilä, M., Smith, J. N., Stozkhov, Y., Tomé, A., Tröstl, J., Wagner, P. E., Wimmer, D., Winkler, P. M., Worsnop, D. R., and Carslaw, K. S.: Global atmospheric particle formation from CERN CLOUD measurements, *Science*, 354, 1119–1124, <https://doi.org/10.1126/science.aaf2649>, 2016.
- Duplissy, J., Merikanto, J., Franchin, A., Tsagkogeorgas, G., Kangasluoma, J., Wimmer, D., Vuollekoski, H., Schobesberger, S., Lehtipalo, K., Flagan, R. C., Brus, D., Donahue, N. M., Vehkämäki, H., Almeida, J., Amorim, A., Barmet, P., Bianchi, F., Breitenlechner, M., Dunne, E. M., Guida, R., Henschel, H., Junninen, H., Kirkby, J., Kürten, A., Kupc, A., Määttänen, A., Makhmutov, V., Mathot, S., Nieminen, T., Onnela, A., Praplan, A. P., Riccobono, F., Rondo, L., Steiner, G., Tome, A., Walther, H., Baltensperger, U., Carslaw, K. S., Dommen, J., Hansel, A., Petäjä, T., Sipilä, M., Stratmann, F., Vrtala, A., Wagner, P. E., Worsnop, D. R., Curtius, J., and Kulmala, M.: Effect of ions on sulfuric acid-water binary particle formation II: Experimental data and comparison with QC-normalized classical nucleation theory, *Journal of Geophysical Research Atmospheres*, 212, 1752–1775, <https://doi.org/10.1002/2015JD023539>, 2016.
- Ehn, M., Thornton, J. A., Kleist, E., Sipila, M., Junninen, H., Pullinen, I., Springer, M., Rubach, F., Tillmann, R., Lee, B., Lopez-Hilfiker, F., Andres, S., Acir, I.-H., Rissanen, M., Jokinen, T., Schobesberger, S., Kangasluoma, J., Kontkanen, J., Nieminen, T., Kurten, T., Nielsen, L. B., Jorgensen, S., Kjaergaard, H. G., Canagaratna, M., Maso, M. D., Berndt, T., Petaja, T., Wahner, A., Kerminen, V.-M., Kulmala, M., Worsnop, D. R., Wildt, J., and Mentel, T. F.: A large source of low-volatility secondary organic aerosol, *Nature*, 506, 476–479, 2014.



- Finkenzeller, H., Iyer, S., He, X.-C., Simon, M., Koenig, T. K., Lee, C., Valiev, R., Hofbauer, V., Amorim, A., Baalbaki, R., Baccarini, A., Beck, L., Caudillo, L., Chen, D., Dada, L., Duplissy, J., Heinritzi, M., Kemppainen, D., Kim1, C., Krechmer, J., Kürten, A., Kvashnin, A., Lamkaddam, H., Lee, C. P., Lehtipalo, K., Li, Z., Makhmutov, V., Manninen, H. E., Marie, G., Marten, R., Mauldin, R. L., Mentler, B., Müller, T., Petäjä, T., Philippov, M., Ranjithkumar, A., Rörup, B., Shen, J., Stolzenburg, D., Tauber, C., Tham, Y. J., Tomé, A., Vazquez-Pufleau, M., Wagner, A. C., Wang, D. S., Wang, M., Weber, S. K., Nei, W., Wu, Y., Xiao, M., Ye, Q., Zauner-Wieczorek, M., Hansel, A., Baltensperger, U., Brioude, J., Curtius, J., Donahue, N. M., Hadad, I. E., Flagan, R. C., Kulmala, M., Kirkby, J., Sipilä, M., Worsnop, D. R., Rissanen, M., Kurten, T., and Volkamer, R.: The gas-phase source mechanism of iodic acid as a driver of aerosol formation, *Nature Chemistry*, 14, 129–135, <https://doi.org/10.1038/s41557-022-01067-z>, 2022.
- 1065
- 1070 Friese, E. and Ebel, A.: Temperature Dependent Thermodynamic Model of the System  $\text{H}^+ \text{-NH}_4^+ \text{-Na}^+ \text{-SO}_4^{2-} \text{-NO}_3^- \text{-Cl}^- \text{-H}_2\text{O}$ , *The Journal of Physical Chemistry A*, 114, 11 595–11 631, <https://doi.org/10.1021/jp101041j>, 2010.
- Gordon, H., Kirkby, J., Baltensperger, U., Bianchi, F., Breitenlechner, M., Curtius, J., Dias, A., Dommen, J., Donahue, N. M., Dunne, E. M., Duplissy, J., Ehrhart, S., Flagan, R. C., Frege, C., Fuchs, C., Hansel, A., Hoyle, C. R., Kulmala, M., Kürten, A., Lehtipalo, K., Makhmutov, V., Molteni, U., Rissanen, M. P., Stozkhov, Y., Tröstl, J., Tsagkogeorgas, G., Wagner, R., Williamson, C., Wimmer, D., Winkler, P. M., Yan, C., and Carslaw, K. S.: Causes and importance of new particle formation in the present-day and pre-industrial atmospheres, *Journal of Geophysical Research Atmospheres*, 122, 8739–8760, <https://doi.org/10.1002/2017JD026844>, 2017.
- 1075
- Hyvärinen, A.-P., Raatikainen, T., Laaksonen, A., Viisanen, Y., and Lihavainen, H.: Surface tensions and densities of  $\text{H}_2\text{SO}_4 + \text{NH}_3 + \text{water}$  solutions, *Geophysical Research Letters*, 32, <https://doi.org/10.1029/2005GL023268>, 2005.
- Kirkby, J., Curtius, J., Almeida, J., Dunne, E., Duplissy, J., Ehrhart, S., Franchin, A., Gagne, S., Ickes, L., Kurten, A., Kupc, A., Metzger, A., Riccobono, F., Rondo, L., Schobesberger, S., Tsagkogeorgas, G., Wimmer, D., Amorim, A., Bianchi, F., Breitenlechner, M., David, A., Dommen, J., Downard, A., Ehn, M., Flagan, R. C., Haider, S., Hansel, A., Hauser, D., Jud, W., Junninen, H., Kreissl, F., Kvashin, A., Laaksonen, A., Lehtipalo, K., Lima, J., Lovejoy, E. R., Makhmutov, V., Mathot, S., Mikkila, J., Minginette, P., Mogo, S., Nieminen, T., Onnela, A., Pereira, P., Petaja, T., Schnitzhofer, R., Seinfeld, J. H., Sipila, M., Stozkhov, Y., Stratmann, F., Tome, A., Vanhanen, J., Viisanen, Y., Vrtala, A., Wagner, P. E., Walther, H., Weingartner, E., Wex, H., Winkler, P. M., Carslaw, K. S., Worsnop, D. R., Baltensperger, U., and Kulmala, M.: Role of sulphuric acid, ammonia and galactic cosmic rays in atmospheric aerosol nucleation, *Nature*, 476, 429–433, <https://doi.org/10.1038/nature10343>, 2011.
- 1080
- Kupc, A., Amorim, A., Curtius, J., Danielczok, A., Duplissy, J., Ehrhart, S., Walther, H., Ickes, L., Kirkby, J., Kürten, A., Lima, J., Mathot, S., Minginette, P., Onnela, A., Rondo, L., and Wagner, P.: A fibre-optic UV system for  $\text{H}_2\text{SO}_4$  production in aerosol chambers causing minimal thermal effects, *Journal of Aerosol Science*, 42, 532 – 543, <https://doi.org/http://dx.doi.org/10.1016/j.jaerosci.2011.05.001>, 2011.
- 1090 Kürten, A., Rondo, L., Ehrhart, S., and Curtius, J.: Calibration of a Chemical Ionization Mass Spectrometer for the Measurement of Gaseous Sulfuric Acid, *The Journal of Physical Chemistry A*, 116, 6375–6386, <https://doi.org/10.1021/jp212123n>, 2012.
- Kürten, A., Jokinen, T., Simon, M., Sipilä, M., Sarnela, N., Junninen, H., Adamov, A., Almeida, J., Amorim, A., Bianchi, F., Breitenlechner, M., Dommen, J., Donahue, N. M., Duplissy, J., Ehrhart, S., Flagan, R. C., Franchin, A., Hakala, J., Hansel, A., Heinritzi, M., Hutterli, M., Laaksonen, A., Lehtipalo, K., Leiminger, M., Makhmutov, V., Mathot, S., Onnela, A., Petäjä, T., Praplan, A. P., Rondo, L., Schobesberger, S., Seinfeld, J. H., Stratmann, F., Tomé, A., Tröstl, J., Wagner, P. E., Weingartner, E., Williamson, C., Wimmer, D., Ye, P., Baltensperger, U., Carslaw, K. S., Kulmala, M., Worsnop, D. R., Kirkby, J., and Curtius, J.: Neutral molecular cluster formation of sulfuric acid-dimethylamine observed in real time under atmospheric conditions, *Proceedings of the National Academy of Sciences*, 111, 15 019–15 024, <https://doi.org/10.1073/pnas.1404853111>, 2014.
- 1095



- Kürten, A., Williamson, C., Almeida, J., Kirkby, J., and Curtius, J.: On the Derivation of Particle Nucleation Rates from Experimental  
1100 Formation Rates, *Atmospheric Chemistry and Physics*, 15, 4063–4075, <https://doi.org/10.5194/acp-15-4063-2015>, 2015.
- Larriba, C., Hogan Jr., C. J., Attoui, M., Borrajo, R., Garcia, J. F., and de la Mora, J. F.: The Mobility–Volume Relationship below 3.0 nm Examined by Tandem Mobility–Mass Measurement, *Aerosol Science and Technology*, 45, 453–467,  
https://doi.org/10.1080/02786826.2010.546820, 2011.
- Lehtipalo, K., Rondo, L., Schobesberger, S., Jokinen, T., Sarnela, N., Franchin, A., Nieminen, T., Sipilä, M., Kürten, A., Riccobono, F.,  
1105 Erhart, S., Yli-Juuti, T., Konkanen, J., Adamov, A., Almeida, J., Amorim, A., Bianchi, F., Breitenlechner, M., Dommen, J., Downard, A. J., Dunne, E. M., Duplissy, J., Flagan, R. C., Guida, R., Hakala, J., Hansel, A., Jud, W., Kangasluoma, J., Keskinen, H., Kim, J., Kupc, A., Laaksonen, A., Mathot, S., Ortega, I. K., Onnela, A., Praplan, A., Rissanen, M. P., Ruuskanen, T., Santos, F. D., Schallhart, S., Schnitzhofer, R., Smith, J. N., Tröstl, J., Tsagkogeorgas, G., Tomé, A., Vaattovaara, P., Vrtala, A. E., E. Wagner, P., Williamson, C., Wimmer, D., Winkler, P. M., Virtanen, A., Donahue, N. M., Carslaw, K. S., Baltensperger, U., Kirkby, J., Riipinen, I., Curtius, J., Kulmala, M., and Worsnop, D. R.: The effect of acid–base clustering and ions on the growth of atmospheric nano-particles, *Nature Communications*, 7, 11 594, <https://doi.org/10.1038/ncomms11594>, 2016.
- Lei, T., Ma, N., Hong, J., Tuch, T., Wang, X., Wang, Z., Pöhlker, M., Ge, M., Wang, W., Mikhailov, E., Hoffmann, T., Pöschl, U., Su, H., Wiedensohler, A., and Cheng, Y.: Nano-hygrosopicity tandem differential mobility analyzer (nano-HTDMA) for investigating hygroscopic properties of sub-10 nm aerosol nanoparticles, *Atmospheric Measurement Techniques*, 13, 5551–5567, <https://doi.org/10.5194/amt-13-5551-2020>, 2020.
- Mahfouz, N. and Donahue, N. M.: The role of particle charging and the primary ion balance in governing particle losses from teflon chambers, *Aerosol Science and Technology*, 54, 1058–1069, <https://doi.org/10.1080/02786826.2020.1757032>, 2020.
- Mahfouz, N. G. A. and Donahue, N. M.: Atmospheric Nanoparticle Survivability Reduction Due to Charge-Induced Coagulation Scavenging Enhancement, *Geophysical Research Letters*, 48, e2021GL092758, <https://doi.org/10.1029/2021GL092758>, 2021.
- 1120 McMurry, P. H. and Grosjean, D.: Gas and aerosol wall losses in Teflon film smog chambers, *Environmental Science & Technology*, 19, 1176–1181, 1985.
- Mifflin, A. L., Smith, M. L., and Martin, S. T.: Morphology hypothesized to influence aerosol particle deliquescence, *Phys. Chem. Chem. Phys.*, 11, 10 095–10 107, <https://doi.org/10.1039/B910432A>, 2009.
- Mirme, S. and Mirme, A.: The mathematical principles and design of the NAIS – a spectrometer for the measurement of cluster ion and  
1125 nanometer aerosol size distributions, *Atmospheric Measurement Techniques*, 6, 1061–1071, <https://doi.org/10.5194/amt-6-1061-2013>, 2013.
- Ozon, M., Seppänen, A., Kaipio, J. P., and Lehtinen, K. E. J.: Retrieval of process rate parameters in the general dynamic equation for aerosols using Bayesian state estimation: BAYROSOL1.0, *Geoscientific Model Development*, 14, 3715–3739, <https://doi.org/10.5194/gmd-14-3715-2021>, 2021a.
- 1130 Ozon, M., Stolzenburg, D., Dada, L., Seppänen, A., and Lehtinen, K. E. J.: Aerosol formation and growth rates from chamber experiments using Kalman smoothing, *Atmospheric Chemistry and Physics*, 21, 12 595–12 611, <https://doi.org/10.5194/acp-21-12595-2021>, 2021b.
- Rondo, L., Ehrhart, S., Kürten, A., Adamov, A., Bianchi, F., Breitenlechner, M., Duplissy, J., Franchin, A., Dommen, J., Donahue, N. M.,  
1135 Dunne, E. M., Flagan, R. C., Hakala, J., Hansel, A., Keskinen, H., Kim, J., Jokinen, T., Lehtipalo, K., Leiminger, M., Praplan, A., Riccobono, F., Rissanen, M. P., Sarnela, N., Schobesberger, S., Simon, M., Sipilä, M., Smith, J. N., Tomé, A., Tröstl, J., Tsagkogeorgas, G., Vaattovaara, P., Winkler, P. M., Williamson, C., Wimmer, D., Baltensperger, U., Kirkby, J., Kulmala, M., Petäjä, T., Worsnop, D. R.,



- and Curtius, J.: Effect of dimethylamine on the gas phase sulfuric acid concentration measured by Chemical Ionization Mass Spectrometry (CIMS), *Journal of Geophysical Research Atmospheres*, 121, 3036–3049, <https://doi.org/10.1002/2015JD023868>, 2016.
- Schnitzhofer, R., Metzger, A., Breitenlechner, M., Jud, W., Heinritzi, M., Menezes, L.-P. D., Duplissy, J., Guida, R., Haider, S., Kirkby, J., Mathot, S., Minginette, P., Onnela, A., Walther, H., Wasem, A., Hansel, A., and CLOUD, T.: Characterisation of Organic Contaminants 1140 in the CLOUD Chamber at CERN, *Aerosol Measurement Techniques*, 7, 2159–2168, <https://doi.org/10.5194/amt-7-2159-2014>, 2014.
- Stolzenburg, D., Steiner, G., and Winkler, P. M.: A DMA-train for precision measurement of sub-10 nm aerosol dynamics, *Atmospheric 1145 Measurement Techniques*, 10, 1639–1651, <https://doi.org/10.5194/amt-10-1639-2017>, 2017.
- Stolzenburg, D., Simon, M., Ranjithkumar, A., Kürten, A., Lehtipalo, K., Gordon, H., Nieminen, T., Pichelstorfer, L., He, X., Brilke, S., Xiao, 1150 M., Amorim, A., Baalbaki, R., Baccarini, A., Beck, L., Bräkling, S., Murillo, L. C., Chen, D., Chu, B., Dada, L., Dias, A., Dommen, J., Duplissy, J., Haddad, I. E., Finkenzeller, H., Fischer, L., Carracedo, L. G., Heinritzi, M., Kim, C., Koenig, T. K., Kong, W., Lamkaddam, H., Lee, C. P., Leiminger, M., Li, Z., Makhmutov, V., Manninen, H. E., Marie, G., Marten, R., Müller, T., Nie, W., Partol, E., Petäjä, T., Pfeifer, J., Philipov, M., Rissanen, M. P., Rörup, B., Schobesberger, S., Schuchmann, S., Shen, J., Sipilä, M., Steiner, G., Stozhkov, Y., Tauber, C., Tham, Y. J., Tomé, A., Vazquez-Pufleau, M., Wagner, A. C., Wang, M., Wang, Y., Weber, S. K., Wimmer, D., Wlasits, P. J., Wu, Y., Ye, Q., Zauner-Wieczorek, M., Baltensperger, U., Carslaw, K. S., Curtius, J., Donahue, N. M., Flagan, R. C., Hansel, A., Kulmala, M., Volkamer, R., Kirkby, J., and Winkler, P. M.: Enhanced growth rate of atmospheric particles from sulfuric acid, *Atmospheric Chemistry 1155 and Physics*, 20, 7359–7372, <https://doi.org/10.5194/acp-20-7359-2020>, 2020.
- Vehkamaki, H. and Riipinen, I.: Thermodynamics and kinetics of atmospheric aerosol particle formation and growth, *Chem. Soc. Rev.*, 41, 5160–5173, <https://doi.org/10.1039/C2CS00002D>, 2012.
- Vlasenko, S. S., Su, H., Pöschl, U., Andreae, M. O., and Mikhailov, E. F.: Tandem configuration of differential mobility and centrifugal 1160 particle mass analysers for investigating aerosol hygroscopic properties, *Atmospheric Measurement Techniques*, 10, 1269–1280, <https://doi.org/10.5194/amt-10-1269-2017>, 2017.
- Yli-Juuti, T., Barsanti, K., Hildebrandt Ruiz, L., Kieloaho, A.-J., Makkonen, U., Petäjä, T., Ruuskanen, T., Kulmala, M., and Riipinen, I.: Model for acid-base chemistry in nanoparticle growth (MABNAG), *Atmospheric Chemistry and Physics*, 13, 12 507–12 524, 1165 <https://doi.org/10.5194/acp-13-12507-2013>, 2013.

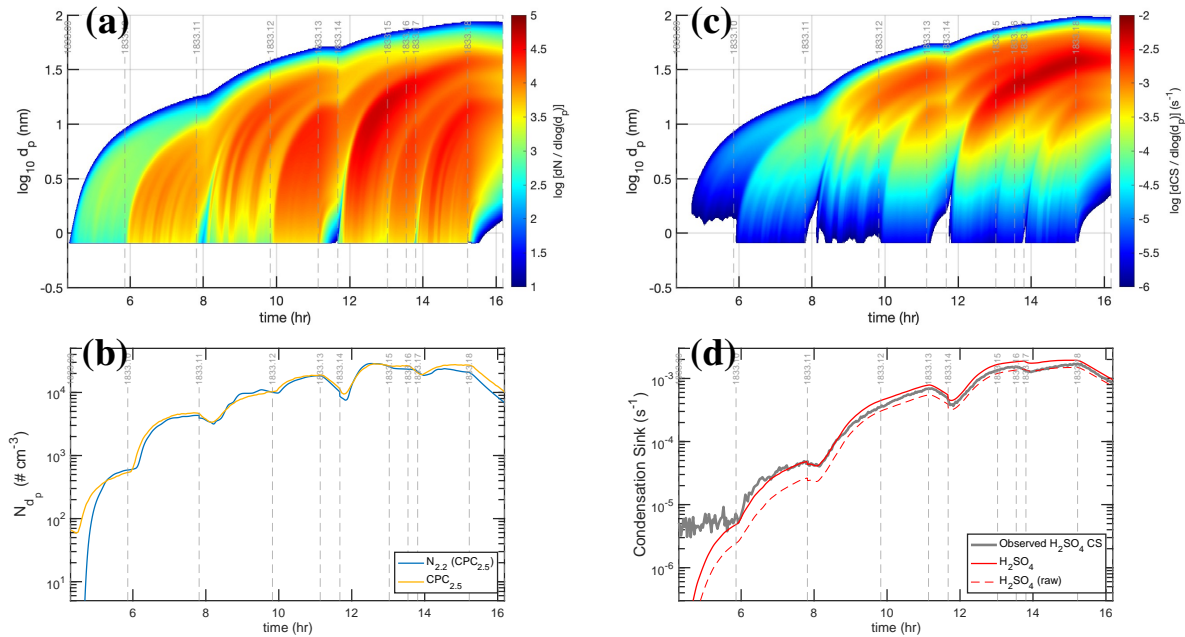


**Figure 20.** Optimal modeled particle size and corresponding condensation sink distributions with wet  $(\text{NH}_4)_2 \cdot \text{SO}_4 \cdot (\text{H}_2\text{O})_n$  growth, and their agreement with measurements during the UVX stages. (a) Simulated particle size distribution ( $dN/d \log d_p$ ) for optimal parameters, with empirical nucleation coefficients and an  $\text{H}_2\text{SO}_4$  calibration factor of 1.2. (b) Simulated (blue) and observed (gold) total particle number measurable by a CPC<sub>2.5</sub>. (c) Simulated condensation-sink distribution ( $d\text{CS}/d \log d_p$ ). (d) Simulated (red) and observed (gray) condensation sink. Simulated values are shown both with (solid) and without (dashed) a Van der Waals correction; the observed values include the correction; the condensation sink is reproduced with good fidelity aside from the enhanced loss during the cleaning stage, which was not simulated. Other than the low-intensity stages (01 and 02), charged and neutral nucleation are competitive because charged nucleation is limited by ion-pair production. That saturation value serves as an additional constraint on the nucleation parameters.



1160 **Appendix A: Photochemical model**

**A1 gas-phase reactions**

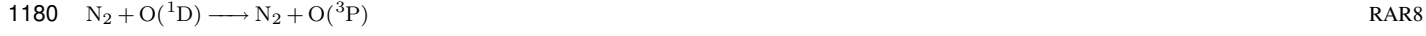
The gas-phase photochemistry for the OH actinometry calibration run can be modeled with the following set of reactions. The initial photochemistry is driven by odd-oxygen ( $O_x$ ) reactions:



$$k_0 = 5.7 \times 10^{-34} \times (T/300)^{-2.8}$$

$$k_\infty = 2.8 \times 10^{-12}$$

$$F_c = \exp(-T/696)$$



$$k = 1.8 \times 10^{-11} e^{+107/T}$$



$$k = 3.2 \times 10^{-11} e^{+67/T}$$

This includes three distinct  $O_3$  photolysis representations so that the model will keep track of the separate contributions of individual lights during stages when more than one light is illuminated. This feeds into odd-hydrogen ( $HO_x$ ) chemistry:



$$k = 1.63 \times 10^{-10} e^{+60/T}$$



$$k = 1.7 \times 10^{-12} e^{-940/T}$$

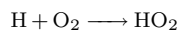


$$k = 4.8 \times 10^{-11} e^{+250/T}$$



RAR13

$$k = 1.0 \times 10^{-14} e^{-490/T}$$



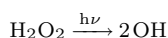
RAR14

1195

$$k_0 = 7.4 \times 10^{-31} \times (T/300)^{-2.4}$$

$$k_\infty = 7.5 \times 10^{-11}$$

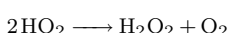
$$F_c = \exp(-T/517)$$



RAR15

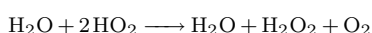
$$k = \text{photolysis}(\text{H}_2\text{O}_2 \text{ OH})$$

1200



RAR16

$$k = (3.0 \times 10^{-13} e^{+460/T} + 2.1 \times 10^{-33} e^{+920/T} \times c_M)$$



RAR17

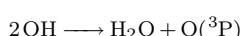
$$k = 2.8 \times 10^{-18} \times (3.0 \times 10^{-13} e^{+460/T} + 2.1 \times 10^{-33} e^{+920/T} \times c_M)$$



RAR18

1205

$$k = 2.8 \times 10^{-12} e^{-1800/T}$$



RAR19

$$k = 1.8 \times 10^{-12}$$



RAR20

$$k = 1.8 \times 10^{-12}$$

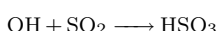
1210 Reaction with CO is a major OH sink, and in the base model is the only “hydrocarbon” reaction treated.



RAR21

$$k = 1.3 \times 10^{-13} \times (1 + 0.6 \times (c_M / 2.5 \times 10^{19}))$$

Finally, OH is also the sink of SO<sub>2</sub> and ultimately source of H<sub>2</sub>SO<sub>4</sub>:



RAR22

1215

$$k_0 = 4.5 \times 10^{-31} \times (T/300)^{-3.9}$$

$$k_\infty = 1.3 \times 10^{-12} \times (T/300)^{-0.7}$$

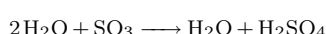
$$F_c = 0.525$$



RAR23

$$k = 1.3 \times 10^{-12} e^{-330/T}$$

1220



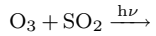
RAR24

$$k = 8.5 \times 10^{-41} e^{+6540/T}$$

Wall loss in general is modeled as a process relevant to all species in the photochemical system, with wall collision frequencies scaled by the (empirically constrained) H<sub>2</sub>SO<sub>4</sub> wall loss (collision frequency) and an uptake coefficient (assumed to be  $\gamma = 1$ ) for H<sub>2</sub>SO<sub>4</sub>. In addition, based on the observed 1:1 stoichiometry of SO<sub>2</sub> and O<sub>3</sub> loss when especially the 385 nm UV



1225 light emitting diodes (LS3) are on at full power, a photon-mediated uptake of  $\text{SO}_2$  and  $\text{O}_3$  (presumably to make wall-adsorbed  $\text{H}_2\text{SO}_4$ ) is included in the mechanism.



RAR25

$k = \text{photolysis}(\text{SO}_2 \text{ O}_3 \text{ wall})$

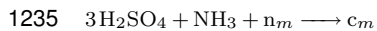
## A2 ion reactions

1230 Nucleation as well as ion production and loss can be treated with a set of pseudo-reactions creating and removing primary ions ( $n^{\pm}$ ) as well as nucleated clusters (2 nm particles in three charge states,  $p_2^{\circ, \pm}$  above and  $c_{n,m,p}$  here). Here the subscripts  $n$ ,  $m$ , and  $p$  indicate charge, as “neutral”, “minus (negative)” and “positive” (i.e.  $\circ$ ,  $-$ , and  $+$  elsewhere):



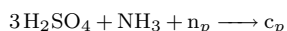
RAR26

$k = \text{nucleationCoefficient}(\text{ternary neutral})$



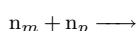
RAR27

$k = \text{nucleationCoefficient}(\text{ternary anion})$

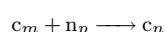


RAR28

$k = \text{nucleationCoefficient}(\text{ternary cation})$

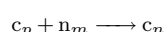


RAR29



RAR30

$k = 1.75 \times 10^{-6}$



RAR31

$k = 1.45 \times 10^{-6}$



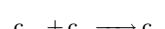
RAR32

$k = 2 \times 10^{-9}$

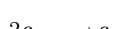


RAR33

$k = 2 \times 10^{-9}$



RAR34



RAR35

$k = 1.2 \times 10^{-9}$

## A3 modal microphysics

The modal representation continues with growth from 2 nm to a nanoparticle nucleation mode at 5 nm,  $n_{p,n,m,p}$ . The growth 1255 is a first-order “reaction” with  $\text{H}_2\text{SO}_4$  but with a rate constant reflecting of order 100 collisions required for 3 nm of growth. Coagulation as well as diffusion charging and neutralization by both primary ions and charged 2 nm particles is also treated.



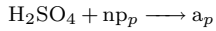
	$\text{H}_2\text{SO}_4 + c_n \longrightarrow \text{np}_n$ $k = \text{growthCoefficient(cluster)}$	RAR36
	$\text{H}_2\text{SO}_4 + c_m \longrightarrow \text{np}_m$	RAR37
1260	$k = \text{growthCoefficient(cluster)}$	
	$\text{H}_2\text{SO}_4 + c_p \longrightarrow \text{np}_p$ $k = \text{growthCoefficient(cluster)}$	RAR38
	$\text{n}_m + \text{np}_p \longrightarrow \text{np}_n$ $k = 1.75 \times 10^{-6}$	RAR39
1265	$\text{n}_p + \text{np}_m \longrightarrow \text{np}_n$ $k = 1.45 \times 10^{-6}$	RAR40
	$\text{c}_m + \text{np}_p \longrightarrow \text{np}_n$ $k = 1.4 \times 4 \times 10^{-7}$	RAR41
	$\text{c}_p + \text{np}_m \longrightarrow \text{np}_n$ $k = 1.4 \times 4 \times 10^{-7}$	RAR42
1270	$\text{n}_m + \text{np}_n \longrightarrow \text{np}_m$ $k = 3 \times 10^{-8}$	RAR43
	$\text{n}_p + \text{np}_n \longrightarrow \text{np}_p$ $k = 3 \times 10^{-8}$	RAR44
1275	$\text{c}_m + \text{np}_n \longrightarrow \text{np}_m$ $k = 1 \times 10^{-8}$	RAR45
	$\text{c}_p + \text{np}_n \longrightarrow \text{np}_p$ $k = 1 \times 10^{-8}$	RAR46
	$\text{np}_m + \text{np}_p \longrightarrow \text{np}_n$ $k = 1 \times 10^{-7}$	RAR47
1280	$2 \text{np}_n \longrightarrow \text{np}_n$ $k = 1.5 \times 10^{-9}$	RAR48
	$\text{c}_n + \text{np}_n \longrightarrow \text{np}_n$ $k = 3 \times 10^{-9}$	RAR49
1285	Finally, growth to an Aitken mode at 15 nm, $\text{a}_{n,m,p}$ , requires 1000s of collisions of $\text{H}_2\text{SO}_4$ with those growing nanoparticles, and the resulting Aitken mode particles can interact with all of the smaller nanoparticles and clusters, in all charge states. We ignore formation of doubly charged particles for all these sizes as negligible.	

$\text{H}_2\text{SO}_4 + \text{np}_n \longrightarrow \text{a}_n$   
 $k = \text{growthCoefficient(nano)}$

1290  $\text{H}_2\text{SO}_4 + \text{np}_m \longrightarrow \text{a}_m$  RAR51

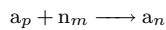


$k = \text{growthCoefficient(nano)}$



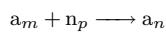
RAR52

$k = \text{growthCoefficient(nano)}$



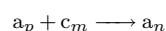
RAR53

$$k = 1.75 \times 10^{-6}$$



RAR54

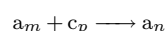
$$k = 1.45 \times 10^{-6}$$



RAR55

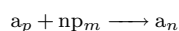
$$k = 1.4 \times 4 \times 10^{-7}$$

1295



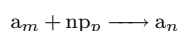
RAR56

$$k = 1.4 \times 4 \times 10^{-7}$$



RAR57

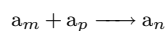
$$k = 1.4 \times 1 \times 10^{-7}$$



RAR58

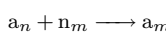
1300

$$k = 1.4 \times 1 \times 10^{-7}$$



RAR59

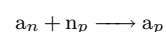
$$k = 2 \times 10^{-8}$$



RAR60

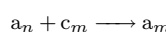
$$k = 1 \times 10^{-7}$$

1305



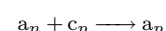
RAR61

$$k = 1 \times 10^{-7}$$



RAR62

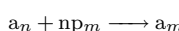
$$k = 3 \times 10^{-8}$$



RAR63

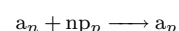
1310

$$k = 3 \times 10^{-8}$$



RAR64

$$k = 7 \times 10^{-9}$$



RAR65

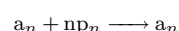
$$k = 7 \times 10^{-9}$$

1315



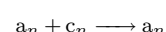
RAR66

$$k = 2 \times 10^{-9}$$



RAR67

$$k = 4 \times 10^{-9}$$



RAR68

1320

$$k = 8 \times 10^{-9}$$